Springer Theses
Recognizing Outstanding Ph.D. Research

Michihiro Nishikawa

Photofunctionalization of Molecular Switch Based on Pyrimidine Ring Rotation in Copper Complexes

Springer

Springer Theses

Recognizing Outstanding Ph.D. Research

For further volumes:
http://www.springer.com/series/8790

Aims and Scope

The series "Springer Theses" brings together a selection of the very best Ph.D. theses from around the world and across the physical sciences. Nominated and endorsed by two recognized specialists, each published volume has been selected for its scientific excellence and the high impact of its contents for the pertinent field of research. For greater accessibility to non-specialists, the published versions include an extended introduction, as well as a foreword by the student's supervisor explaining the special relevance of the work for the field. As a whole, the series will provide a valuable resource both for newcomers to the research fields described, and for other scientists seeking detailed background information on special questions. Finally, it provides an accredited documentation of the valuable contributions made by today's younger generation of scientists.

Theses are accepted into the series by invited nomination only and must fulfill all of the following criteria

- They must be written in good English.
- The topic should fall within the confines of Chemistry, Physics, Earth Sciences, Engineering and related interdisciplinary fields such as Materials, Nanoscience, Chemical Engineering, Complex Systems and Biophysics.
- The work reported in the thesis must represent a significant scientific advance.
- If the thesis includes previously published material, permission to reproduce this must be gained from the respective copyright holder.
- They must have been examined and passed during the 12 months prior to nomination.
- Each thesis should include a foreword by the supervisor outlining the significance of its content.
- The theses should have a clearly defined structure including an introduction accessible to scientists not expert in that particular field.

Michihiro Nishikawa

Photofunctionalization of Molecular Switch Based on Pyrimidine Ring Rotation in Copper Complexes

Doctoral Thesis accepted by
The University of Tokyo, Tokyo, Japan

Springer

Author
Dr. Michihiro Nishikawa
The University of Tokyo
Tokyo
Japan

Supervisor
Prof. Hiroshi Nishihara
The University of Tokyo
Tokyo
Japan

ISSN 2190-5053 ISSN 2190-5061 (electronic)
ISBN 978-4-431-54624-5 ISBN 978-4-431-54625-2 (eBook)
DOI 10.1007/978-4-431-54625-2
Springer Tokyo Heidelberg New York Dordrecht London

Library of Congress Control Number: 2013955562

Printed on acid-free paper

Springer is part of Springer Science+Business Media (www.springer.com)

Parts of this thesis have been published in the following journal articles:

1. Nishikawa M, Nomoto K, Kume S, Inoue K, Sakai M, Fujii M, Nishihara H (2010) J Am Chem Soc 132:9579.
2. Nishikawa M, Nomoto K, Kume S, Nishihara H (2012) J Am Chem Soc 134:10543.
3. Nishikawa M, Nomoto K, Kume S, Nishihara H (2013) Inorg Chem 52:369.

Supervisor's Foreword

Metal complexes bearing π-conjugated chelating ligands are fascinating not only in basic science focusing on their unique physical and chemical properties but also in application to molecular-based devices. For example, photophysical properties of metal complexes are valuable for fabrication of dye-sensitized solar cells and light-emitting devices, and redox-active metal complexes of their two oxidation states reversibly switchable by electronic stimuli are useful in application to nanotechnology such as molecular electronics. Our group has been constructing a single molecular system made of copper complexes bearing a bidentate ligand with a rotatable pyrimidine moiety. This system exhibits an electrochemical potential shift by the motion of the artificial molecular rotor.

Dr. Nishikawa has introduced photofunctions into the copper-pyrimidine molecular rotors in the course of his study for the Ph.D. Two of his remarkable achievements are development of a new class of luminescence, that is, dual emission caused by rotational isomerization, and construction of a new photo-electronic conversion system caused by the redox potential switching based on photoinduced-electron-transfer-driven rotation.

He started his Ph.D. research by investigating the rotational equilibrium in newly synthesized copper(I) complexes bearing two bidentate ligands, pyridylpyrimidine and bulky diphosphine, using NMR spectroscopy and single crystal X-ray structural analysis. He analyzed ion-pairing sensitivities of rotational bistability of the copper complexes from the viewpoint of both thermodynamics and kinetics, leading to discovery of evidence for the intramolecular process of interconversion and the suitability of a common organic solution state for the desired function. Next, he developed a molecular system that exhibits heat-sensitive dual luminescence behavior caused by the pyrimidine ring rotational isomerization in copper(I) complexes. This peculiar photochemical process was examined in detail by transient emission spectral measurement. Dr. Nishikawa's finding is valuable for designing a promising way to handle the photo-processes of transition metal complexes. Additionally, he created a novel process for conversion of light stimuli into electrochemical potential via reversibly working artificial molecular rotation. This was realized by two strategies, a redox mediator system and a partial oxidation system. In both systems, photoinduced electron transfer from the copper complex

to the electron acceptor played a key role for the photo- and heat-driven rotation. In conclusion, his research provides novel electronic and photonic functions of copper-pyrimidine complexes based on repeatable conversion of external stimuli into redox potential signals.

Dr. Nishikawa's Ph.D. thesis comprises descriptions of his three research achievements noted above together with a general introduction and concluding remarks. The thesis demonstrates the excellence of his research concept, molecular design, experimental plan, and discussion of the results. I hope that the publishing of this thesis will stimulate researchers in the field of molecular science.

Tokyo, August 2013 Hiroshi Nishihara

Acknowledgments

This work was accomplished with a great deal of support from many people. I would like to express my gratitude to all of them.

My research was fully supervised by Dr. Hiroshi Nishihara, Professor at The University of Tokyo. Dr. Nishihara provided me with not only a chance to conduct this interesting research but also valuable guidance, discussions, and suggestions. For that, I am extremely grateful to Dr. Nishihara.

I would also like to express my gratitude to Dr. Shoko Kume, Assistant Professor at The University of Tokyo. She kindly gave me a lot of guidance and specific advice for this research.

For their helpful comments and suggestions, I am very grateful to Dr. Yoshinori Yamanoi, Associate Professor at The University of Tokyo; Dr. Ryota Sakamoto, Assistant Professor at The University of Tokyo; Dr. Mariko Miyachi, Assistant Professor at The University of Tokyo; and Dr. Tetsuro Kusamoto, Assistant Professor at The University of Tokyo.

For measurement of time-resolved emission spectra and for their discussions with me, I gratefully acknowledge Dr. Masaaki Fujii, Professor at the Tokyo Institute of Technology; Dr. Makoto Sakai, Associate Professor at the Tokyo Institute of Technology; and Dr. Keiichi Inoue, Assistant Professor at the Tokyo Institute of Technology. As well, I would like to express my gratitude to Ms. Kimoyo Saeki and Ms. Aiko Sakamoto for elemental analysis.

I am deeply grateful to all members of the Nishihara Laboratory for their helpful discussions and the shared enjoyment of our research activity, and I also express my gratitude to Dr. Kuniharu Nomoto for giving me valuable advice at the beginning of my research.

I am indebted to a JSPS Research Fellowship for Young Scientists and to the Global COE Program for Chemistry Innovation for financial support.

Finally, I would like to express my special gratitude to my family not only for providing financial support but also for encouraging and supporting me in spirit.

Contents

Chapter 1
General Introduction

Abstract I described general introduction for importance of metal complexes, well-established unique nature of copper complexes bearing diimines, and the previous research of our group on stimuli-responsive pyrimidine ring rotation in copper complexes. An advantage of our system is that we can extract useful electric responses from a simple multistable molecule. The aim of studies in my Ph.D course on development of new types of emission and photoresponsivity by photofunctionalization of the copper complex system is described.

Keywords: Metal complex · Molecular switch · Copper complex · Redox · Luminescence

1.1 Metal Complexes Bearing π-Conjugated Ligands

Metal complexes bearing π-conjugated ligands, such as chelating polypyridines, play an important role in both application and novel phenomena not only for their varieties of molecular structures and metal-ligand bond strengths but also their electrochemical, photophysical, magnetic, and other unique properties (Fig. 1.1). Ease of tuning for these functions by choosing metal and ligand components is one of the significant advantages for this class of materials. I described herein several examples to show the importance of the metal complexes.

1.1.1 Photophysics of Metal Complexes Bearing π-Conjugated Chelating Ligands

The photoprocesses of metal complexes bearing π-conjugated chelating ligands are of interest for their potential use in dye-sensitized solar cells [1–5], light-emitting devices [6–9], and photocatalysts [10–13] due to a combination of high

M. Nishikawa, *Photofunctionalization of Molecular Switch Based on Pyrimidine Ring Rotation in Copper Complexes*, Springer Theses,
DOI: 10.1007/978-4-431-54625-2_1, © Springer Japan 2014

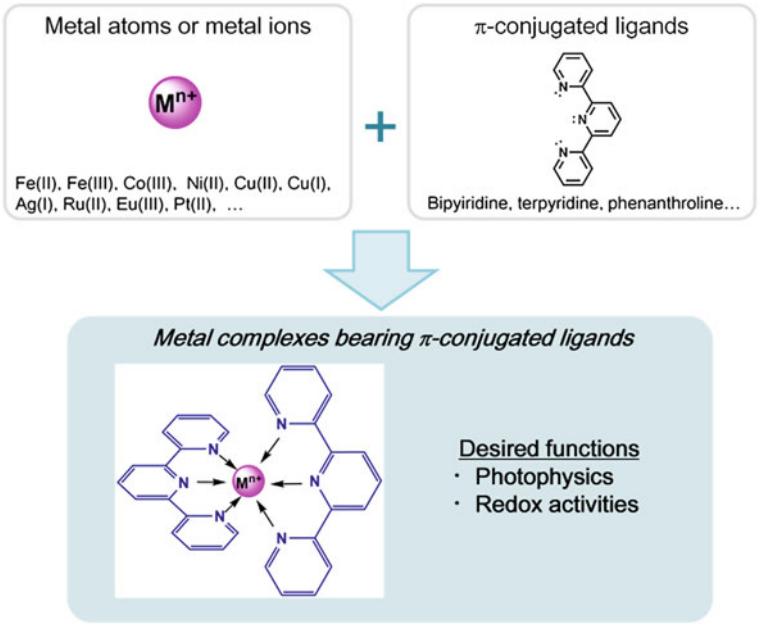

Fig. 1.1 Metal complexes bearing π-conjugated chelating polypyridine ligands

thermal stability, reversible redox activity, intense visible absorption, and the formation of a long-lived charge transfer (CT) excited state. Investigation of luminescence is important not only for luminescence itself but also properties related to photoexcited state.

For example, tris(bipyridine)ruthenium(II) complex ($[Ru(bpy)_3]^{2+}$, bpy = 2,2′-bipyridine) and their derivatives such as **A** have significant advantages for dye-sensitized solar cells (Fig. 1.2). Efficient injection of an electron into the conduction bond of the titanium oxide is achieved, because the lowest electronic excited state of them is of a metal-to-ligand-charge-transfer (MLCT) nature, involving the electronic transitions from a metal *d* orbital to a π^* antibonding orbital centered on the diimine ligand [5]. For another example, hydrogen production using light energy through photocatalytic ability of the complexes has been investigated [11].

The photophysics of metal complexes with other metals and ligands such as platinum(II) and iridium(III) have been well-studied. The emissive excited state of these complexes can be either MLCT or ligand centered (LC) depending on the ligand environment. Whatever the electronic nature, it is invariably triplet states, because of a consequence of the high spin-orbit coupling of the second and third row transition metal atom. Utilization of the triplet state has advantages for light-emitting devices. Unlike fluorescence dyes, an emission of materials doped with platinum(II) porphyrin (**B**) [5] results from both singlet and triplet excited states. It was also reported that nearly a maximum internal efficiency 100 % was achieved

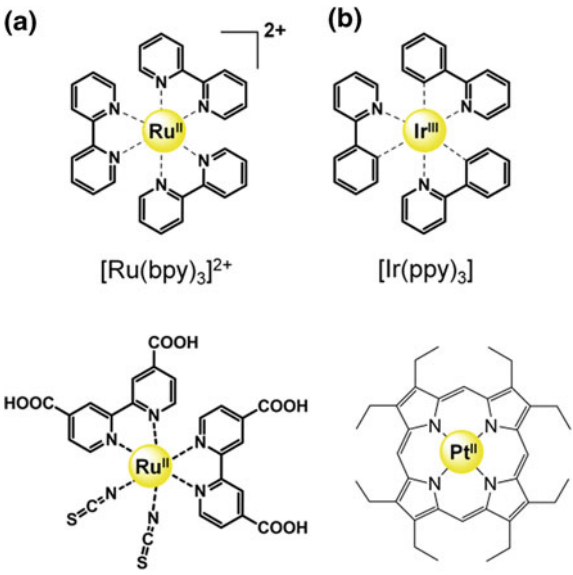

Fig. 1.2 Well-employed metal complexes for promising photofunctions

by employing the host organic materials doped with *fac*-tris(2-phenylpyridine)iridium(III) ($Ir(ppy)_3$ in Fig. 1.2) [6].

A single, dominant and lowest-energy-emissive excited state in ruthenium(II) complexes and most other chromophores is observed in a fluid solutions at room-temperature, due to a breakdown of the standard nonradiative decay pathways. One of the recent topics in photo-functional molecules is to build simple metal complexes, which exhibit dual phosphorescence derived from the two independent excited states [14–16].

Tor et al. have reported that a family of heteroleptic ruthenium(II) coordination complexes containing substituted 1,10-phenanthroline (phen) ligands with extended conjugation [15]. They found that ruthenium(II) complexes containing 4-substituted phen ligands exhibit two simultaneously emissive excited states at room-temperature in a fluid solution. The short-lived, short wavelength component is essentially bipyridine-based, while the long-lived, long wavelength component is localized predominantly on the more conjugated phen ligand. They concluded that an asymmetry in the phen facilitates the production of these two nonequilibrated emissive states.

Dual emission of cyclometalated iridium(III) polypyridine complexes was reported by Tang et al. [14]. The complexes showed dual emission in a fluid solution at room temperature. They assigned the higher energy band to a triplet intraligand ^{3}IL excited state, and the low energy feature to an excited state with high ^{3}MLCT/^{3}LLCT character. The latter should also possess substantial amine to a ligand charge transfer ^{3}NLCT. They showed an environmental-sensitivity of the emission, and concluded that the use of these compounds led to a new luminescent probe.

1.1.2 Molecular Switches Based on Metal Complexes Bearing π-Conjugated Ligands

Multistable molecules (Fig. 1.3) that are capable of intramolecular structural or chemical transitions form a subclass of molecules useful in nanotechnology applications, such as in molecular electronics [17–30], magnetic ordering [31, 32], artificial photosynthesis [10–13, 33, 34], photochromic materials [35–56], and molecular machines [57–73]. These devices are often based on organic molecules and/or metal complexes bearing π-conjugated ligands. Redox-active molecules, in which oxidation states are reversibly switched by electronic stimuli, are one of the key components in these molecular devices (Figs. 1.3 and 1.4); ferrocene (Fc), decamethylferrocene (DMFc), other ferrocene derivatives, and polypyridine metal complexes, such as bis(terpyridine)iron(II) complexes, are a common class of redox-active molecules due to ferrocenium ion/ferrocene (Fc^+/Fc) and corresponding reactions [18, 23–30, 39–41]. Photochromic molecules, such as azobenzene [42–45] and diarylethene [35–38, 55, 56], have attracted considerable attention among available photoresponsive materials because of the reversible light-convertible bistable states with significant color changes occurring in these molecules (Figs. 1.3 and 1.5) [35–56].

Park et al. have reported that the redox-active metal complexes are involved in charge injection of electrode-bridged redox-active single molecules in single-electron transistors, using cobalt(III/II) redox in bis(terpyridine)cobalt complex derivatives [18]. Our group has reported the bottom-up fabrication of bis(terpyridine) metal complex wires on Au/mica electrodes, intra-wire redox conduction by successive electron hopping between neighboring redox sites, and the long-range electron transport abilities of such wires [23–30]. The fabrication of complex wires on semiconducting silicon electrodes shows dopant-dependent and photo-switchable intra-wire redox conduction [23–30].

Several groups have reported that redox-active molecule can be functionalized with photo-switchable ability by attaching photochromic molecules [39–56], such as azobenzene [42–45] and diarylethene [55, 56]; Our group has demonstrated photo-chrome coupled metal complexes with collaborative properties [39–54] such as molecular photomemory with controllable depth [45] and redox-conjugated reversible isomerization with a single green light (Fig. 1.6) [42], including systems in a modified electrode [43] and a polymer particle [44]. Moreover, our group has developed an artificial molecular system which exhibited reversible photoelectronic signal conversion based on photoisomerization-controlled coordination change by azobenzene-appended bipyridine through ligand exchange at the copper center (*i.e.*, the transition was not intramolecular), considering the function of visual sense [46–48]. Our group recently has developed this system with acid and base-controllable function [47].

Redox-active molecular machines are often employed as an imitation of muscle, where redox-signal from brain can be repeatedly converted into macroscopic motions. I note that redox-driven molecular motion based on organic molecules can

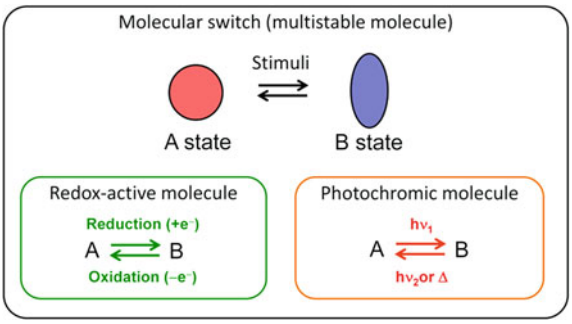

Fig. 1.3 Conceptual diagram showing multistable molecules, redox-active molecules, and photochromic molecules

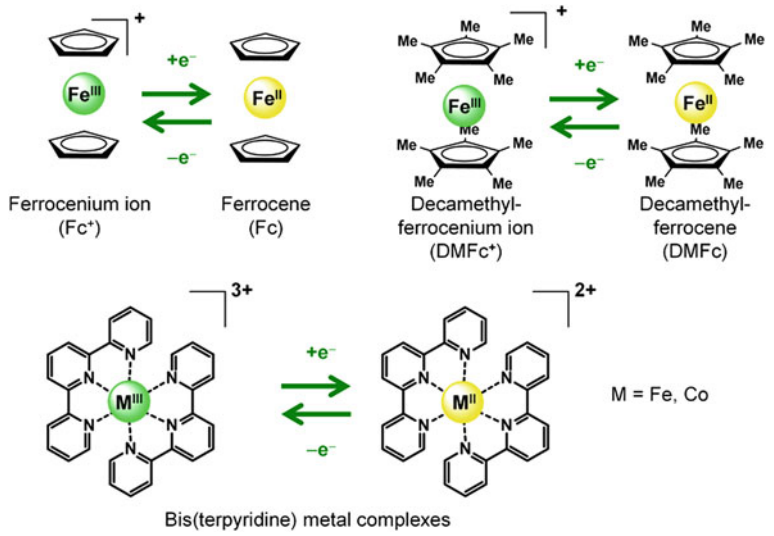

Fig. 1.4 Well-employed redox active molecules based on metal complexes bearing π-conjugated ligands

be applicable in molecular-level memory devices based on electromagnetic responses [22] and conversion into macroscopic mechanics [62]. Redox reactions such as copper(II/I) [68–83] are widely used as input stimuli to drive molecular machines that display linear and rotational motions using supramolecule such as rotaxanes and catenanes, reported by Sauvage et al. [68–73]. Some molecular machines are fueled by light through photoelectron transfer (PET) processes [65–73], although the induced displacement does not persist without introduction of a potential trap or irreversible process, and conformational switching induced by PET is inherently transient.

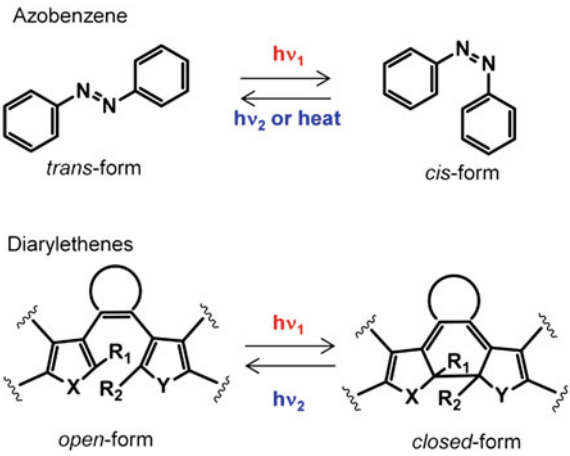

Fig. 1.5 Well-employed photochromic molecules

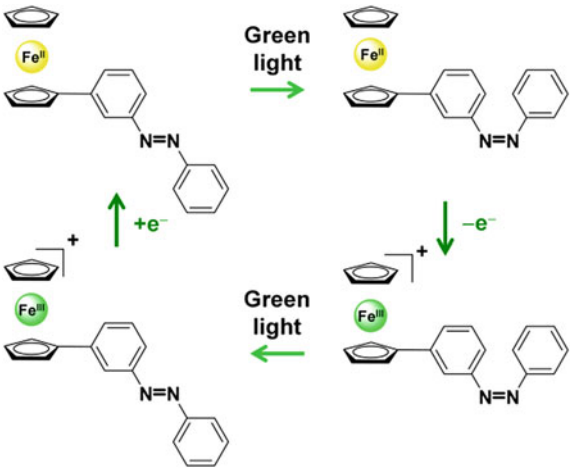

Fig. 1.6 Redox-conjugated reversible isomerization of ferrocenylazobenzene with a single *green* light

1.2 Copper Complexes Bearing Two Bidentate Ligands Including Diimines

Copper complexes bearing two bidentate ligands including diimines have well-established unique relationship between reversible redox activities, photophysics, and coordination structures in these compounds [46–48, 68–133]. The copper(I) state prefers a tetrahedral geometry, whereas the copper(II) state favors a square planar geometry or a 5- or 6-coordinated form due to Jahn–Teller effects [68–83]. The structural changes associated with electron transfer events turn out to play a significant role not only in the function of copper blue proteins [84–87] but also applications in nanoscience such as molecular machines that are based on supramolecular structures [46–48, 68–73]. As a result, crowded coordination geometry generally renders the

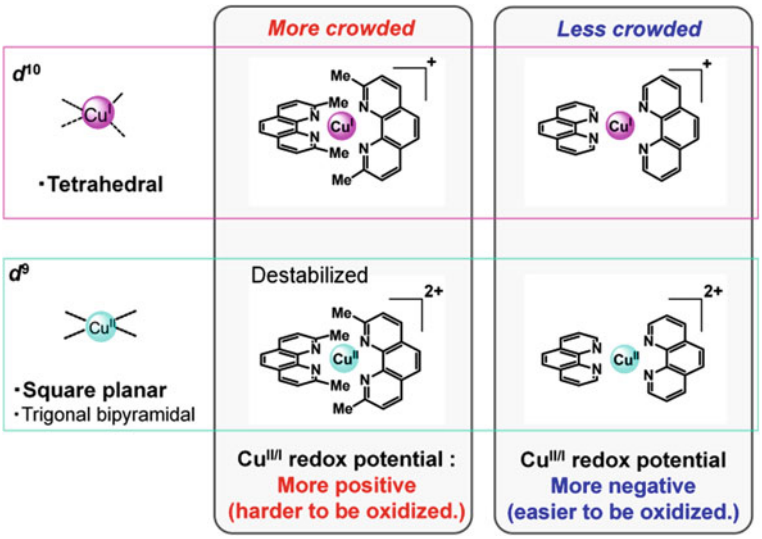

Fig. 1.7 Conceptual diagram showing the well-established unique relationship between reversible redox activities and coordination structures

oxidation of copper(I) to copper(II) thermodynamically less favorable due to destabilization by steric repulsion in the copper(II) state (Fig. 1.7) [74]. For example, the oxidation potential of $[Cu(dmp)_2]^+$ (dmp = 2,9-dimethyl-1,10-phenanthlorine, $E^{\circ\prime} = 0.64$ V vs SCE) in 0.1 M tetrabutylammonium hexafluorophosphate CH_2Cl_2 is much more positive than that of $[Cu(phen)_2]^+$ (phen = 1,10-phenanthlorine, $E^{\circ\prime} = 0.19$ V vs SCE) [74, 75]. Furthermore, bidentate diimines on copper undergo ligand substitution reactions at minute-scale rates at ambient temperatures [68–83, 88–93].

In addition, bis(diimine)copper(I) complexes, $[Cu(diimine)_2]^+$, basically exhibit an absorption band in the visible light region due to the metal-to-ligand charge transfer (MLCT) transition [94–96]. Introduction of a bulky substituent into the coordination sphere is known to elongate the lifetime of the MLCT excited state of copper(I) complexes (Fig. 1.8) [94–96] because of two reasons as follows. (i) Inhibition of structural rearrangement contributes to the large energy difference between ground and photoexcited states, therefore, the nonradiative decay constant is small due to energy gap law. (ii) The additional solvent coordination, which affords nonluminessive 5-coordinated photoexcited species, can be effectively prevented by crowded coordinated structure. Typical examples for this substituent effects are reviewed by McMillin et al. [96]. Application of the emissive copper(I) complexes into optical devices has been developed by considering the steric effect around the copper center [97]. Additionally, these copper(I) complexes, especially $[Cu(dmp)_2]^+$, have been found to exhibit thermally enhanced emission, known as delayed fluorescence, derived from thermal activation between close levels in fast equilibrium, ^{1}MLCT and low-lying ^{3}MLCT excited states [103, 104]. The MLCT

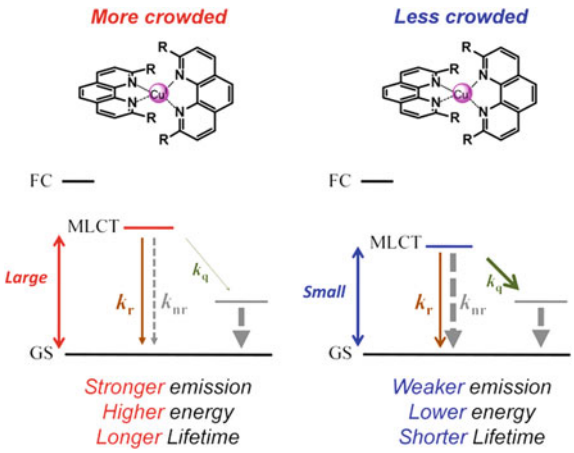

Fig. 1.8 Conceptual diagram showing the well-established unique relationship between photophysics and coordination structures. GS: ground state. FC: Franck–Condon state. Physical parameters, k_r, k_{nr}, and k_q indicate radiative, nonradiative, and solvent quenching rate constants, respectively. Inhibition of structural rearrangement in a crowded coordinated structure contribute to the larger energy difference between ground and photoexcited states, therefore, k_{nr} decreased due to energy gap law. The additional solvent coordination, which afford nonluminessive 5-coordinated photoexcited species with a small energy gap, can be effectively prevented by a crowded coordinated structure

state facilitates the photoelectron transfer (PET) process [74, 75], as in ruthenium(II) polypyridyl complexes [5].

Furthermore, the photophysics of heteloleptic copper(I) complexes bearing diimine and diphosphine ligands has attracted significant attention not only for fundamental studies pertaining to their intense luminescence [94–96, 106–111] but also for use in applications that include light-emitting devices [113–117], oxygen sensors [118], and dye-sensitized solar cells [119]. A family of $[Cu(diimine)(DPEphos)]^+$ (DPEphos = bis[2-diphenylphosphino)phenyl]ether) complexes has been particularly well studied owing to their intense luminescence [106–111]. The luminescence of $[Cu(diimine)(dppp)]^+$ (dppp = 1,3-bis(diphenylphosphino)propane) derivatives has also been examined in detail [112]. The photophysics of $[Cu(diimine)(diphosphine)]^+$ can be explained according to slightly modified models for the bis(diimine)copper(I) complexes described above [94–96, 106–111]. The lowest-lying light-excited state of $[Cu(diimine)(diphosphine)]^+$ is often found to have nature of a mixture of MLCT and LLCT (ligand to ligand charge transfer, in this case from diphosphine to diimine) [109, 117]. The complex shows heat-enhanced emission, which is discussed as delayed fluorescence derived from ^{1}CT and ^{3}CT excited state [106, 107, 116].

Properties of bis(diimine)copper(I) complexes, where 2- and 9-positions on 1,10-phenanthroline are proton, methyl, butyl, pentyl, phenyl, and other upto ten kinds of groups, have been reviewed (Fig. 1.9) [94, 95]. Bis(diimine)copper(I)

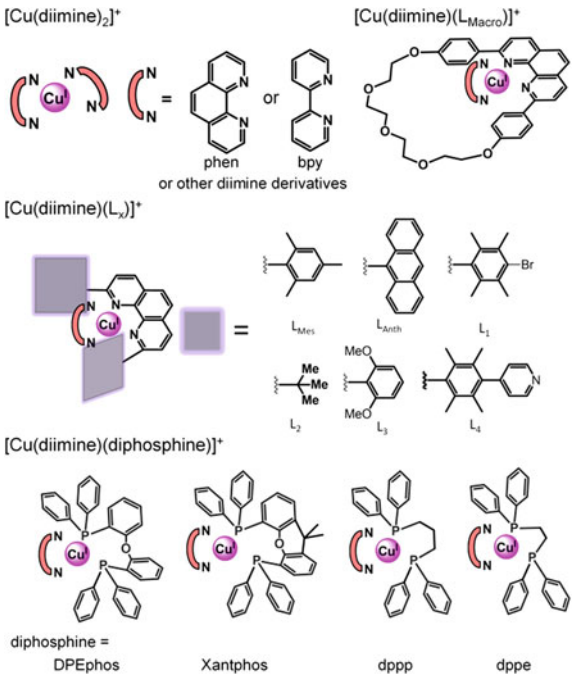

Fig. 1.9 Chemical structures of well-employed homoleptic and heteroleptic copper(I) complexes bearing two bidendate ligands including diimine derivatives

complexes bearing monomethylphenanthroline [100], bpy [80], 6,6′-dimethyl-2,2′-bipyridine [80], and recently 2,9-ditertiallybutyl,1,10-phenanthroline [101, 102], which is known to afford heteroleptic complexes described later using normal synthetic method [105], have been examined. Photophysics of a family of $[Cu(diimine)(PPh_3)_2]^+$ has been investigated [94–96], where phen [121], dmp [121], bpy [120], 6-methyl-2,2′-bipyridine [120], 4,4′-dimethyl-2,2′-bipyridine [120], and 6,6′-dimethyl-2,2′-bipyridine [120] are employed as a diimine ligand. Several types of heteroleptic copper diimine complexes bearing two different bidentate ligands have been well-investigated. Schmittel et al. have developed a useful method for synthesis of heteroleptic copper(I) complexes, $[Cu(diimine)(L_x)]^+$, using 2,9-dianthracenylphenanthroline (L_{Anth}), 2,9-dimesityl-1,10-phenanthroline (L_{Mes}), and their derivatives as an auxiliary ligand, because bulky groups at the 2- and 9-positions impede homoleptic complexation [122–125]. The ligand, 2,9-ditertiallybutyl,1,10-phenanthroline, has been also reported to afford this type of heteroleptic copper(I) diimine complexes [105]. Sauvage et al. have developed many sophisticated molecular machines using supramolecular structures based on $[Cu(diimine)(L_{macro})]^+$ derivatives [68–73]. Additionally, a family of $[Cu(diimine)(diphosphine)]^+$ has been often employed. For example, McMillin et al. and several groups have employed bis[2-(diphenylphosphino)phenyl]ether (DPEphos) [106–111, 113–119], and Tsubomura et al. have used 1,3-bis(diphenylphosphino)propane (dppp) and 1,2-bis(diphenylphosphino)ethane for investigation of luminescence [112]. 4,5-Bis(diphenylphosphino)-9,9-dimethylxanthene (xantphos) has been employed [118].

DPEphos behaves as a tridentate ligand using two phosphorus and one oxygen atoms, especially for hexagonal metal complexes such as rhenium(III) [134]. In contrast, DPEphos has been found to be basically a bidentate ligand using two phosphorus atoms in a family of $[Cu(diimine)(DPEPhos)]^+$. For example, the ether oxygen atom of DPEphos in crystal structure is generally at a nonbonding distance (>3.0 Å) [106, 107, 114, 116], which is longer than sum of van der Waals radii of oxygen and copper atoms (2.92 Å), to the metal center in a family of $[Cu(diimine)(DPEPhos)]^+$, such as phen [105, 106], bpy [107, 108], 2,9-dimethyl-1,10-phenanthroline (dmp) [105, 106], 2,9-dibutyl-1,10-phenanthroline [105, 106], 2,9-diphenethyl-1,10-phenanthroline [114], 2,9-dimethyl-4,7-diphenyl-1,10-phenanthroline [114], 2-pyridyl-pyrrolide derivatives [116]. Additionally, this type of coordination structure is reported in many $[Cu(diimine)(DPEPhos)]^+$ complexes, where 4,4′-dimethyl-2,2′-bipyridine [110], 6,6′-dimethyl-2,2′-bipyridine [110], 2-(2′-quinolyl)benzimidazole [111], 2,9-diisopropyl-1,10-phenanthroline [118], 2,2-bipyrimidine [119], 2,2-biquinoline [117], and other ligands are used. The ^1H NMR spectra of these $[Cu(diimine)(DPEPhos)]^+$ complexes in a solution state show one set of signals without contamination of other species. For example, the chemical shifts of ^1H NMR signals in $[Cu(bpy)(DPEPhos)]^+$ are similar to those in $[Cu(bpy)(PPh_3)_2]^+$, which does not have an oxygen atom [110]. Judging from these reports, coordination structure in copper complexes bearing two phosphorus atoms on DPEphos unit in both solid and solution states have been well-established.

1.3 Metal Complexes Bearing Pyridylpyrimidine Derivatives

Several groups have reported the metal complexes bearing 2-(2′-pyridyl)pyrimidine (pmpy) derivatives (Fig. 1.10) [135–143]. The ruthenium(II) complexes, such as $[Ru(Mepypm)_3]^{2+}$ (Mepypm = 4-methyl-2-(2′-pyridyl)pyrimidine), $[Ru(1)_3]^{2+}$, $[Ru(bpy)_2(1)]^{2+}$ and $[Ru(bpy)(1)_2]^{2+}$ have been investigated [135–137]. An iron(II) complex bearing **2** [138] and a copper(II) complex bearing **5** [139], have been reported. Vrieze et al. have reported pyrimidine ring rotation in palladium(II) complex bearing tridendate ligand, **3** [142]. Spiccia et al. have discussed linkage isomers due to orientation of unsymmetrically substituted pyrimidine ring, based on heteroleptic ruthenium(II) complexes bearing diimine and bidantate **4** derivative [143]. The acid sensitivities based on uncoordinated nitrogen atoms on pyrimidine unit have been often investigated by using these complexes [140, 143].

Because copper complexes have unique relation between steric effects in coordination sphere and properties (Sect. 1.2), the effects of pyrimidine ring rotation on the properties of the copper complexes were much larger than those of other metal complexes. Copper complexes bearing pmpy derivatives enable us to design a molecule whose structural responses could be converted into a different signal form, described in the next section.

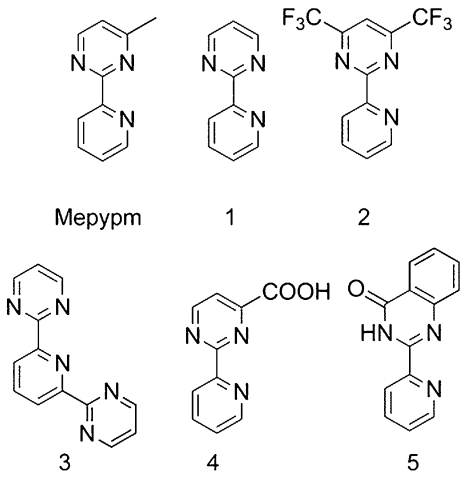

Fig. 1.10 Chemical structures of selected 2-(2′-pyridyl)pyrimidine derivatives which have been employed as a ligand for metal complexes except copper(I) ion

1.4 Pyrimidine Ring Rotation in Copper Complexes

1.4.1 The Aim of Our Previous Work

The activities of multi-stable molecules as functional units within single molecules are frequently observed in natural systems. The aim of our previous work is related to single molecular system which imitates function of five senses [144], where external stimuli are repeatedly converted into redox potential signal through gigantic molecular structure change (Fig. 1.11). Additionally, our system is related to harnessing the natural motor functions of molecules that can convert proton gradient energies across membranes into useful ATP molecules via rotational motion of the F_0 unit of ATPase [145–147]. I note that well-established redox-active molecular machines are rather related to an imitation of muscle, where redox-signal from brain can be repeatedly converted into macroscopic motions [57–73].

1.4.2 Essential Points of this System

Unique properties of copper complexes, described in Sect. 1.2, have advantages to design a molecule whose structural responses can be converted into a different signal form. Our group has demonstrated repeatable photoelectron conversion using intermolecular ligand exchange in copper complexes, considering visual sense (Sect. 1.1.2) [46]. To embed the ligand exchange within a single molecular process, we introduced a bidentate ligand consisting of a coordinated pyrimidine moiety that could effectively alternate between two possible coordination

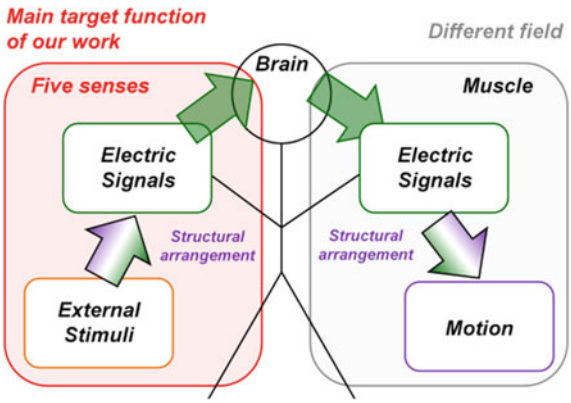

Fig. 1.11 Conceptual diagram showing functions of five senses and muscle

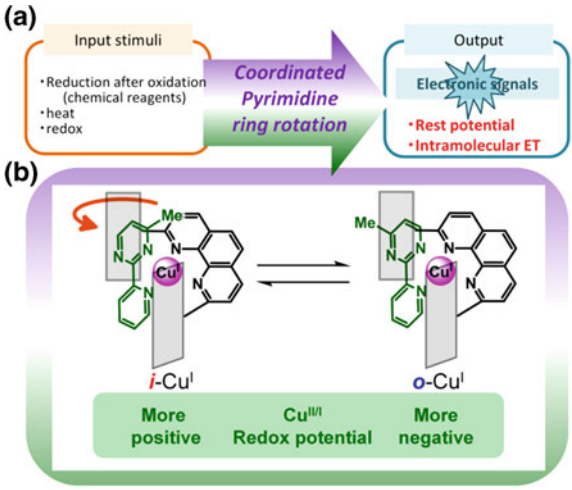

Fig. 1.12 Conceptual diagram showing **a** stimuli-convertible function of our rotational isomeric system and **b** bistability based on redox-synchronized coordinated pyrimidine *ring rotation* on copper

geometries at the copper center via rotational isomerization [148–151]. When the groups alpha to the alternate pyrimidine nitrogen atoms differed, rotational isomerization altered the steric interactions within the coordination sphere of the copper center. The interconversion between two stable isomers in copper(I) state is described in Fig. 1.12, where the notation of inner (*i*-Cu^{I}) and outer (*o*-Cu^{I}) isomers indicates the direction of the pyrimidine ring. Such steric effects induced shifts in the copper(II/I) redox potential as well as the photophysics of the resulting complex [74, 75].

The shifts arising from ring rotation have been exploited for the modulation of the electrode potential of $[Cu(Mepypm)(L_{Anth})]BF_4$ (Mepypm = 4-methyl-2-(2′-pyridyl)pyrimidine, L_{Anth} = 2,9-bis(9-anthryl)-1,10-phenanthroline) (Figs. 1.13 and 1.14) [148]. The key point for the function, rest potential switching, is the isomer ratio change of four stable isomers related to copper(II)/(I) states and rotational isomeric states, *i*-Cu^{I}, *o*-Cu^{I}, *i*-Cu^{II}, and *o*-Cu^{II}, by external-stimuli-induced switching from equilibrium and metastable states, where heating and

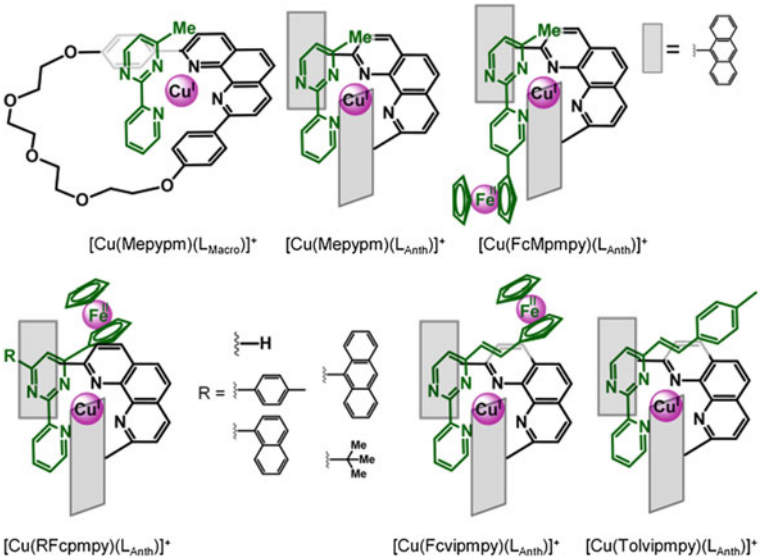

Fig. 1.13 Chemical structures of *i*-Cu^{I} in copper complexes bearing unsymmetrically substituted pyridylpyrimidine derivatives

adding chemical redox agents are performed as input stimuli. Additionally, the present redox potential response can be progressed into other types of signals via intramolecular electron transfer using [Cu(FcMpmpy)(L$_{Anth}$)]BF$_4$ (Figs. 1.13 and 1.15) [149].

Consequently, pyrimidine ring rotation in copper complexes is a powerful way to obtain functionality which can repeatedly convert input stimuli into useful output responses (Fig. 1.12).

1.4.3 Details of this System

Our group has reported details of rotational equilibrium in several copper(I) complexes bearing two bidendate diimines including pyridylpyrimidine derivatives (Fig. 1.13) [148–151]. The simplicity of the system enables us to design the motion more accurately. Mepypm was employed as a ligand in copper(I) complexes; in addition, 2,9-dianthracenyl-1,10-phenanthroline was embedded in the complex to lock the ring rotation by means of the steric effects of two anthracene planes ([Cu(Mepypm)(L$_{Anth}$)]BF$_4$, see Fig. 1.13) [148]. Because bulky groups at the 2- and 9-positions impede homoleptic complexation, the heteroleptic copper(I) complex was formed selectively. Another heteroleptic copper complex containing a macrocyclic ligand, [Cu(Mepypm)(L$_{Macro}$)]BF$_4$, was synthesized as a reference with a different steric effect on ring rotation [148].

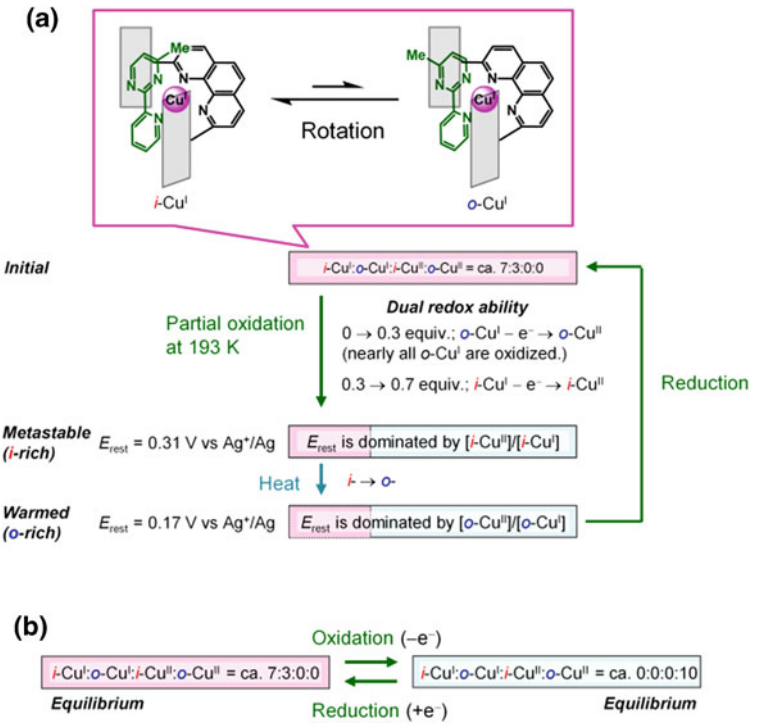

Fig. 1.14 Conceptual diagram showing the repeatable conversion of chemical energy into copper(II/I) rest potential of electrode via coordinated pyrimidine *ring rotation* of $[Cu(Me\text{-}pypm)(L_{Anth})]^+$. **a** Rest potential switching **b** cf. well established oxidation-triggered rotation

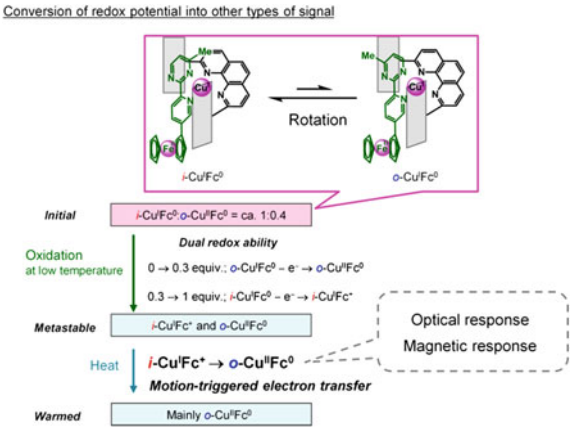

Fig. 1.15 Conceptual diagram showing the conversion of redox potential into other types of response through intramolecular electron transfer via coordinated pyrimidine *ring rotation*

The redox potential, $E°$, for the copper(II/I) redox reaction in *i*-isomer (*i*-Cu^{II}/*i*-Cu^{I} or *i*-$Cu^{II/I}$) is more positive than that in *o*-isomer (*o*-Cu^{II}/*o*-Cu^{I} or *o*-$Cu^{II/I}$) [148]. In other words, oxidation of *o*-Cu^{I} to *o*-Cu^{II} is thermodynamically more favorable than that of *i*-Cu^{I} to *i*-Cu^{II}. The reason for the redox potential shift can be explained by low relative stability of *i*-Cu^{II} according to features [148, 149] of copper complexes (Sect. 1.2), considering two factors as follows. (i): Both *i*-Cu^{I} and *o*-Cu^{I} are comparably stable in a tetrahedral geometry (preferred by copper(I)). (ii): In monooxidized state, *o*-Cu^{II} is thermodynamically much more stable than *i*-Cu^{II} in a square planar geometry (5- or 6-coordinated form preferred by copper(II)), considering the unstable crowded structure of *i*-Cu^{II}. Rotational isomerization of the bidentate ligand therefore displays dual redox potentials, the electric signal of which can be detected in the cyclic voltammogram for the copper (II/I) couple.

X-ray structural analysis has revealed that all complex cations exist as *i*-Cu^{I} in the single crystals of both [Cu(Mepypm)(L_{Anth})]BF_4 and [Cu(Mepypm)(L_{Anth})]BF_4 [148]. On the other hand, ^{1}H NMR signals derived from two rotational isomers, *i*-Cu^{I} and *o*-Cu^{I}, are observed in both [Cu(Mepypm)(L_{Anth})]BF_4 and [Cu(Mepypm)(L_{Macro})]BF_4 in the solution states [148]. Two sets of ^{1}H NMR signals at room temperature in [Cu(Mepypm)(L_{Anth})]BF_4 are much more sharpened than those of [Cu(Mepypm)(L_{Macro})]BF_4, suggesting that the rotational interconversion between *i*-Cu^{I} and *o*-Cu^{I} of [Cu(Mepypm)(L_{Anth})]BF_4 is much slower than that of [Cu(Mepypm)(L_{Macro})]BF_4.

A simulated fit of experimental cyclic voltammograms at several temperatures enables us to obtain electrochemical properties as well as rotational behaviors [148]. Results of [Cu(Mepypm)(L_{Anth})]BF_4 are summarized as follows. (I): Both *i*-Cu^{I} and *o*-Cu^{I} coexist in solution ($K_I = [o\text{-}Cu^{I}]/[i\text{-}Cu^{I}] = 0.61$). (II): In monooxidized state, *o*-Cu^{II} is much more preferred than *i*-Cu^{II} ($K_{Ii} = [o\text{-}Cu^{II}]/[i\text{-}Cu^{II}] >$ ca. 10^2). (III): Redox potential of *i*-$Cu^{II/I}$ is more positive than that of *o*-$Cu^{II/I}$ ($E^{o\prime}$for *i*-$Cu^{II/I} = 0.55$ V, $E^{o\prime}$for *o*-$Cu^{II/I} = 0.38$ V). (IV): The rate for interconversion between *i*-Cu^{I} and *o*-Cu^{I} is sufficiently slow at low temperature to trap metastable state ($k_{Ii\rightarrow o} = 1\ s^{-1}$). (V): The rate for interconversion between *i*-Cu^{II} and *o*-Cu^{II} is slower than that between *i*-Cu^{I} and *o*-Cu^{I}. The results of [Cu(Mepypm)(L_{Macro})]BF_4 are basically similar to those of [Cu(Mepypm)(L_{Anth})]BF_4 [148]. A remarkable difference between two complexes is that the rate constant of the interconversion from *i*-Cu^{I} to *o*-Cu^{I} at 293 K for [Cu(Mepypm)(L_{Macro})]BF_4 is ca. 150 times larger than that of [Cu(Mepypm)(L_{Anth})]BF_4. [Cu(Mepypm)(L_{Macro})]BF_4 is found to be not suitable to trap the metastable state.

Here, I describe how we can extract electric signal from chemical energy via pyrimidine ring rotation in copper complexes, in other words, rest potential switching (Fig. 1.14) [148]. When the system is a mixture of copper(I) and copper(II) states upon partial oxidation, the rest potential of electrode (E_{rest}) is dominated by Nernst equation which includes the ratio of rotational isomers. Since the rotational process of [Cu(Mepypm)(L_{anth})]BF_4 is frozen at low temperature, adding chemical oxidative agents sufficiently induces metastable state in partially oxidized state. Therefore, isomer ratio change of four isomers, *i*-Cu^{I}, *o*-Cu^{I}, *i*-Cu^{II},

and *o*-Cu^{II} is induced by switching between metastable, where E_{rest} is dominated by the ratio of *i*-Cu^{I} and *i*-Cu^{II}, and equilibrium, where E_{rest} is dominated by the ratio of *o*-Cu^{I} and *o*-Cu^{II}, states. The partial oxidation (0.7 equiv.) at low temperature using $[Cu(Mepypm)(L_{Anth})]^+$ leads repeatable changes in rest potential, dominated by ratio of *i*-Cu^{I}:*o*-Cu^{I}:*i*-Cu^{II}:*o*-Cu^{II}, as follows:

(1) Initial: *i*-Cu^{I}:*o*-Cu^{I}:*i*-Cu^{II}:*o*-Cu^{II} = ca. 7:3:0:0;
(2) After 0.7 equiv. oxidation: dual oxidation abilities {0–0.3 equiv. mainly *o*-Cu^{I} − e^- → *o*-Cu^{II} ($E^{\circ\prime}$ = more negative), 0.3–0.7 equiv. mainly *i*-Cu^{I} − e^- → *i*-Cu^{II} ($E^{\circ\prime}$ = more negative)} enable us to trap *i*-rich metastable state in a mixture of Cu^{I} and Cu^{II}, because both *i*-Cu^{I} → *o*-Cu^{I} and *i*-Cu^{II} → *o*-Cu^{II} are kinetically frozen;
(3) After heating: *o*-rich state in a mixture of Cu^{I} and Cu^{II} due to thermal activation of *i*- → *o*- rotation;
(4) Reduction restores the system into initial state.

The well-established oxidation triggered rotation [68–73], which corresponds to *i*-Cu^{I} – e^- → *o*-Cu^{II} (*i*-Cu^{I}:*o*-Cu^{I}:*i*-Cu^{II}:*o*-Cu^{II} = ca. 7:3:0:0 to ca. 0:0:0:10) in our system, requires the redox reaction to drive the motion. In contrast, the key process of rest potential switching, (3), proceeds without redox reaction, therefore, we can extract the rest potential response from the motion.

The present redox potential response can be progressed into other types of signals via intramolecular electron transfer (Fig. 1.15) [149]. $[Cu(FcMpmpy)(L_{Anth})]BF_4$ is employed, because redox potential of $Fc^{+/0}$ is in a range from those of *i*-$Cu^{II/I}$ and *o*-$Cu^{II/I}$. The 1 equiv. oxidation at low temperature using $[Cu(FcMpypm)(L_{Anth})]^+$ enable us to manipulate intramolecular electron transfer as follows.

(1) Initial: *i*-$Cu^{I}Fc^{0}$:*o*-$Cu^{I}Fc^{0}$ = ca. 1:0.4;
(2) After 1 equiv. oxidation: dual oxidation abilities (0–0.4 equiv. *o*-$Cu^{I}Fc^{0}$ −e^- → *o*-$Cu^{II}Fc^{0}$, 0.4–1 equiv. *i*-$Cu^{I}Fc^{0}$ − e^- → *i*-$Cu^{I}Fc^{+}$) enable us to trap *i*-rich metastable state in the oxidized state, because *i*-$Cu^{I}Fc^{+}$ → *o*-$Cu^{II}Fc^{0}$ is kinetically frozen;
(3) After heating: *o*-rich state in the oxidized state, which is accompanied by rotation-triggered intramolecular electron transfer, *i*-$Cu^{I}Fc^{+}$ → *o*-$Cu^{II}Fc^{0}$.

Oxidation of the sample at low temperature affords metastable *i*-$Cu^{I}Fc^{+}$ in divalent state, where the ferrocene unit is oxidized. Upon heating of this solution, the rotational isomerization from *i*-$Cu^{I}Fc^{+}$ to *o*-$Cu^{II}Fc^{0}$, where the ferrocene unit is neutral, proceeds via electron transfer from copper to ferrocenium ion units. This process is accompanied with the changes in the charge transfer absorption from the copper to the ferronenium as well as magnetic responses.

A redox active ferrocene moiety is used as the rotative unit instead of methyl group, using a family of $[Cu(Rpmpy)(L_{Anth})]BF_4$ [150, 151] and

[Cu(Fcvipmpy)(L_{Anth})]BF_4 [151] (Fig. 1.13). The ratio of *o*-Cu^I, [*o*-Cu^I]/([*i*-Cu^I] + [*o*-Cu^I]), in the solution state of [Cu(HFcpmpy)(L_{Anth})]$^+$ is nearly 100 %, which is much higher than that of [Cu(Mepypm)(L_{Anth})]$^+$ (ca. 30 %), because the destabilization of *i*-Cu^I compared to *o*-Cu^I by steric repulsion between the L_{Anth} moiety and the substituent on the pyrimidine moiety in [Cu(HFcpmpy)(L_{Anth})]$^+$ is much larger than that in [Cu(Mepypm)(L_{Anth})]$^+$. [Cu(Tolvipmpy)(L_{Anth})]BF_4 [151] is investigated as a reference. Although the difference in copper(II/I) redox potential between *i*- and *o*-isomers in a family of [Cu(Rpmpy)(L_{Anth})]BF_4 is small, that in ferrocenium-ion/ferrocene is sufficiently large to demonstrate oxidation-triggered rotation [150]. The intramolecular electron transfer arrangement, described in previous paragraph, is achieved using [Cu(Fcvipmpy)(L_{Anth})]BF_4 [150]. The notable feature is that this electron transfer process was accompanied by the movement of the ferrocene to the outer section of the complex.

1.5 The Aim of this Work

Our group has demonstrated that a collaboration of electrochemistry and rotational bistability using the pyrimidine ring rotational isomeric system, described in Sect. 1.5, is a powerful way to extract useful output responses from multistable molecule (Sects. 1.1, 1.2).

The aim of studies in my Ph.D course is to develop new types of properties by photofunctionalization of this molecular system (Fig. 1.16).

I studied on details of the rotational equilibrium between *i*-Cu^I and *o*-Cu^I for rational molecular design. In Chap. 2, I describe the rotational equilibrium in newly synthesized copper(I) complexes bearing a pyridylpyrimidine and a bulky diphosphine, **1**·BF_4 (**1**$^+$ = [Cu(Mepypm)(DPEphos)]$^+$, Mepypm = 4-methyl-2-(2′-pyridyl)pyrimidine, DPEphos = bis[2-(diphenylphosphino)phenyl]ether) and **2**·BF_4 (**2**$^+$ = [Cu(Mepypm)(dppp)]$^+$, dppp = 1,3-bis(diphenylphosphino)propane). I elucidate ion-pairing sensitivities of the rotational dynamics, Nature of intramolecular ligating atom exchange for the interconversion between *i*-Cu^I and *o*-Cu^I, and suitability of the common organic solution state for desired function.

Collaboration of photophysics and rotation enables me to develop a new class of emission, dual luminescence caused by the pyrimidine ring rotational isomerization (Chap. 3, using **1**$^+$), which can be a promising way to handle photophysics of metal complexes bearing π-conjugated ligand, described in Sect. 1.1.1. Whereas **2**·BF_4 showed negligible luminescence in acetone, **1**·BF_4 exhibited heat-sensitive dual luminescence. Both *i*-Cu^I and *o*-Cu^I coexist and exhibit emission at room temperature with different emission lifetime. Other properties of **1**·BF_4 and **2**·BF_4 are also described.

I demonstrated that combination of photophysics, redox activities, and rotational dynamics provides a new class of photoresponsivity, PET-driven rotational

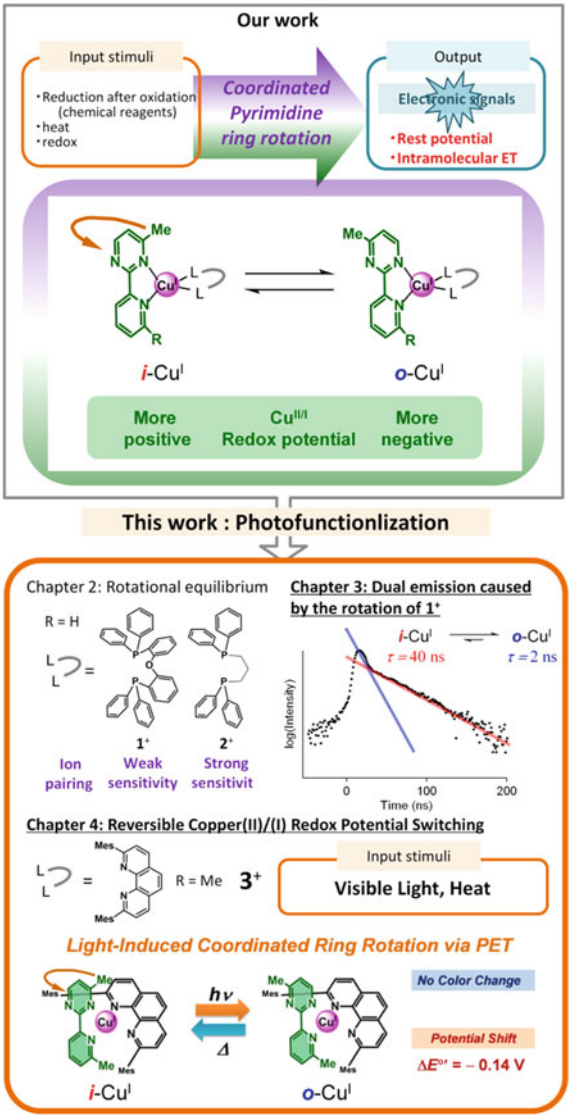

Fig. 1.16 Conceptual diagram showing the studies in my Ph.D course

isomerization with redox potential switching {Chap. 4, using $\mathbf{3}\cdot BF_4$ ($\mathbf{3}^+$ = $[Cu(MepmMepy)(L_{mes})]^+$, MepmMepy = 4-methyl-2-(6′-methyl-2′-pyridyl)pyrimidine, L_{mes} = 2,9-dimesityl-1,10-phenanthroline)}. The present photo- and heat-driven isomerization between *i*-Cu^I and *o*-Cu^I provides repeatable conversion of visible light illumination into a responsive electric signal via molecular motion. This finding is valid for electronic, magnetic, and other promising molecular signaling systems.

References

1. O'Regan B, Grätzel M (1991) Nature 353:737–740
2. Hagfeldt A, Grätzel M (2000) Acc Chem Res 33:269–277
3. Ardo S, Meyer GJ (2009) Chem Soc Rev 38:115–164
4. Hamann TW, Jensen RA, Martinson ABF, Ryswyk HV, Hupp JT (2008) Energy Environ Sci 1:66–78
5. Campagna S, Puntoriero F, Nastasi F, Bergamini G, Balzani V (2007) Top Curr Chem 280:117–214
6. Baldo MA, O'Brien DF, You Y, Shoustikov A, Sibley S, Thompson ME, Forrest SR (1998) Nature 395:151–154
7. Baldo MA, Thompson ME, Forrest SR (2000) Nature 403:750–753
8. Evans RC, Douglas P, Winscom CJ (2006) Coord Chem Rev 250:2093–2126
9. Qin T, Ding J, Wang L, Baumgarten M, Zhou G, Müllen K (2009) J Am Chem Soc 131:14329–14336
10. Meyer TJ (1989) Acc Chem Res 22:163–170
11. Concepcion JJ, Jurss JW, Brennaman MK, Hoertz PG, Patrocinio AOT, Murakami Iha NY, Templeton JL, Meyer TJ (2009) Acc Chem Res 42:1954–1965
12. Lewis NS, Nocera DG (2006) Proc Natl Sci USA 103:15729–15735
13. Lazarides T, McCormick T, Du P, Luo G, Lindley B, Eisenberg R (2009) J Am Chem Soc 131:9192–9194
14. Lo KKW, Zhang KY, Leung SK, Tang MC (2008) Angew Chem Int Ed 47:2213–2216
15. Glazer EC, Magde D, Tor Y (2007) J Am Chem Soc 129:8544–8551
16. DeAmond MK, Carlin CM (1981) Coord Chem Rev 36:325–355
17. Kubatkin S, Danilov A, Hjort M, Cornil J, Brédas J-L, Stuhr-Hansen N, Hedegård P, Bjørnholm T (2003) Nature 425:698–701
18. Park J, Pasupathy AN, Goldsmith JI, Chang C, Yaish Y, Petta JR, Rinkoski M, Sthena JP, Abruña HD, McEuen PL, Ralph DC (2002) Nature 417:722–725
19. Moth-Poulsen K, Bjørnholm T (2009) Nat Nanotechnol 4:551–556
20. Joachim C, Gimzewski JK, Aviram A (2000) Nature 408:541–548
21. Flood AH, Stoddart JF, Steuerman DW, Heath JR (2004) Science 306:2055–2056
22. Green JE, Wook Choi J, Boukai A, Bunimovich Y, Johnston-Halperin E, DeIonno E, Luo Y, Sheriff BA, Xu K, Shik Shin Y, Tseng H-R, Stoddart JF, Heath JR (2007) Nature 445:414–417
23. Sakamoto R, Katagiri S, Maeda H, Nishihara H (2013) Coord Chem Rev 257:1493–1506
24. Maeda H, Sakamoto R, Nishimori Y, Sendo J, Toshimitsu F, Yamanoi Y, Nishihara H (2011) Chem Commun 47:8644–8646
25. Kurita T, Nishimori Y, Toishimitsu F, Muratsugu S, Kume S, Nishihara H (2010) J Am Chem Soc 132:4524–4525
26. Nishimori Y, Kanaizuka K, Kurita T, Nagatsu T, Segawa Y, Toshimitsu F, Muratsugu S, Utsuno M, Kume S, Murata M, Nishihara H (2009) Chem Asian J 4:1361–1367
27. Utsuno M, Toshimitsu F, Kume S, Nishihara H (2008) Macromol Symp 270:153
28. Nishimori Y, Kanaizuka K, Murata M, Nishihara H (2007) Chem Asian J 2:367–376
29. Ohba Y, Kanaizuka K, Murata M, Nishihara H (2006) Macromol Symp 235:31
30. Kanaizuka K, Murata M, Nishimori Y, Mori I, Nishio K, Masuda H, Nishihara H (2005) Chem Lett 34:534–535
31. Simão C, Mas-Torrent M, Crivillers N, Lloveras V, Artés JM, Gorostiza P, Veciana J, Rovira C (2011) Nat Chem 3:359–364
32. Venkataramani S, Jana U, Dommaschk M, Sönnichsen FD, Tuczek F, Herges R (2011) Science 331:445–448
33. Imahori H, Tamaki K, Guldi DM, Luo C, Fujitsuka M, Ito O, Sakata Y, Fukuzumi S (2001) J Am Chem Soc 123:2607–2617

34. D'Souza F, Chitta R, Ohkubo K, Tasior M, Subbaiyan NK, Zandler ME, Rogacki MK, Gryko DT, Fukuzumi S (2008) J Am Chem Soc 130:14263–14272
35. Irie M, Fukaminato T, Sasaki T, Tamai N, Kawai T (2002) Nature 420:759–760
36. Kobatake S, Takami S, Muto H, Ishikawa T, Irie M (2007) Nature 446:778–781
37. Gorostiza P, Isacoff EY (2008) Science 322:395–399
38. Beharry AA, Sadovski O, Woolley GA (2011) J Am Chem Soc 133:19684–19687
39. Kume S, Nishihara H (2008) Dalton Trans 25:3260–3271
40. Nishihara H (2005) Coord Chem Rev 249:1468–1475
41. Nishihara H (2004) Bull Chem Soc Jpn 77:407–428
42. Kurihara M, Hirooka A, Kume S, Sugimoto M, Nishihara H (2002) J Am Chem Soc 124:8800–8801
43. Namiki K, Murata M, Kume S, Nishihara H (2011) New J Chem 35:2146–2152
44. Namiki K, Sakamoto, A, Murata M, Kume S, Nishihara H (2007) Chem Commun 44:4650–4652
45. Nagashima S, Murata M, Nishihara H (2006) Angew Chem Int Ed 45:4298–4301
46. Kume S, Murata M, Ozeki T, Nishihara H (2005) J Am Chem Soc 127:490–491
47. Umeki S, Kume S, Nishihara H (2010) Chem Lett 39:204–205
48. Kume S, Kurihara M, Nishihara H (2003) Inorg Chem 42:2194–2196
49. Muratsugu S, Kume S, Nishihara H (2008) J Am Chem Soc 130:7204–7205
50. Sakamoto R, Murata M, Nishihara H (2006) Angew Chem Int Ed 45:4793–4795
51. Hasegawa Y, Takahashi K, Kume S, Nishihara H (2011) Chem Commun 47:6846–6848
52. Takahashi K, Hasegawa Y, Sakamoto R, Nishikawa M, Kume S, Nishibori E, Nishihara H (2012) Inorg Chem 51:5188–5198
53. Uchida K, Yamanoi Y, Yonezawa T, Nishihara H (2011) J Am Chem Soc 133:9239–9241
54. Umeki S, Kume S, Nishihara H (2011) Inorg Chem 50:4925–4933
55. Fraysse S, Coudret C, Launay JP (2000) Eur J Inorg Chem 7:1581–1590
56. Tanaka Y, Inagaki A, Akita M (2007) Chem Commun 11:1169–1171
57. Muraoka T, Kinbara K, Aida T (2006) Nature 440:512–515
58. Ruangsupapichat N, Pollard MM, Harutyunyan SR, Feringa BL (2011) Nat Chem 3:53–60
59. Fletcher SP, Dumur F, Pollard MM, Feringa BL (2005) Science 310:80–82
60. Hernández JV, Kay ER, Leigh DA (2004) Science 306:1532–1537
61. Serreli V, Lee C-F, Kay ER, Leigh DA (2007) Nature 445:523–527
62. Browne WR, Feringa BL (2006) Nat Nanotechnol 1:25–35
63. Balzani V, Credi A, Venturi M (2008) Molecular devices and machines, 2nd edn. Wiley-VCH, Weinheim
64. Kay ER, Leigh DA, Zerbetto F (2007) Angew Chem Int Ed 46:72–191
65. Brouwer AM, Frochot C, Gatti FG, Leigh DA, Mottier L, Paolucci F, Roffia S, Wurpel GWH (2001) Science 291:2124–2128
66. Mobian P, Kern J-M, Sauvage J-P (2004) Angew Chem Int Ed 43:2392–2395
67. Murakami H, Kawabuchi A, Kotoo K, Kunitake M, Nakashima N (1997) J Am Chem Soc 119:7605–7606
68. Armaroli N, Balzani V, Collin J-P, Gavina P, Sauvage J-P, Ventura B (1999) J Am Chem Soc 121:4397–4408
69. Poleschak I, Kern JM, Sauvage J-P (2004) Chem Commun 474–476
70. Collin J-P, Dietrich-Buchecker C, Gaviña P, Jiménez-Molero MC, Sauvage J-P (2001) Acc Chem Res 34:477–487
71. Sauvage J-P (1998) Acc Chem Res 31:611–619
72. Livoreil A, Sauvage J-P, Armaroli N, Balzani V, Flamigni L, Ventura B (1997) J Am Chem Soc 119:12114–12124
73. Sauvage J-P (2010) Bull Jpn Soc Coord Chem 55:3–18
74. Ruthkosky M, Kelly CA, Castellano FN, Meyer GJ (1998) Coord Chem Rev 171:309–322

75. Scaltrito DV, Thompson DW, O'Callaghan JA, Meyer GJ (2000) Coord Chem Rev 208:243–266
76. Ruthkosky M, Castellano FN, Meyer GJ (1996) Inorg Chem 35:6406–6412
77. Miller MT, Gantzel PK, Karpishin TB (1998) Inorg Chem 37:2285–2290
78. Rorabacher DB (2004) Chem Rev 104:651–697
79. Le Poul N, Campion M, Douziech B, Rondelez Y, Le Clainche L, Reinaud O, Le Mest Y (2007) J Am Chem Soc 129:8801–8810
80. Meyer M, Albrecht-Gary AM, Dietrich-Buchecker CO, Sauvage J-P (1999) Inorg Chem 38:2279–2287
81. Munakata M, Endicott JF (1984) Inorg Chem 23:3693–3698
82. Munakata M, Kitagawa S, Asahara A, Masuda H (1987) Bull Chem Soc Jpn 60:1927–1929
83. Federlin P, Kern J-M, Rastegar A, Dietrich-Buchecker C, Marnot PA, Sauvage J-P (1990) New J Chem 14:9–12
84. Solomon EI, Szilagyi RK, George SD, Basumallick L (2004) Chem Rev 104:419–458
85. Lewis EA, Tolman WB (2004) Chem Rev 104:1047–1076
86. Farver O, Pecht I (2011) Coord Chem Rev 255:757–773
87. Suzuki M (2007) Acc Chem Res 40:609–617
88. Lacour J, Moraleda D (2009) Chem Commun 7073–7089
89. Hebbe-Viton V, Desvergnes V, Jodry JJ, Dietrich-Buchecker C, Sauvage J-P, Lacour J (2006) Dalton Trans 17: 2058–2065
90. Desvergnes-Breuil V, Hebbe V, Dietrich-Buchecker C, Sauvage J-P, Lacour J (2003) Inorg Chem 42:255–257
91. Hutin M, Nitschke JR (2006) Chem Commun 1724–1726
92. Riesgo E, Hu Y-Z, Bouvier F, Thummel RP (2001) Inorg Chem 40:2541–2546
93. Frei UM, Geier G (1992) Inorg Chem 31:187–190
94. Armaroli N, Accorsi G, Cardinali F, Listorti A (2007) Top Curr Chem 280:69–115
95. Lavie-Cambot A, Cantuel M, Leydet Y, Jonusauskas G, Bassani DM, McClenaghan ND (2008) Coord Chem Rev 252:2572–2584
96. McMillin DR, McNett KM (1998) Chem Rev 98:1201–1219
97. Bessho T, Constable EC, Grätzel M, Redondo AH, Housecroft CE, Kylberg W, Nazeeruddin MK, Neuburger M, Schaffner S (2008) Chem Commun 32:3717–3719
98. Lu X, Wei S, Wu C-ML, Li S, Guo W (2011) J Phys Chem C 115:3753–3761
99. Everly RM, Ziessel R, Suffert J, McMillin DR (1991) Inorg Chem 30:559–561
100. Cunningham CT, Cunningham KLH, Michalec JF, McMillin DR (1999) Inorg Chem 38:4388–4392
101. Gothard NA, Mara MW, Huang J, Szarko JM, Rolczynski B, Lockard JV, Chen LX (2012) J Phys Chem A 116:1984–1992
102. Gandhi BA, Green O, Burstyn JN (2007) Inorg Chem 46:3816–3825
103. Kirchhoff JR, Gamache RE, Blaskie MW, Paggio AD, Lengel RK, McMillin DR (1983) Inorg Chem 22:2380–2384
104. Siddique ZA, Yamamoto Y, Ohno T, Nozaki K (2003) Inorg Chem 42:6366–6378
105. Miller MT, Gantzel PK, Karpishin TB (1999) J Am Chem Soc 121:4292
106. Cuttell DG, Kuang SM, Fanwick PE, McMillin DR, Walton RA (2002) J Am Chem Soc 124:6–7
107. Kuang SM, Cuttell DG, McMillin DR, Fanwick PE, Walton RA (2002) Inorg Chem 41:3313–3322
108. Yang L, Feng JK, Ren AM, Zhang M, Ma YG, Liu XD (2005) Eur J Inorg Chem 1867–1879
109. Costa RD, Tordera D, Ortí E, Bolink HJ, Schönle J, Graber S, Housecroft CE, Constable EC, Zampese JA (2011) J Mater Chem 21:16108–16118
110. Andrés-Tomé I, Fyson J, Dias FB, Monkman AP, Iacobellis G, Coppo P (2012) Dalton Trans 41:8669–8674

111. Liu X, Sun W, Zou L, Xie Z, Li X, Lu C, Wang L, Cheng Y (2012) Dalton Trans 41:1312–1319
112. Saito K, Arai T, Takahashi N, Tsukuda T, Tsubomura T (2006) Dalton Trans 4444–4448
113. Zhang Q, Zhou Q, Cheng Y, Wang L, Ma D, Jing X, Wang F (2004) Adv Mater 16:432–436
114. Armaroli N, Accorsi G, Holler M, Moudam O, Nierengarten J-F, Zhou Z, Wegh RT, Welter R (2006) Adv Mater 18:1313–1316
115. Zhang Q, Zhou Q, Cheng Y, Wang L, Ma D, Jing X, Wang F (2006) Adv Funct Mater 16:1203–1208
116. Hsu C-W, Lin C-C, Chung M-W, Chi Y, Lee G-H, Chou P-T, Chang C-H, Chen P-Y (2011) J Am Chem Soc 133:12085–12099
117. Zhang Q, Ding J, Cheng Y, Wang L, Xie Z, Jing X, Wang F (2007) Adv Funct Mater 17:2983–2990
118. Smith CS, Branham CW, Marquardt BJ, Mann KR (2010) J Am Chem Soc 132:14079–14085
119. Linfoot CL, Richardson P, Hewat TE, Moudam O, Forde MM, Collins A, White F, Robertson N (2010) Dalton Trans 39:8945–8956
120. Del Paggio AA, McMillin DR (1983) Inorg Chem 22:691–692
121. Rader RA, McMillin DR, Buckner MT, Matthews TG, Casadonte DJ, Lengel RK, Whittaker SB, Darmon LM, Lyttle FE (1981) J Am Chem Soc 103:5906–5912
122. Schmittel M, Michel C, Wiegrefe A, Kalsani V (2001) Synthesis 10:1561–1567
123. Schmittel M, Ganz A (1997) Chem Commun 999–1000
124. Schmittel M, Michel C, Liu S-X, Schildbach D, Fenske D (2001) Eur J Inorg Chem 5: 1155–1166
125. Schmittel M, Lüning U, Meder M, Ganz A, Michel C, Herderich M (1997) Heterocycl Commun 3:493–498
126. Iwamura M, Watanabe H, Ishii K, Takeuchi S, Tahara T (2011) J Am Chem Soc 133:7728–7736
127. Vorontsov II, Graber T, Kovalevsky AY, Novozhilova IV, Gembicky M, Chen Y-S, Coppens P (2009) J Am Chem Soc 131:6566–6573
128. McCormick T, Jia W-L, Wang S (2006) Inorg Chem 45:147–155
129. Sakaki S, Mizutani H, Kase Y-I, Inokuchi K-J, Arai T, Hamada T (1996) J Chem Soc Dalton Trans 1909–1914
130. Kovalevsky AY, Gembicky M, Novozhilova IV, Coppens P (2003) Inorg Chem 42:8794–8802
131. Cunningham CT, Moore JJ, Cunningham KLH, Fanwick PE, McMillin DR (2000) Inorg Chem 39:3638–3644
132. Itoh S, Funahashi S, Koshino N, Takagi HD (2001) Inorg Chim Acta 324:252–265
133. Zahn S, Canary JW (2002) J Am Chem Soc 124:9204–9211
134. Kuang S-M, Fanwick PE, Walton RA (2002) Inorg Chem 41:405–412
135. Kawanishi Y, Kitamura N, Tazuke S (1989) Inorg Chem 28:2968–2975
136. Casalboni F, Mulazzani QG, Clark CD, Hoffman MZ, Orizondo PL, Perkovic MW, Rillema DP (1997) Inorg Chem 36:2252–2257
137. Rillema DP, Blanton CB, Shaver RJ, Jackman DC, Boldaji M, Bundy S, Worl LA, Meyer TJ (1992) Inorg Chem 31:1600–1606
138. Hearns NGR, Fatila EM, Clérac R, Jennings M, Preuss KE (2008) Inorg Chem 47:10330–10341
139. Battaglia LP, Corradi AB, Nardelli M, Pelizzi C, Tani MEV (1976) J Chem Soc, Dalton Trans 12:1076–1080
140. Zhang H, Zhang B, Li Y, Sun W (2009) Inorg Chem 48:3617–3627
141. Xue WM, Gosmami N, Eichhorn DM, Orizondo PL, Rillema DP (2000) Inorg Chem 39:4460–4467
142. Groen JH, van Leeuwen PWNM, Vrieze K (1998) J Chem Soc Dalton Trans 113–117

143. Nickita N, Gasser G, Pearson P, Belousoff MJ, Goh LY, Bond AM, Deacon GB, Spiccia L (2008) Inorg Chem 48:68–81
144. Wald G (1968) Science 162:230–239
145. Dau H, Zaharieva I (2009) Acc Chem Res 42:1861–1870
146. Vale RD, Milligan RA (2000) Science 288:88–95
147. Junge W, Sielaff H, Engelbrecht S (2009) Nature 459:364–370
148. Nomoto K, Kume S, Nishihara H (2009) J Am Chem Soc 131:3830–3831
149. Kume S, Nomoto K, Kusamoto T, Nishihara H (2009) J Am Chem Soc 131:14198–14199
150. Kume S, Nishihara H (2011) Chem Commun 47:415–417
151. Kume S, Nishihara H (2011) Dalton Trans 40:2299–2305

Chapter 2
Details of Molecular Bistability Based on Pyrimidine Ring Rotation in Copper(I) Complexes

Abstract The rational molecular design requires a detailed investigation for the equilibrium between two rotational isomers derived from orientation of pyrimidine ring. I studied on chemistry of rotational equilibrium in newly synthesized copper(I) complexes bearing two bidentate ligands, pyridylpyrimidine and bulky diphosphine, using ^{1}H NMR and single crystal X-ray structural analysis. I found that ion-pairing sensitivities of rotational bistability in the view point of both thermodynamics and kinetics, evidence for intramolecular process of interconversion, and suitability of common organic solution state for the desired function.

Keywords Copper complex · Molecular rotation · Isomerization · Ion pairing · Dynamic NMR

2.1 Introduction

2.1.1 Ion Paring in Metal Complexes

An ion pair consists an equilibrium between several different states that include the anion and cation present as a solvated contact ion pair (CIP), a solvent-shared ion pair, a solvent-separated ion pair (SSIP), and as unpaired solvated ions (Fig. 2.1) [1]. Since ion pairing between the metal complex cation and counter anion [2] (Fig. 2.1.) has often been found to play a key role in functionalization of molecular systems, detailed studies [2–10] on the solvation are valid for the development of promising materials. The ion-pairing behavior of transition metal complexes has been extensively investigated using nuclear magnetic resonance (NMR) techniques such as diffusion-ordered spectroscopy and pulsed gradient spin-echo diffusion studies [2–6]. Ion-paring causes signal splitting in the ^{1}H NMR spectra of enantiomers of metal complexes bound to a chiral anion [7–10]. In addition, the rate of the chemical exchange between such enantiomers can be determined from the peaks in the spectra at several temperatures [7–10].

M. Nishikawa, *Photofunctionalization of Molecular Switch Based on Pyrimidine Ring Rotation in Copper Complexes*, Springer Theses,
DOI: 10.1007/978-4-431-54625-2_2, © Springer Japan 2014

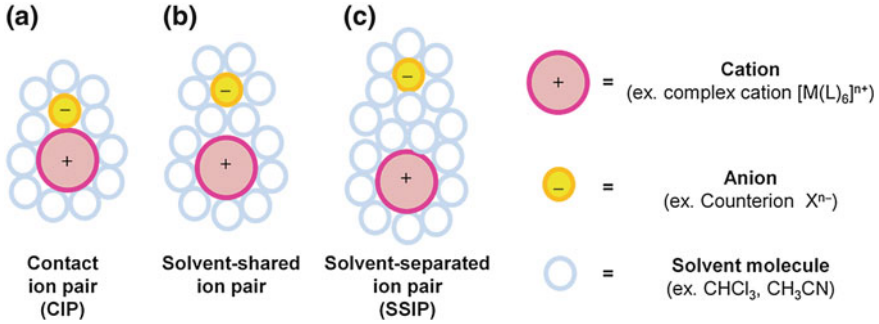

Fig. 2.1 Conceptual diagram showing transition-metal ion pairs. **a** The two contact ion pairs as outer-sphere ion pairs (CIP), **b** solvent-shared, and **c** solvent-separated ion pairs (SSIP)

2.1.2 The Aim of this Study

As I described in Sect. 1.5, pyrimidine ring rotation in copper(I) complexes is a promising system which exhibits the desired functions. The aim of this study is to examine the details of the rotational equilibrium, including ion pairing sensitivities, based on a family of $[Cu(diimine)(diphosphine)]^+$ complexes.

2.1.3 Molecular Design

As described in Sect. 1.2, a family of $[Cu(diimine)(diphosphine)]^+$ complexes has been particularly well studied owing to their intense luminescence; therefore, this class of compounds can be promising candidate for photofunctionlaiztoin of our rotational system. I describe here rotational equilibrium in newly synthesized copper(I) complexes bearing a bidentate pyridylpyrimidine and a bulky diphosphine, **1**·BF_4 (**1**$^+$ = $[Cu(Mepypm)(DPEphos)]^+$, Mepypm = 4-methyl-2-(2′-pyridyl)pyrimidine, DPEphos = bis[2-(diphenylphosphino)phenyl]ether), **1**·$B(C_6F_5)_4$, **2**·BF_4 (**2**$^+$ = $[Cu(Mepypm)(dppp)]^+$, dppp = 1,3-bis(diphenylphosphino)propane), and **2**·$B(C_6F_5)_4$ (Fig. 2.2). I employed **4**·BF_4 (**4**$^+$ = $[Cu(bpy)(DPEphos)]^+$, bpy = 2,2′-bipyridine) as a reference compound. Two kinds of non-coordinative counterions are considered [11–14], BF_4^- and $B(C_6F_5)_4^-$, where the latter is much larger than the former. The chemical equilibrium of the coordination isomers is illustrated in Fig. 2.2, where the notation of the inner (*i*-Cu^I) and outer (*o*-Cu^I) isomers describes the orientation of the pyrimidine ring.

2.1.4 Contents of this Chapter

In the present study, I investigated ion pair effects on a metal complex bistability caused by intramolecular ligating atom exchange using newly synthesized

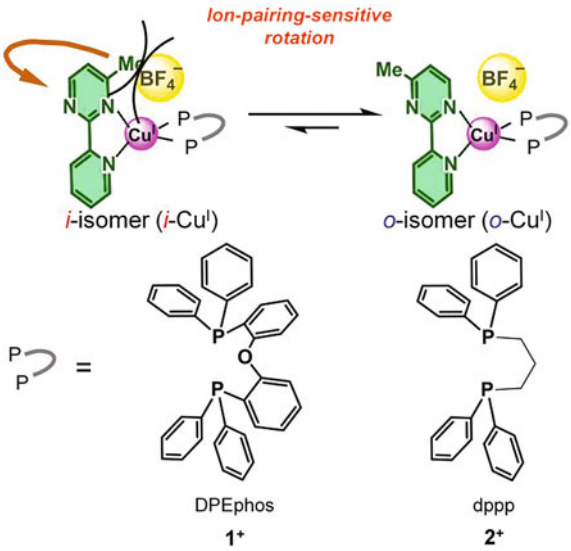

Fig. 2.2 Conceptual diagram showing the effects of ion pairing on the chemical equilibrium of pyrimidine ring rotational isomerization

heteroleptic copper(I) complexes bearing an unsymmetrically substituted pyridylpyrimidine and a bulky diphosphine ligand, **1**·BF_4, **1**·$B(C_6F_5)_4$, **2**·BF_4, and **2**·$B(C_6F_5)_4$. I found that the complex exhibited the rotational bistability in common organic solvent, and the ratio of *i*-Cu^I and *o*-Cu^I was solvent- and counterion-sensitive (Fig. 2.2). Two rotational isomers of $\mathbf{2}^+$ were separately obtained as single crystals, and the structure of each isomer was examined in detail from X-ray structural analysis. The values of enthalpy and entropy for rotational equilibrium between *i*-Cu^I and *o*-Cu^I are strongly dependent on the geometry of the diphosphine, polarity of the solvent, and the size of the counterion. Consideration of solvated counter ion pairing is a key point for rationally accounting for the effect of the weak interaction on rotational equilibrium. Since the major part of the copper center bonding surface was occupied by ligands, the position of the counterion affects the orientation of the pyrimidine moiety. I elucidate kinetics of rotational equilibrium between *i*-Cu^I and *o*-Cu^I. The interconversion between the two rotational isomers is generally an intramolecular process, as confirmed by ^1H NMR analysis of a mixed solution of two kinds of complexes.

2.2 Experimental Section

Materials. Tetrakis(acetonitrile)copper(I) tetrafluoroborate ($[Cu(MeCN)_4]BF_4$) [11], tetrakis(acetonitrile)copper(I) tetrakis(pentafluorophenyl)borate ($[Cu(MeCN)_4]B(C_6F_5)_4$) [12], and 4-methyl-2-(2′-pyridyl)pyrimidine(Mepypm) [15, 16], were prepared according to literature protocols. Bis[2-(diphenylphosphino)phenyl]ether (DPEphos) was purchased from Wako Pure Chemical

Industries, Ltd. 2,2′-Bipyridine (bpy) and 1,3-bis(diphenylphosphino)propane (dppp) were purchased from Kanto Chemicals. Other chemicals were used as purchased.

Synthesis of [Cu(Mepypm)(DPEphos)]BF_4 ($\mathbf{1}\cdot BF_4$) (Scheme 2.1). A new compound, $\mathbf{1}\cdot BF_4$, was synthesized according to a modified literature procedure [17, 18]. In this synthesis, $[Cu(MeCN)_4]BF_4$ (64 mg, 0.20 mmol) was added to DPEphos (121 mg, 0.23 mmol) in 5 mL of dichloromethane. **Mepypm** (34 mg, 0.20 mmol) in 5 mL of dichloromethane was then added, upon which the reaction solution immediately turned yellow. The reaction mixture was subsequently stirred for an additional 30 min. Diethyl ether was then added to the solution in order to precipitate the product as a yellow solid, which was filtered and washed with diethyl ether. Reprecipitation from a dichloromethane and diethyl ether mixture afforded $\mathbf{1}\cdot BF_4$ as a yellow solid with a yield of 68 % (116 mg, 0.14 mmol). ^{1}H NMR (500 MHz, $CDCl_3$, 253 K) δ 8.86 (d, $J = 5$ Hz, *i*-1H), 8.77 (d, $J = 8$ Hz, *o*-1H), 8.69 (d, $J = 8$ Hz, *i*-1H), 8.65 (d, $J = 5$ Hz, *o*-1H), 8.36 (d, $J = 5$ Hz, *i*-1H), 8.32 (d, $J = 5$ Hz, *o*-1H), 8.04 (t, $J = 8$ Hz, *o*-1H), 8.00 (t, $J = 8$ Hz, *i*-1H), 7.5–6.5 (m), 2.66 (s, *o*-3H), 2.31 (s, *i*-3H). Elemental analysis. Calculated for $C_{46}H_{37}N_3OP_2CuBF_4$: C 64.24, H 4.34, N 4.89, found C 64.19, H 4.48, N 4.78.

Synthesis of [Cu(Mepypm)(DPEphos)]$B(C_6F_5)_4$ ($\mathbf{1}\cdot B(C_6F_5)_4$) (Scheme 2.2). A new compound, $\mathbf{1}\cdot B(C_6F_5)_4$, was synthesized using a procedure similar to that described for $\mathbf{1}\cdot BF_4$ with the exception that hexane was used in place of diethyl ether. $[Cu(MeCN)_4]B(C_6F_5)_4$ (80 mg, 0.088 mmol), DPEphos (59 mg, 0.11 mmol), and Mepypm (14 mg, 0.082 mmol): Yellow solid (70 %, 83 mg). ^{1}H NMR (500 MHz, $CDCl_3$, 253 K) δ 8.76 (m, *o*-1H + *i*-1H), 8.68 (d, $J = 7.7$ Hz, *i*-1H), 8.37 (d, $J = 5.5$ Hz, *o*-1H), 8.29 (d, $J = 5.5$ Hz, *o*-1H), 8.26 (d, $J = 4.8$ Hz, *i*-1H), 7.99 (t, $J = 7.8$ Hz, *o*-1H), 7.95 (t, $J = 7.6$ Hz, *i*-1H), 7.4–6.7 (m, *i*-30H + *o*-30H), 2.63 (s, *o*-3H), 2.29 (s, *i*-3H). Elemental analysis. Calculated for $C_{70}H_{37}N_3OP_2CuBF_{20}$: C 57.89, H 2.57, N 2.89, found C 58.16, H 2.87, N 2.77.

Synthesis of [Cu(Mepypm)(dppp)]BF_4 ($\mathbf{2}\cdot BF_4$) (Scheme 2.3). A new compound, $\mathbf{2}\cdot BF_4$, was synthesized using a procedure similar to that described for $\mathbf{1}\cdot BF_4$. $[Cu(MeCN)_4]BF_4$ (67 mg, 0.20 mmol), dppp (104 mg, 0.25 mmol), and Mepypm (34 mg, 0.20 mmol): Yellow solid (56 %, 82 mg). ^{1}H NMR (500 MHz, $CDCl_3$, 253 K) δ 8.97 (d, $J = 5.0$ Hz *i*-1H), 8.93 (d, $J = 7.9$ Hz, *i*-1H), 8.85 (d, $J = 7.9$ Hz, *o*-1H), 8.79 (d, $J = 5.5$ Hz, *o*-1H), 8.47 (d, $J = 5.1$ Hz, *o*-1H), 8.35 (d, $J = 5.2$ Hz, *i*-1H), 8.20 (t, $J = 7.8$ Hz, *i*-1H), 8.11 (t, $J = 7.7$ Hz, *o*-1H), 7.69 (dd, $J = 7.5$, 5.1 Hz, *i*-1H), 7.62 (dd, $J = 7.5$, 5.2 Hz, *o*-1H), 7.5–7.1 (m, *i*-29H + *o*-29H), 2.88 (m, br), 2.69 (s + br), 2.45 (t, br), 2.32 (s, *i*-3H), 2.10 (m, br). Elemental analysis. Calculated for $C_{37}H_{35}N_3P_2CuBF_4$: C 60.54, H 4.81, N 5.73, found C 60.52, H 4.92, N 5.49.

Synthesis of [Cu(Mepypm)(dppp)]$B(C_6F_5)_4$ ($\mathbf{2}\cdot B(C_6F_5)_4$) (Scheme 2.4). A new compound, $\mathbf{2}\cdot B(C_6F_5)_4$, was synthesized using a procedure similar to that described for $\mathbf{1}\cdot B(C_6F_5)_4$ by employing $[Cu(MeCN)_4]B(C_6F_5)_4$ (185 mg, 0.20 mmol), dppp (92 mg, 0.22 mmol), and Mepypm (35 mg, 0.21 mmol). Yellow solid (40 %, 108 mg). ^{1}H NMR (500 MHz, $CDCl_3$, 253 K) δ 8.91 (d, $J = 8.0$ Hz, *i*-1H), 8.88 (m, *i*-1H + *o*-1H), 8.29 (d, $J = 5.1$ Hz, *o*-1H), 8.26 (d, $J = 4.7$ Hz,

Scheme 2.1 Synthesis of $1{\cdot}BF_4$

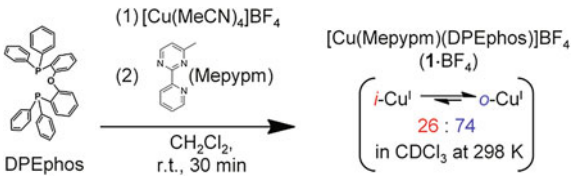

Scheme 2.2 Synthesis of $1{\cdot}B(C_6F_5)_4$

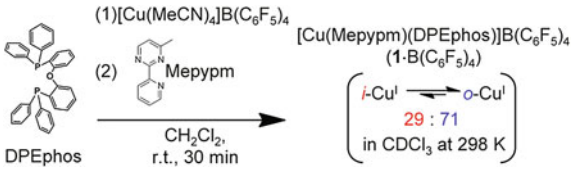

Scheme 2.3 Synthesis of $2{\cdot}BF_4$

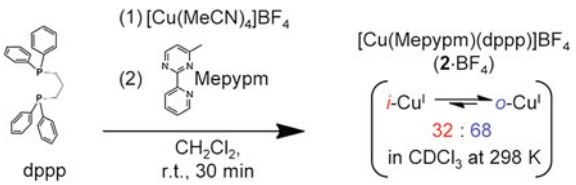

Scheme 2.4 Synthesis of $2{\cdot}B(C_6F_5)_4$

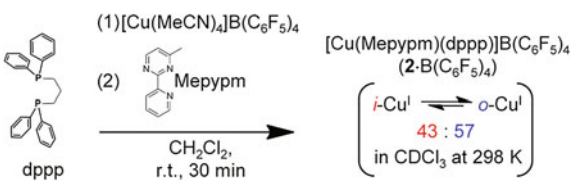

Scheme 2.5 Synthesis of $4{\cdot}BF_4$

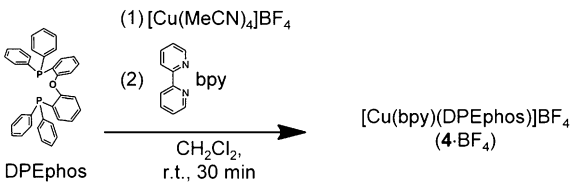

i-1H), 8.18 (d, $J = 5.5$ Hz, *o*-1H), 8.14 (t, $J = 7.8$ Hz, *i*-1H), 8.09 (t, $J = 7.9$ Hz, *o*-1H), 7.59 (dd, $J = 7.4$, 5.3 Hz, *i*-1H), 7.50 (dd, $J = 7.3$, 5.4 Hz, *o*-1H), 7.4–7.1 (m, *i*-30H + *o*-30H), 2.87 (m, br), 2.69 (s + *o*-3H), 2.57 (m, br), 2.35 (m, br), 2.23 (s, *i*-3H), 2.14 (m, br). Elemental analysis. Calculated for $C_{61}H_{35}N_3P_2CuBF_{20}$: C 55.24, H 2.66, N 3.17, found C 55.10, H 2.86, N 3.13.

Synthesis of [Cu(bpy)(DPEphos)]BF_4 (4·BF_4) (Scheme 2.5). [Cu(bpy)(DPEphos)]BF_4 was prepared according to literature methods [19]. [Cu(bpy)(DPEphos)]BF_4 was synthesized using a procedure similar to that described for $1{\cdot}B(C_6F_5)_4$ by employing $[Cu(MeCN)_4]BF_4$ (32 mg, 0.10 mmol), DPEphos

(59 mg, 0.11 mmol), and bpy (16 mg, 0.10 mmol). Yellow solid (78 %, 66 mg, 0.078 mmol). ^{1}H NMR (500 MHz, $CDCl_3$ 293 K) δ 8.49 (d, J = 7.6 Hz, py_3), 8.33 (d, J = 5.2 Hz, py_6), 8.04 (t, J = 8.0 Hz, py_4), 7.3–6.7 (m, Ph and py_5). Elemental analysis. Calculated for $C_{46}H_{36}N_2OP_2CuBF_4$: C 65.38, H 4.29, N 3.31, found C 65.17, H 4.50, N 3.27.

X-ray Structural Analysis. Yellow single crystals of *o*-**1**·BF_4·$CHCl_3$, *o*-**1**·$B(C_6F_5)_4$·1.5hexane, *o*-**2**·BF_4·0.5MeOH, and *i*-**2**·$B(C_6F_5)_4$ were obtained by slow diffusion of diethyl ether into a chloroform solution of **1**·BF_4, slow diffusion of hexane into a dichloromethane solution of **1**·$B(C_6F_5)_4$, diethyl ether into a methanol solution of **2**·BF_4, and hexane into a chloroform solution of **2**·$B(C_6F_5)_4$, respectively. Diffraction data were collected on an AFC10 diffractometer with monochromated MoK_α radiation ($\lambda = 0.7107$ Å). Lorentz polarization and numerical absorption corrections were performed with the Crystal Clear 1.3.6 program. The structure was solved by the direct method using SIR 92 software [20] and refined against F^2 using SHELXL-97 [21]. WinGX software was used to prepare the material for publication [22]. Crystallographic data are listed in Table 2.1. Disordered counterions in *o*-**2**·BF_4 were analyzed by PART, SIMU, and SADI options. The disordered methanol molecule in *o*-**2**·BF_4 was analyzed by PART, EADP, and SADI options.

Instruments. NMR spectra at several temperatures in the dark were recorded on a Bruker DRX 500 spectrometer, using a ca. 20 min data-recording interval. The experimental ^{1}H NMR spectra were simulated using iNMR 2.6.5 software. The reported chemical shifts of the solvent peaks were used for calibration of the NMR spectra in $CDCl_3$ (tetramethylsilane $\delta = 0$ ppm), CD_2Cl_2 ($\delta = 5.32$ ppm), acetone-d_6 ($\delta = 2.05$ ppm) and acetonitritrile-d_3 (CD_3CN, $\delta = 1.94$ ppm) [23].

Thermodynamic and Kinetic Analysis. The analysis was performed using the aromatic ^{1}H NMR signals of the Mepypm moiety. The results of **1**·BF_4 in $CDCl_3$, acetone-d_6, and CD_3CN were comparable with values, which were based on the methyl group of the Mepypm moiety. The solution state molar ratios of the isomers at several temperatures were determined from ^{1}H NMR signal integration. The broad spectra acquired at room temperature were excluded from the thermodynamic analysis. The generated van't Hoff plots [24] were based on an equilibrium constant corresponding to the value of [*o*-Cu^I]/[*i*-Cu^I]. The molar ratios of the *o*-Cu^I, x_o, which is equal to 100 × [*o*-Cu^I]/([*i*-Cu^I] + [*o*-Cu^I]) %, at variable temperatures were calculated by extrapolating the van't Hoff plots. The values of x_{o298} were estimated from predicted value of "ln *K*" at "1/*T*" = 1/298 K^{-1} using single linear regression of van't Hoff plots. Root-mean-square error, *s,* which reflects the error of the predicted value (ln *K*), is less than 0.017 in all data as we tested. The value, 0.017, corresponds to the 0.5 % in x_{o298}. Since the value of x_{o298} is an extrapolation number, we performed *t* test to consider the error of x_{o298}. The value is within $x_{o298} - 1\ \% < x_{o298} < x_{o298} + 1\ \%$ in 95 % significance level, even if in the case of the largest error data. The thermodynamic parameters for the *i*-Cu^I → *o*-Cu^I rotation (ΔH, ΔS, ΔG), *K*, and x_o can be represented by the following van't Hoff equations:

Table 2.1 Crystallographic data of *o*-1·BF_4·$CHCl_3$, *o*-1·$B(C_6F_5)_4$·1.5hexane, *o*-2·BF_4·0.5MeOH, and *i*-2·$B(C_6F_5)_4$

	o-**1**·BF_4·$CHCl_3$	*o*-**1**·$B(C_6F_5)_4$·1.5hexane	*o*-**2**·BF_4·0.5MeOH	*i*-**2**·$B(C_6F_5)_4$
Molecular formula	$C_{47}H_{38}BCl_3CuF_4N_3OP_2$	$C_{79}H_{58}BCuF_{20}N_3OP_2$	$C_{37.5}H_{36.5}BCuF_4N_3O_{0.5}P_2$	$C_{61}H_{35}BCuF_{20}N_3P_2$
Mw/g mol^{-1}	979.44	1581.57	749.49	1326.21
Crystal system	Triclinic	Triclinic	Triclinic	Monoclinic
Space group	P − 1	P − 1	P − 1	P21/c
T/K	113	113(2)	93(2)	113(2)
a/Å	9.661(4)	12.822(3)	12.179(5)	9.2522(12)
b/Å	13.796(5)	15.851(4)	15.881(6)	35.880(5)
c/Å	19.080(7)	19.419(5)	19.374(7)	16.941(2)
α/°	96.296(5)	78.530(10)	99.093(5)	90
β/°	94.822(3)	84.282(12)	95.012(2)	105.400(2)
γ/°	107.981(6)	67.436(9)	107.070(7)	90
V/$Å^3$	2385.5(16)	3570.5(15)	3502(2)	5422.1(13)
Z	2	2	4	4
Reflections collected	18299	28309	28206	42927
Independent reflections	10336	15651	15429	12256
R_{int}	0.0194	0.0541	0.0619	0.0431
ρ_{calcd}/g cm^{-3}	1.36	1.471	1.62	1.62
λ/Å	0.7107	0.7107	0.7107	0.7107
μ/cm^{-1}	0.746	0.452	0.77	0.577
R_1^a	0.094	0.0900	0.0988	0.0642
wR_2^b	0.2827	0.2046	0.2381	0.1416
GOF[c]	1.039	1.101	1.174	1.174

[a] $R_1 = \Sigma||F^o| - |F^c||/\Sigma|F^o| \ (I > 2\sigma(I))$
[b] $wR_2 = [\Sigma(w(F^{o2} - F^{c2})^2/\Sigma w(F^{o2})^2]^{1/2} \ (I > 2\sigma(I))$
[c] $GOF = [\Sigma(w(F^{o2} - F^{c2})^2/\Sigma(N^r - N^p)^2]$

$$\ln\{x_o/(100 - x_o)\} = \ln K = -\Delta G/RT = -\Delta H/RT + \Delta S/R \quad (2.1)$$

Here, T corresponds to the absolute temperature and R is gas constant (8.314 J K^{-1} mol^{-1}). The rate constants for the *i*-Cu^I → *o*-Cu^I isomerization, k, at several temperatures were determined from simulation analysis of the NMR spectra using the equilibrium constants determined from the van't Hoff plots. k at variable temperatures was calculated from the extrapolations of the Arrhenius plots [24]:

$$\ln k = -E_a/RT + \ln(A) \quad (2.2)$$

Here, E_a and A correspond to the activation energy and frequency factor of the *i*- → *o*-isomerization, respectively.

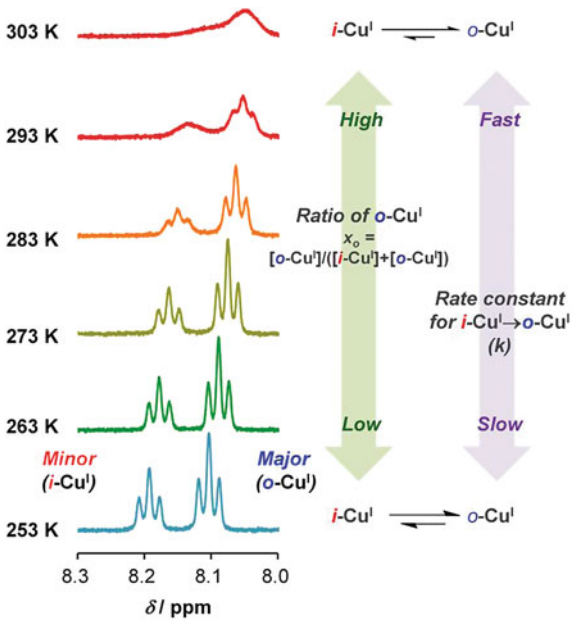

Fig. 2.3 Aromatic ^{1}H NMR signals of a Mepypm moiety in **2**·BF_4 in $CDCl_3$ at several temperatures. The signals derived from *i*-Cu^I and *o*-Cu^I are represented as *red* and *blue*, respectively. Illustration of the ratios and the rate of the rotational equilibrium is also described on the right side

2.3 Synthesis and Characterization of Rotational Equilibrium in Solution

New compounds, **1**·BF_4, **1**·$B(C_6F_5)_4$, **2**·BF_4, and **2**·$B(C_6F_5)_4$, were synthesized using a modified literature method (Sect. 2.2) [17–19]. In this approach, tetrakis(acetonitrile)copper(I) salt was reacted with a diphosphine ligand and a Mepypm ligand in dichloromethane at room temperature. The obtained compounds were characterized by ^{1}H NMR and elemental analysis.

The rotational bistability of **1**·BF_4 in $CDCl_3$, CD_2Cl_2, acetone-d_6, CD_3CN and **1**·$B(C_6F_5)_4$ in $CDCl_3$, **2**·BF_4 in $CDCl_3$, dichloromethane-d_2 (CD_2Cl_2), acetone-d_6, acetonitrile-d_3 (CD_3CN), and **2**·$B(C_6F_5)_4$ in $CDCl_3$ was characterized using ^{1}H NMR analysis to monitor chemical exchange (Figs. 2.3, 2.4, 2.5, 2.6, 2.7, 2.8, 2.9, 2.10, 2.11, 2.12, 2.13). Integration of ^{1}H NMR spectra along with line-shape analysis are well-established methods [25, 26] for investigating the thermodynamics and kinetics of a chemical equilibrium [25–36].

For example, two clearly resolved sets of signals were observed in the ^{1}H NMR spectrum of **2**·BF_4 in $CDCl_3$ at 253 K. A major singlet peak at $\delta = 2.69$ ppm and a minor one at $\delta = 2.32$ ppm were assigned as a methyl group of *o*-Cu^I and *i*-Cu^I, respectively, because of considerations as follows. (i) The chemical shift of the methyl group of *o*-Cu^I is expected to resemble that of Mepypm ($\delta = 2.67$ ppm, $CDCl_3$ at 293 K), owing to an absence of shielding effects caused by a copper center and phenyl groups on a diphosphine moiety. (ii) The shielding effects on *i*-Cu^I methyl group, which is close to both the copper and the diphosphine moieties,

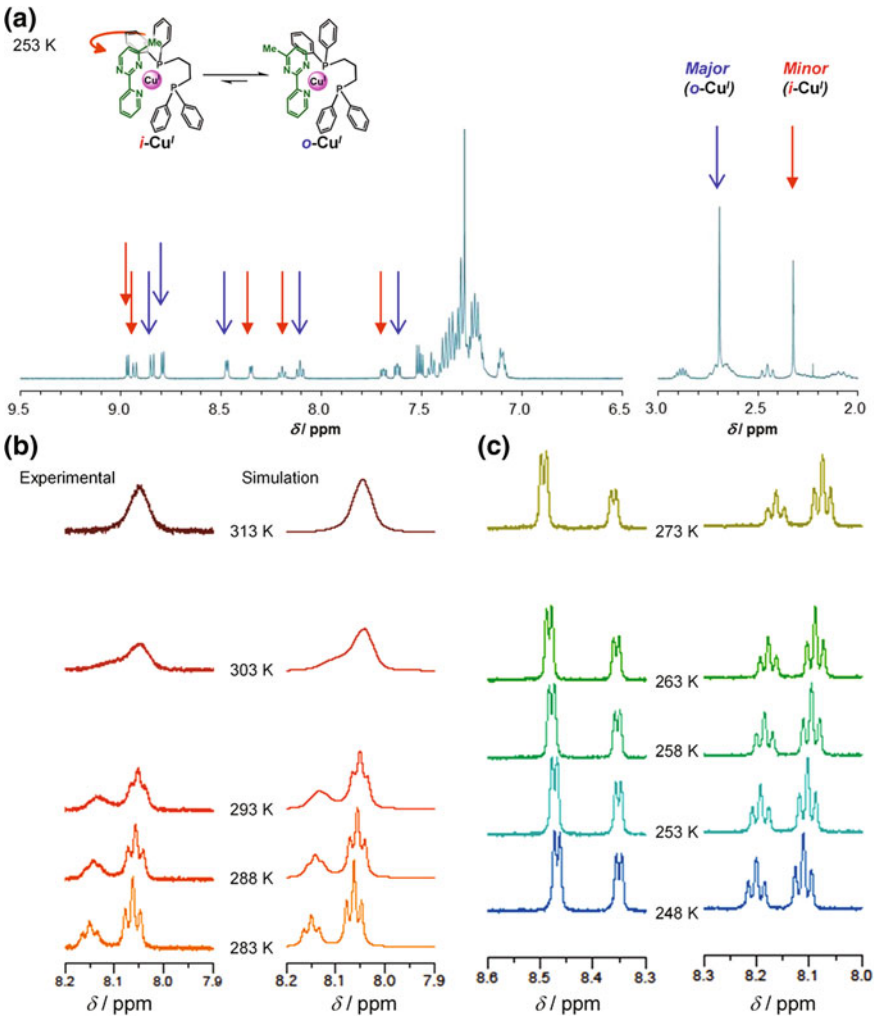

Fig. 2.4 **a** Experimental ^{1}H NMR spectra of **2**·BF_4 in $CDCl_3$ at 253 K. The signals derived from *i*-Cu^I and *o*-Cu^I are represented as *red* and *blue*, respectively. **b** Experimental (*left*) and simulated (*right*) ^{1}H NMR spectra at 313, 303, 293, and 283 K. **c** Experimental ^{1}H NMR spectra at 273, 263, 258, 253, and 248 K

are expected to cause an upfield shift of the signal. Signal splitting was also observed in the aromatic proton signals of the Mepypm ligand (Fig. 2.3). The ratio of *o*-Cu^I, estimated from integration of the minor and major signals, is represented as x_o%. The ratio of *i*-isomer is thus $(100 - x_o)$ %. Consider for instance that at 253 K, the x_o value was determined to be 60 %; the reason of higher x_o values at higher temperature is described in later sections. Upon heating, these signals broadened, indicating that two isomers, *i*-Cu^I and *o*-Cu^I, interconverted in solution

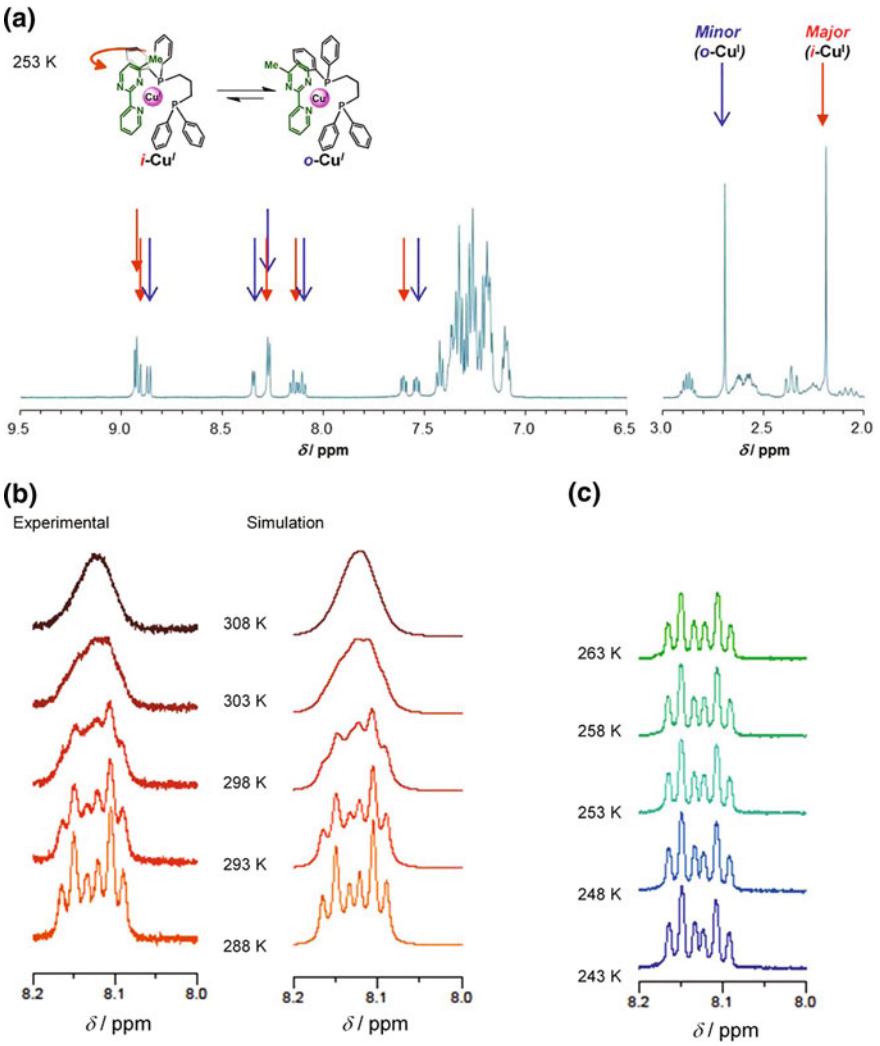

Fig. 2.5 **a** Experimental ^{1}H NMR spectra of **2**·BF_4 in CD_2Cl_2 at 253 K. **b** Experimental (*left*) and simulated (*right*) ^{1}H NMR spectra at 308, 303, 298, 293, and 288 K. **c** Experimental ^{1}H NMR spectra at 263, 258, 253, 248, and 243 K

on a timescale that is commensurate with that of the ^{1}H NMR measurement (Fig. 2.3). The rate constant for the *i*-Cu^I → *o*-Cu^I isomerization, *k*, was estimated from simulated fittings of the broadened ^{1}H NMR spectra (Fig. 2.3). For example, the value of *k* was 100 s^{-1} at 303 K; faster rate of the rotation at higher temperature is normal for chemical equilibrium. These parameters, at several temperatures and under various conditions, were determined by the same analysis as that described above.

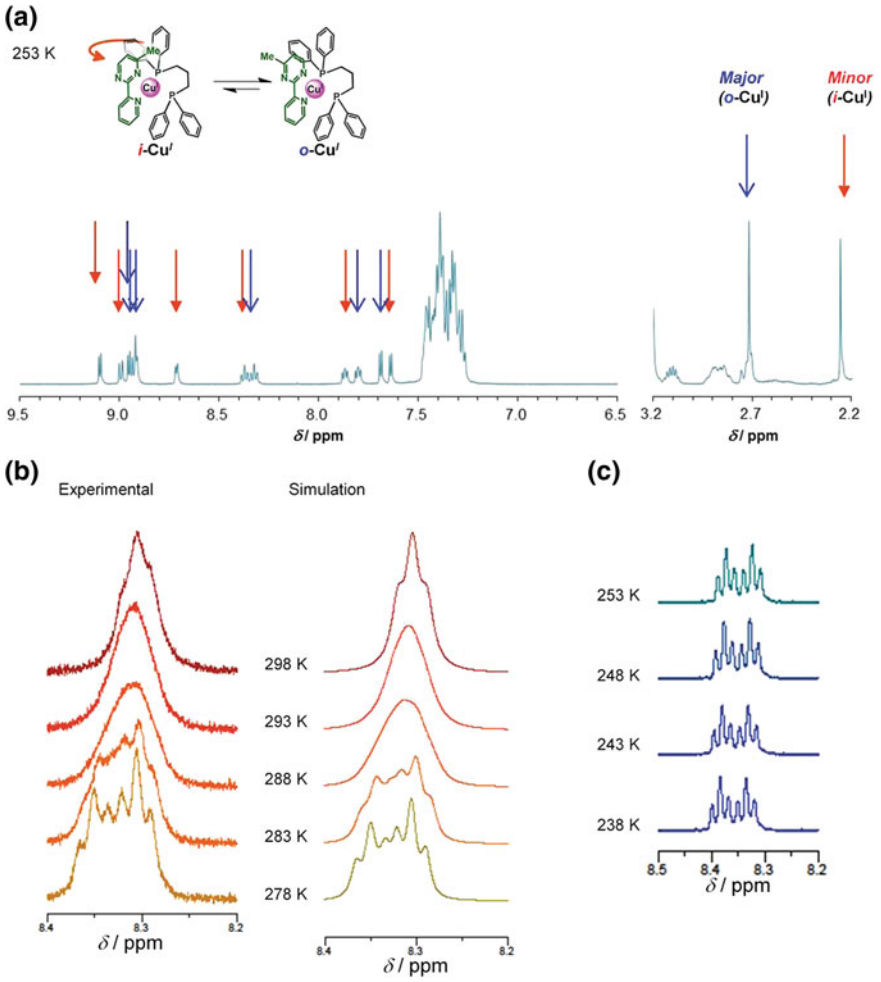

Fig. 2.6 **a** Experimental ^{1}H NMR spectra of **2**·BF_4 in acetone-d_6 at 253 K. **b** Experimental (*left*) and simulated (*right*) ^{1}H NMR spectra at 298, 293, 288, 283, and 278 K. **c** Experimental ^{1}H NMR spectra at 253, 248, 243, and 238 K

^{1}H NMR spectra of [Cu(bpy)(DPEphos)]BF_4 (**4**·BF_4), which does not undergo rotation, show only one set of signals, supporting that the signal separation mentioned above is derived from rotational isomers.

The *i*-Cu^I to *o*-Cu^I ratios and their heat-sensitivities, along with isomerization rates, are dependent on the solvent and counterion (Figs. 2.4, 2.5, 2.6, 2.7, 2.8, 2.9, 2.10, 2.11, 2.12, 2.13). However, a complete description of the observed effects requires a close consideration of the geometry of the complexes, as highlighted in later sections.

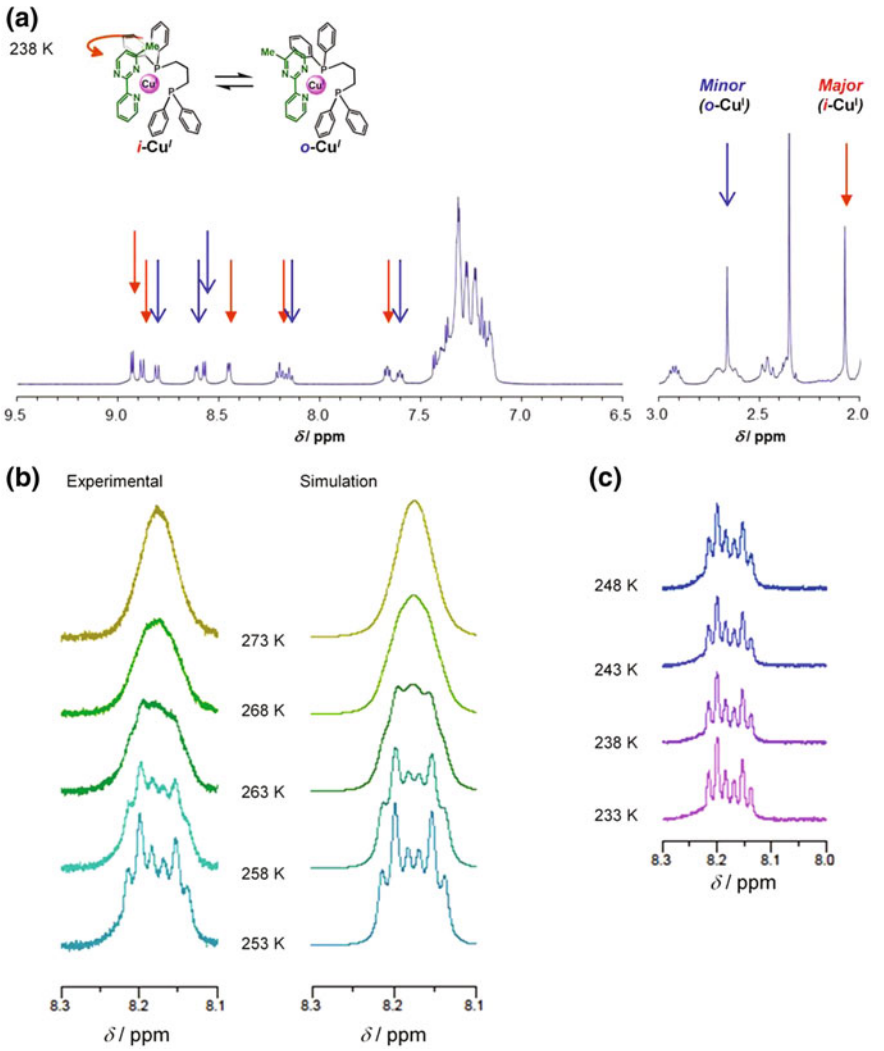

Fig. 2.7 **a** Experimental ^{1}H NMR spectra of **2**·BF_4 in CD_3CN at 238 K. **b** Experimental (*left*) and simulated (*right*) ^{1}H NMR spectra at 273, 268, 263, 258, and 253 K **c** Experimental ^{1}H NMR spectra at 248, 243, 238, and 233 K

2.4 Characterization for Intramolecular Process

The interconversion between two isomers, *i*-Cu^I and *o*-Cu^I, is generally an intramolecular ligating atom exchange process, as confirmed by ^{1}H NMR analysis of a mixed solution of [Cu(Mepypm)(DPEphos)]BF_4 (**1**·BF_4) and [Cu(bpy)(DPEphos)]BF_4 (**4**·BF_4), which does not undergo rotation [19]; This strategy is based on

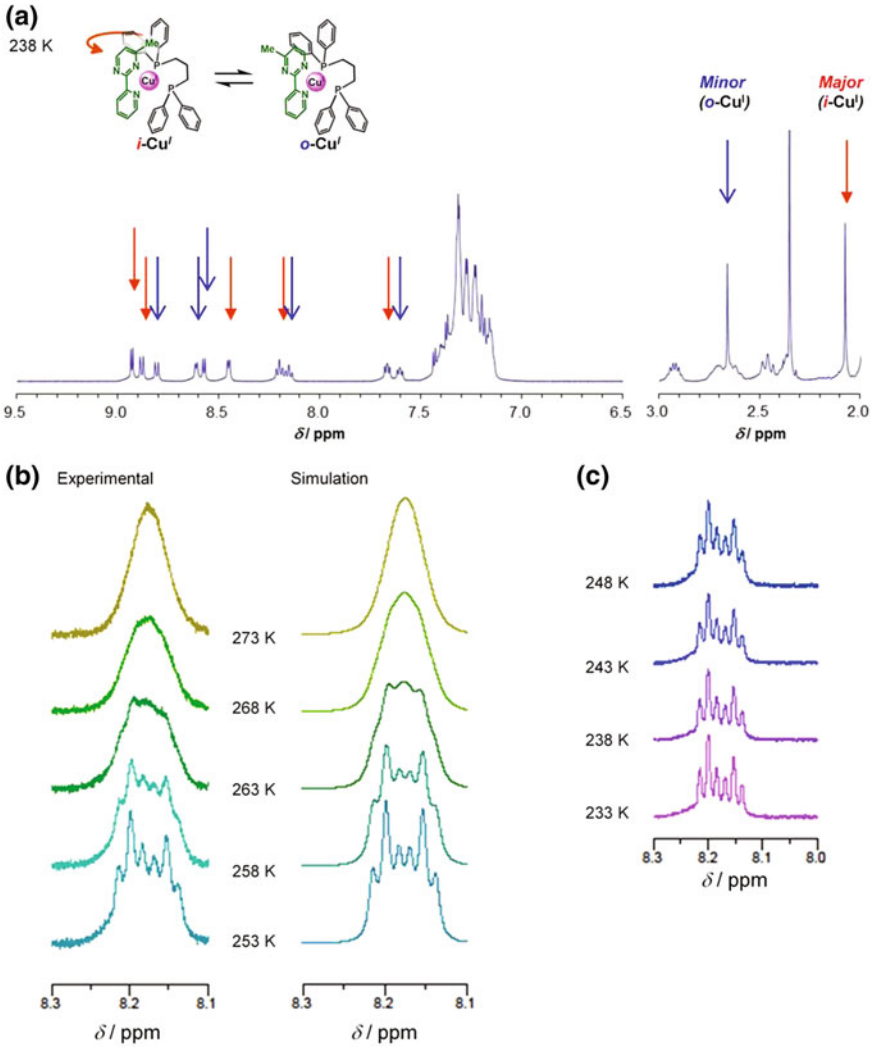

Fig. 2.8 **a** Experimental ^{1}H NMR spectra of **2**·B(C_6F_5)$_4$ in $CDCl_3$ at 273 K. **b** Experimental (*left*) and simulated (*right*) ^{1}H NMR spectra at 313, 308, 303, 298, 293, and 288 K. **c** Experimental ^{1}H NMR spectra at 278, 273, 268, 263, 258, and 253 K

modified method described in literature reported by Shionoya et al. [28]. The rate of interconversion between *i*-Cu^I and *o*-Cu^I (k) via intramolecular process is denoted as k_{intra}, that via intermolecular process is as k_{inter} ($k = k_{intra} + k_{inter}$). The value of k_{inter} is evaluated from the rate of interconversion between **4**·BF_4 and **1**·BF_4, because both processes require intermolecular diimine ligand exchange.

A ^{1}H NMR spectrum of **4**·BF_4 in acetone-d_6 at room temperature displayed one set of signals (Fig. 2.14b). Two sets of broadened signals derived from *i*-Cu^I and

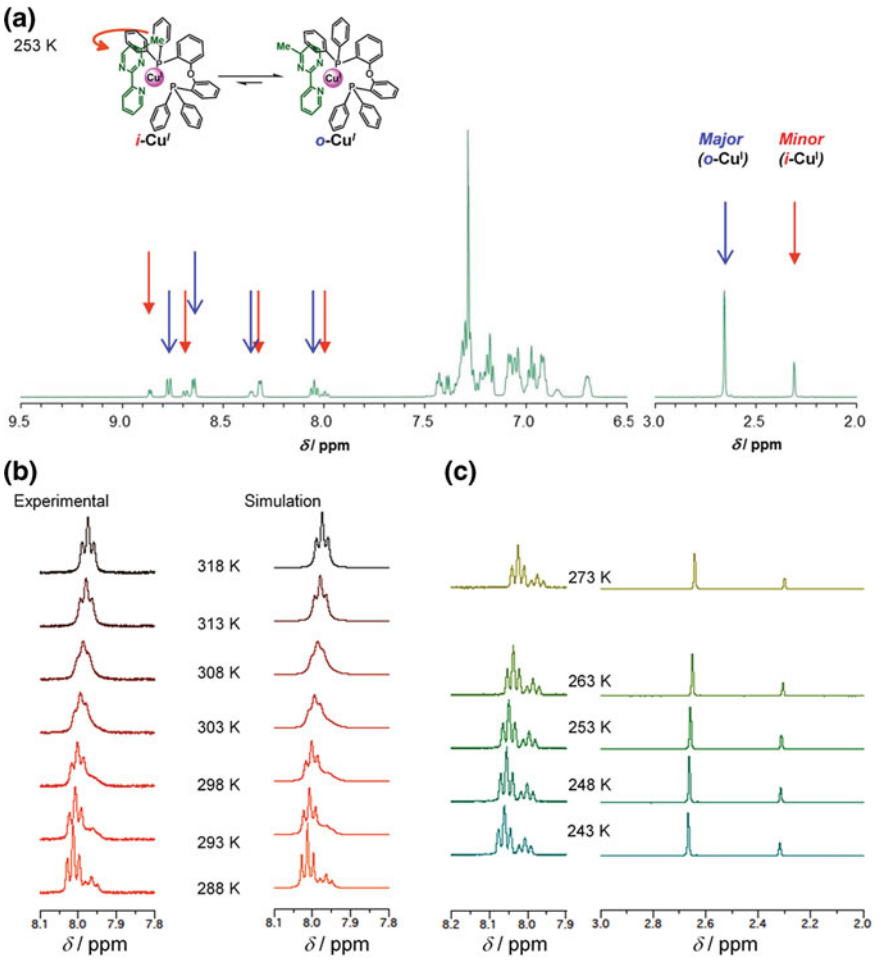

Fig. 2.9 **a** Experimental ^{1}H NMR spectra of **1**·BF_4 in $CDCl_3$ at 253 K. **b** Experimental (*left*) and simulated (*right*) ^{1}H NMR spectra at 318, 313, 308, 303, 298, 293, and 288 K. **c** Experimental ^{1}H NMR spectra at 273, 263, 253, 248, and 243 K

o-Cu^I were observed in a ^{1}H NMR spectrum of **1**·BF_4 under the same conditions (Fig. 2.14a). A ^{1}H NMR spectrum of a mixed solution of **4**·BF_4 and **1**·BF_4 under the same conditions was simply a superposition of the two spectra (Fig. 2.14c), including signals derived from diphosphine moieties, suggesting that the intermolecular interconversion between **4**·BF_4 and **1**·BF_4 via diimine ligand exchange reaction was extremely slow compared with the timescale of the ^{1}H NMR measurement (Fig. 2.14d). In addition, the ^{1}H NMR of the solution showed no signal broadening derived from **4**·BF_4 at 313 K (Fig. 2.15), where the estimated value of k was 300 s^{-1}. The rate constant for the intermolecular process under the given condition (k_{inter}) was smaller than ca. 10^0 s^{-1} ($k \gg k_{inter}$), because signal fusion

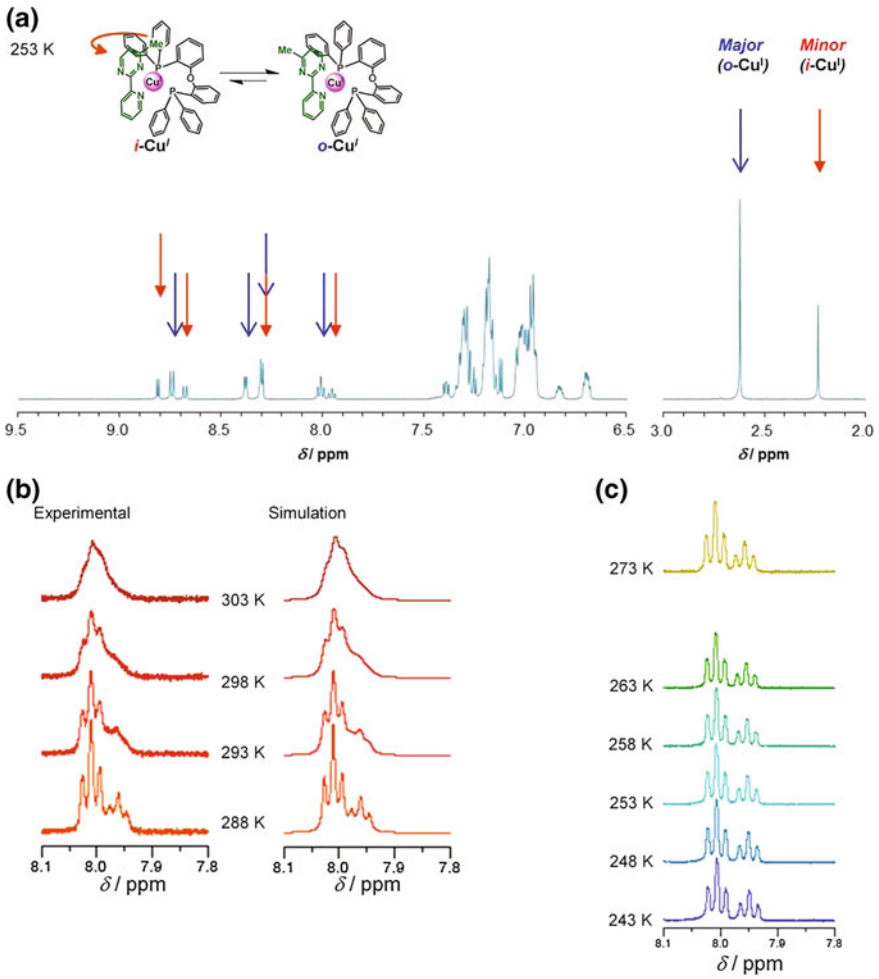

Fig. 2.10 **a** Experimental ^{1}H NMR spectra of **1**·BF_4 in CD_2Cl_2 at 253 K. **b** Experimental (*left*) and simulated (*right*) ^{1}H NMR spectra at 303, 298, 293, and 288 K. **c** Experimental ^{1}H NMR spectra at 273, 263, 258, 253, 248, and 243 K

derived from two species is observed when rate of chemical exchange between them is over a time scale of ^{1}H NMR (ca. 10^0 s^{-1}). Therefore, interconversion between *i*-Cu^I and *o*-Cu^I in typical organic solvents at ambient temperature is dominated by intramolecular process ($k_{intra} \gg k_{inter}$). Possibilities of faster intermolecular process ($k_{intra} \sim k_{inter}$ or $k_{intra} \ll k_{inter}$) can be denied from small difference in signal broadness between three species derived from *i*-, *o*-isomers of **1**·BF_4 and **4**·BF_4. This interpretation is supported by the fact that the shape of the peaks in the ^{1}H NMR spectra of **1**·BF_4 in acetone-d_6 at room temperature displayed no dependence on concentration (Fig. 2.16).

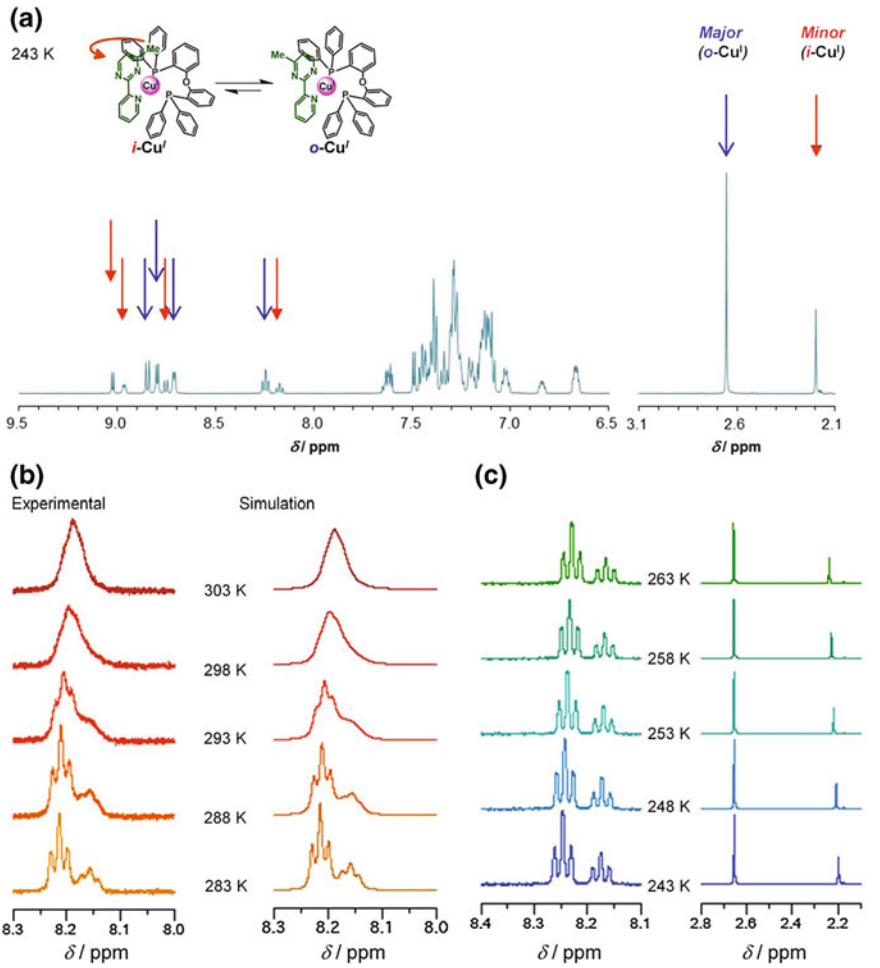

Fig. 2.11 **a** Experimental ^{1}H NMR spectra of **1**·BF_4 in acetone-d_6 at 243 K. **b** Experimental (*left*) and simulated (*right*) ^{1}H NMR spectra at 303, 298, 293, 288, and 283 K. **c** Experimental ^{1}H NMR spectra at 263, 258, 253, 248, and 243 K

This conclusion, intramolecular nature of interconversion between two rotational isomers, is additionally evidenced from similar experiment using a mixed solution of [Cu(Mepypm)(dppp)]BF_4 (**2**·BF_4) and [Cu(Mepypm)(DPEphos)]BF_4 (**1**·BF_4), which are different in diphosphine units. A ^{1}H NMR spectrum of a mixed solution of **2**·BF_4 and **1**·BF_4 (Fig. 2.17c) under the same conditions was simply a superposition of the two spectra of **2**·BF_4 and **1**·BF_4 (Fig. 2.17a, b), including signals derived from Mepypm moieties.

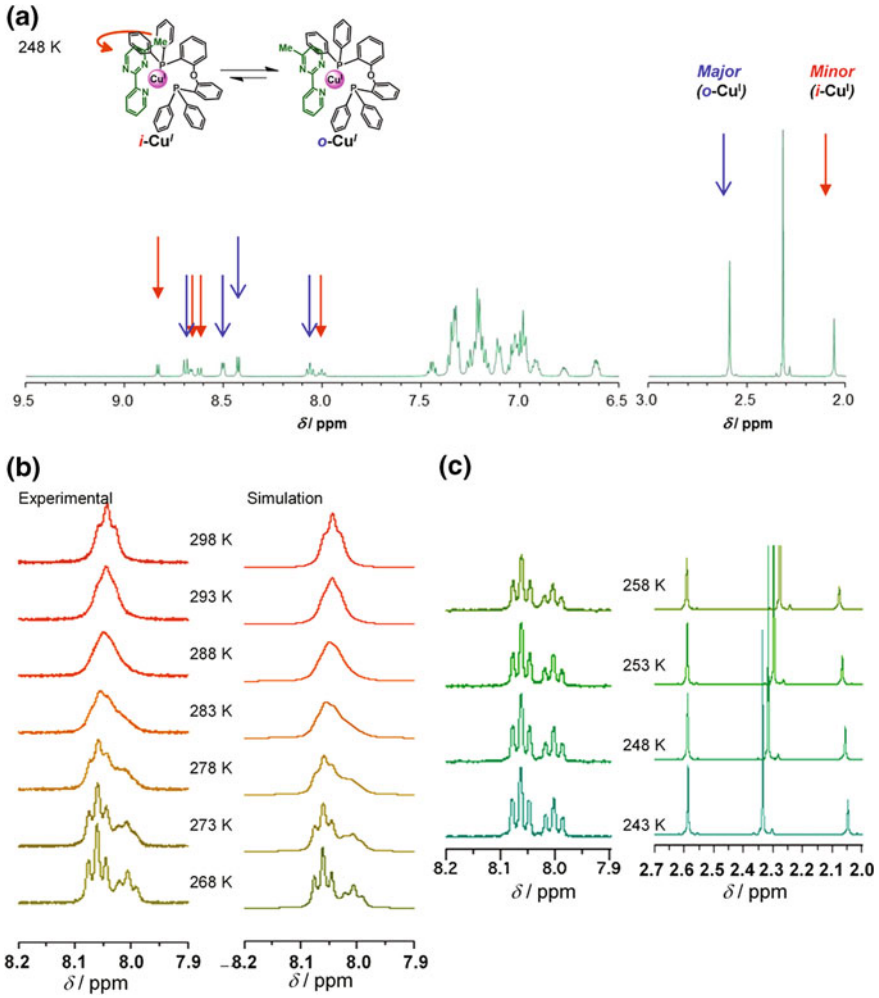

Fig. 2.12 **a** Experimental ^{1}H NMR spectra of **1**·BF_4 in CD_3CN at 248 K. **b** Experimental (*left*) and simulated (*right*) ^{1}H NMR spectra at 298, 293, 288, 283, 278, 273, and 268 K. **c** Experimental ^{1}H NMR spectra at 258, 253, 248, and 243 K

2.5 Crystallography

I performed single crystal X-ray structural analysis of **1**·BF_4, **1**·$B(C_6F_5)_4$, **2**·BF_4, and **2**·$B(C_6F_5)_4$ (Figs. 2.18, 2.19, 2.20, 2.21, 2.22, 2.23 and Table 2.1). The ratio of the complex cation to the counterion in the asymmetric unit was 1:1, suggesting that the oxidation state of the metal atom was copper(I) in the single crystal. The geometric parameters of the complex cations in **1**·BF_4, **1**·$B(C_6F_5)_4$, **2**·BF_4, and **2**·$B(C_6F_5)_4$ bond lengths were in agreement to the ones of the family of

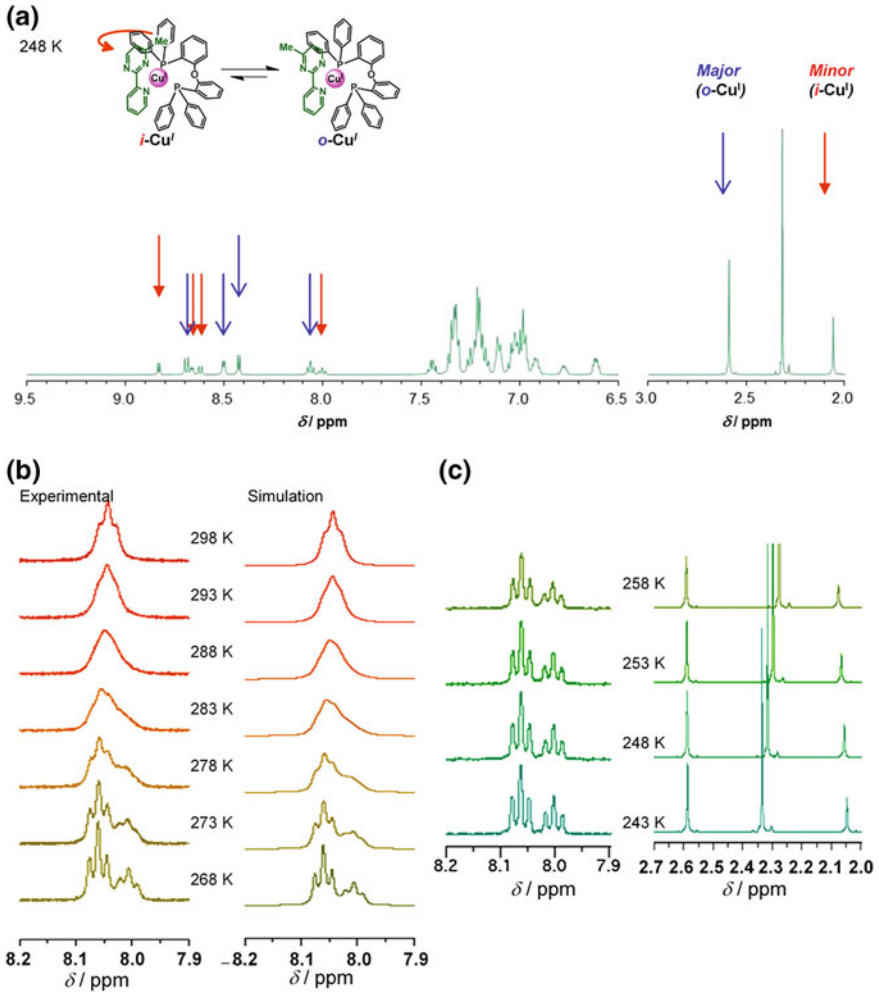

Fig. 2.13 **a** Experimental ^{1}H NMR spectra of **1**·B(C_6F_5)$_4$ in $CDCl_3$ at 248 K. **b** Experimental (*left*) and simulated (*right*) ^{1}H NMR spectra at 308, 303, 298, 293, and 283 K. **c** Experimental ^{1}H NMR spectra at 263, 253, 248, and 243 K

[Cu(diimine)(diphosphine)]$^+$ (Table 2.2) [17, 18]. I note that the distance between oxygen and copper atoms in **1**·BF_4 is found to be non-bonding region (3.18 Å), which is consistent with well-established geometries in copper(I) complexes bearing two phosphine ligating atoms in the DPEphos unit and two nitrogen ligating atoms in diimine unit; for details, see Sect. 1.2. The methyl group of the Mepypm moiety in **2**·BF_4 is oriented outward of the metal center, and no disorder was found in the coordination mode. This result suggests that all **2**$^+$ species in the single crystal exist solely as the *o*-isomer, which corresponds to a pyrimidine

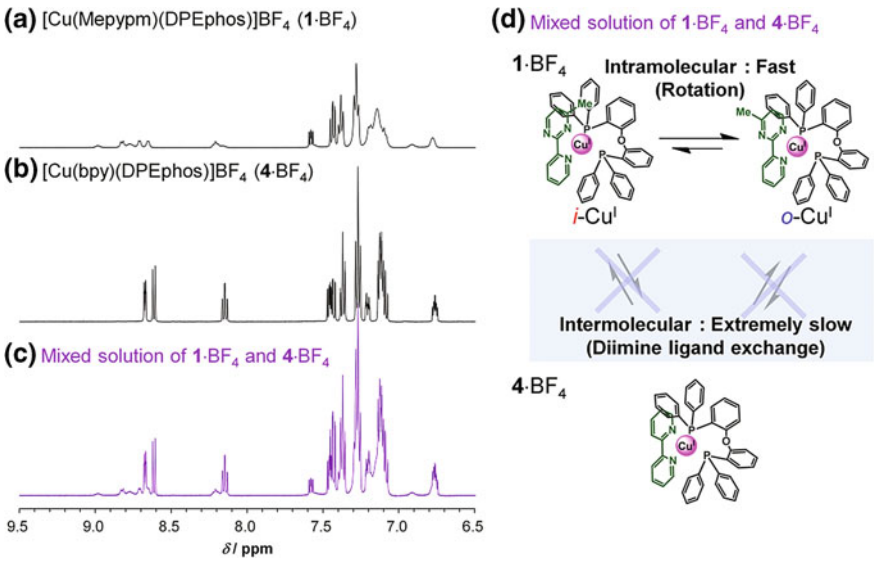

Fig. 2.14 **a**–**c** Partial ^{1}H NMR spectra of **1**·BF_4 (**a**), **4**·BF_4 (**b**), and a mixture of **1**·BF_4 and **4**·BF_4 (**c**) in acetone-d_6 in the dark at room temperature. **d** Illustration of the interconversion between species in a mixed solution of **1**·BF_4 and **4**·BF_4

moiety orientation that is identical to a crystal structure of **1**·BF_4 (Figs. 2.18a, c). In contrast, the methyl group in **2**·$B(C_6F_5)_4$ is directed toward the metal center, indicating that all $\mathbf{2}^{+}$ species exist as the *i*-isomer in the single crystal (Fig. 2.18b). Furthermore, all $\mathbf{1}^{+}$ species in **1**·$B(C_6F_5)_4$ exist as the *o*-isomer (Fig. 2.18d), which is identical to **1**·BF_4 from the viewpoint of pyrimidine orientation. Based on the orientation of pyrimidine in the crystal as well as considering the solvents to have negligible interaction with the complex cation, the four single crystals are denoted as *o*-**2**·BF_4·0.5MeOH, *i*-**2**·$B(C_6F_5)_4$, *o*-**1**·BF_4·$CHCl_3$, and *o*-**1**·$B(C_6F_5)_4$·1.5hexane.

In the case of *o*-**1**·BF_4·$CHCl_3$, the copper center is surrounded by the coordinating nitrogen atoms, a bulky diphosphine moiety, and a BF_4^- ion. The interaction of the BF_4^- ion with the copper center in *o*-**2**·BF_4·0.5MeOH is significantly stronger than in *o*-**1**·BF_4·$CHCl_3$, considering the Cu-B distance. These results reflect the reduced bulkiness of dppp, owing to the presence of fewer phenyl groups, compared with DPEphos. In contrast, the methyl group in *i*-**2**·$B(C_6F_5)_4$ is located nearer to the copper atom rather than the counter anion. $B(C_6F_5)_4^-$ is distant from the copper center owing to a large steric repulsion between $B(C_6F_5)_4^-$ and the complex cation. Because of a similar coordination geometry to *o*-**2**·BF_4·0.5MeOH, the proximity of the counterion is seemingly the primary cause for destabilization in the *i*-isomer. On the other hand, the methyl group did not cover the copper center in *o*-**1**·$B(C_6F_5)_4$·1.5hexane, which is similar to *o*-**1**·BF_4·$CHCl_3$. The results suggest that the position of the counterion has a small effect on the orientation of pyrimidine in $\mathbf{1}^{+}$, due most likely to the bulkiness of the diphosphine moiety. As a

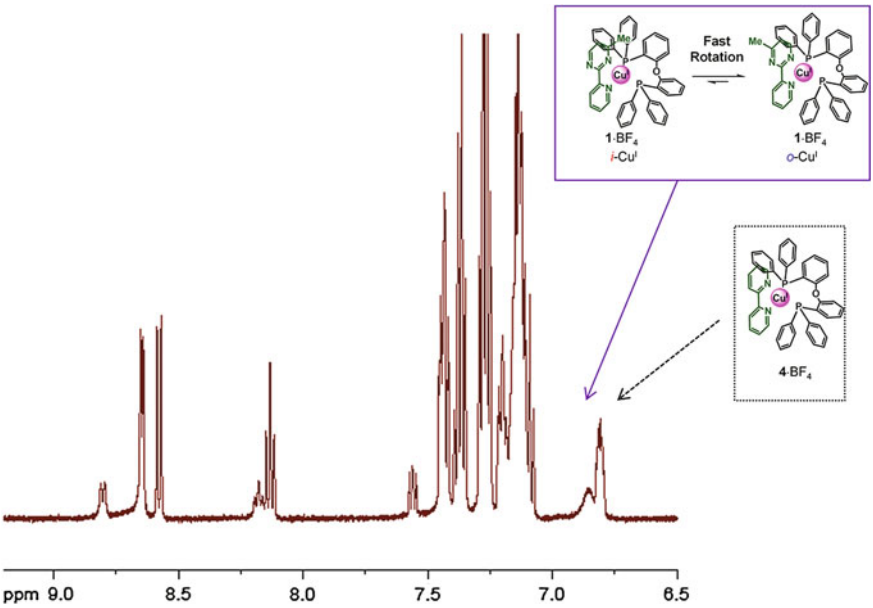

Fig. 2.15 Experimental ^{1}H NMR spectra of a mixture of **1**·BF_4 and **4**·BF_4 (*bottom*) in acetone-d_6 in the dark at 313 K. Representative signals of **1**·BF_4 and **4**·BF_4 are depicted by arrows. Since the rotation of **1**·BF_4 is fast, a fusion of the signals derived from two isomers are observed. As the interconversion between **1**·BF_4 and **4**·BF_4 is very slow, the signals of **4**·BF_4 are clearly resolved

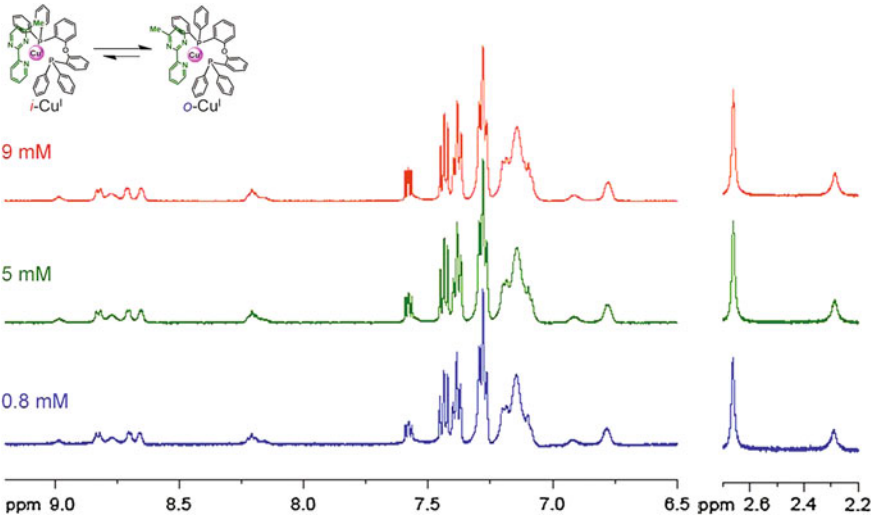

Fig. 2.16 Experimental ^{1}H NMR spectra of **1**·BF_4 in acetone-d_6 at room temperature. Concentrations of **1**·BF_4 are 9, 5, and 0.8 mM

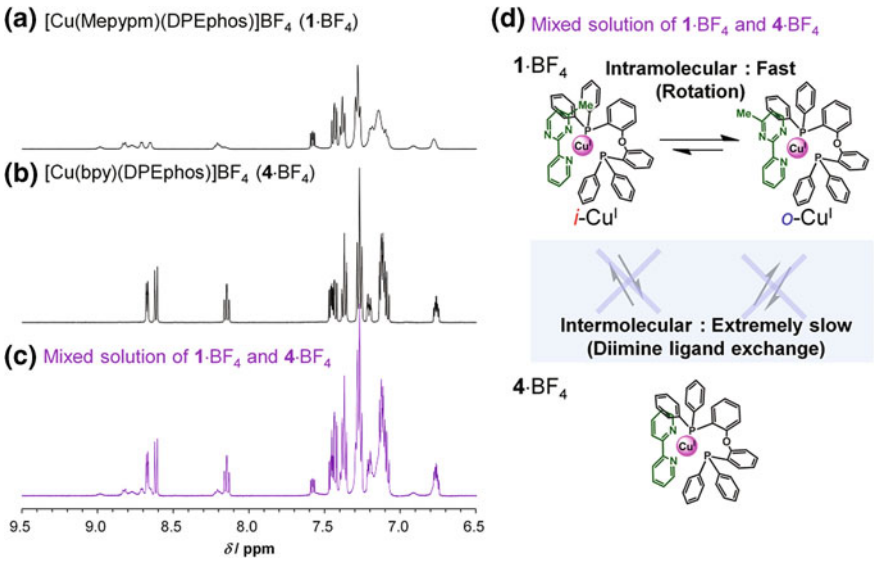

Fig. 2.17 **a**–**c** Partial ^{1}H NMR spectra of **2**·BF_4 (**a**), **1**·BF_4 (**b**), and a mixture of **1**·BF_4 and **2**·BF_4 (**c**) in acetone-d_6 in the dark at room temperature. **d** Illustration of the interconversion between species in a mixed solution of **1**·BF_4 and **2**·BF_4

result, the effects of the counterion on the rotational dynamics of $\mathbf{2}^{+}$ are expected to be more significant than those operative in $\mathbf{1}^{+}$. The aforementioned trend is characteristic of the $[Cu(Mepypm)(diphosphine)]^{+}$ family because of the geometry of the diphosphine ligand. Such behavior was not observed when bulky diimines were employed as the auxiliary ligand, such as in $[Cu(Mepypm)(L_{Anth})]^{+}$ [37]. Examination of the crystal packing in the presented complexes reveals that the proximity of other species, such as solvent molecules or another complex salt, was less than that of the nearest counterion described above (Figs. 2.20, 2.21, 2.22, 2.23). The obtained crystal structures enable us to effectively construct a reasonable model for the sensitivity of rotational equilibrium on a weak-interaction in a solution state, which is described in the following section.

2.6 Thermodynamics of Rotation in Solution

2.6.1 Results

The thermodynamics of the rotational equilibrium of **1**·BF_4, **1**·$B(C_6F_5)_4$, **2**·BF_4, and **2**·$B(C_6F_5)_4$ was examined. The values of enthalpy (ΔH), entropy (ΔS), and Gibbs free energy (ΔG) for the *i*-Cu^{I} → *o*-Cu^{I} rotation were obtained using van't Hoff plots that were estimated from integration of the ^{1}H NMR spectra at various

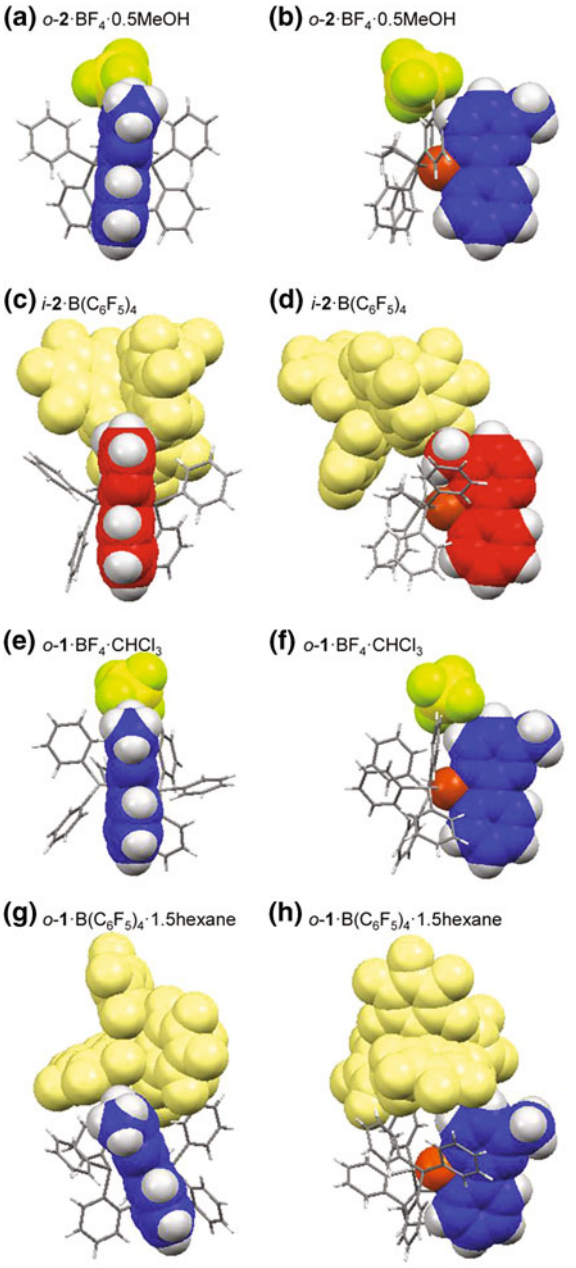

Fig. 2.18 Front (**a**, **c**, **e**, **g**) and side (**b**, **d**, **f**, **h**) views of the crystal structures of *o*-**2**·BF_4·0.5MeOH (**a**, **b**), *i*-**2**·$B(C_6F_5)_4$ (**c**, **d**), *o*-**1**·BF_4·$CHCl_3$ (**e**, **f**), and *o*-**1**·$B(C_6F_5)_4$·1.5hexane (**g**, **h**). The carbon atoms in the Mepypm moiety are colored as blue or red, which correspond to *o*- and *i*-isomers, respectively. The Mepypm moiety, the copper atom, and the counterion are drawn as a space-filling model, whereas the diphosphine moiety is included as a capped stick model. For clarity, some molecules are omitted: **a**, **b** a complex cation, a BF_4^- ion, and a methanol molecule, **e**, **f** a chloroform molecule, **g**, **h** hexane molecules

temperatures in different solvents (Fig. 2.24). A negative ΔG corresponds to a predominance of the *o*-Cu^I compared with the *i*-Cu^I; In this case, the ratio of *o*-Cu^I, $x_o = [o\text{-}Cu^I]/([o\text{-}Cu^I] + [i\text{-}Cu^I])$, is more than 50 %, and equilibrium constant,

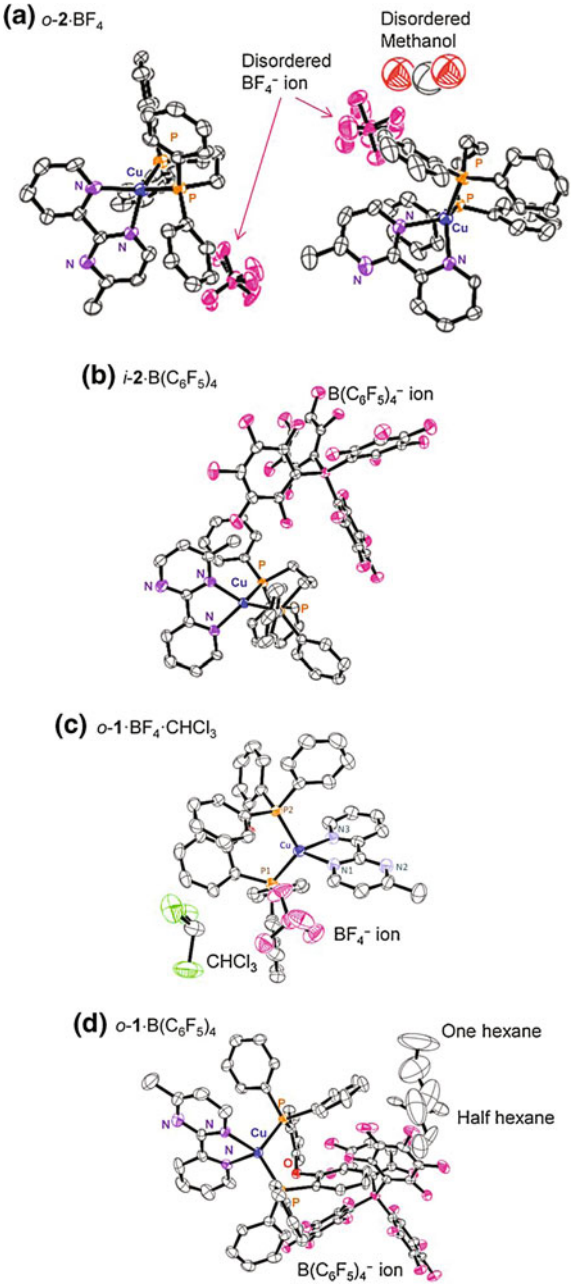

Fig. 2.19 ORTEP views of *o*-**2**·BF_4·0.5MeOH (**a**), *i*-**2**·$B(C_6F_5)_4$ (**b**), *o*-**1**·BF_4·$CHCl_3$ (**c**), and *o*-**1**·$B(C_6F_5)_4$·1.5hexane (**d**). The displacement ellipsoids are drawn at 50 % probability level. H atoms are omitted for clarity

$K = [o\text{-}Cu^I]/[i\text{-}Cu^I]$, is more than 1. A positive ΔH value corresponds to an enthalpic stabilization of *i*-Cu^I and a positive ΔS value to an entropic stabilization of *o*-Cu^I. The significant heat-sensitivity of the isomer ratios (Fig. 2.3) indicated

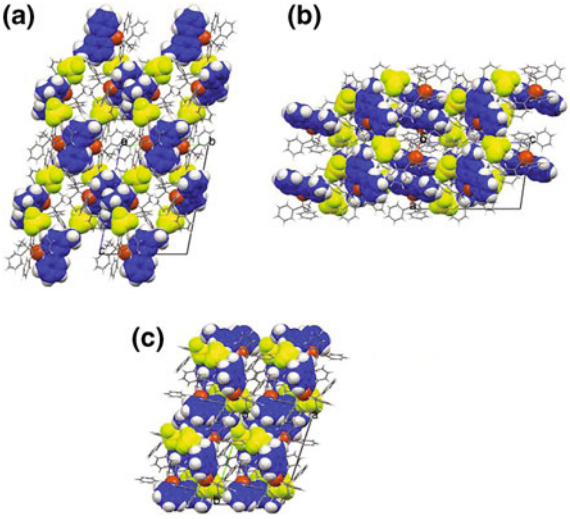

Fig. 2.20 Crystal structure of *o*-**2**·BF_4·0.5MeOH viewed along a-axis (**a**), b-axis (**b**), and c-axis (**c**). The Mepypm moiety, the copper atom and the BF_4^- ion are drawn as a space filling model, whereas the diphosphine moiety as a capped stick model

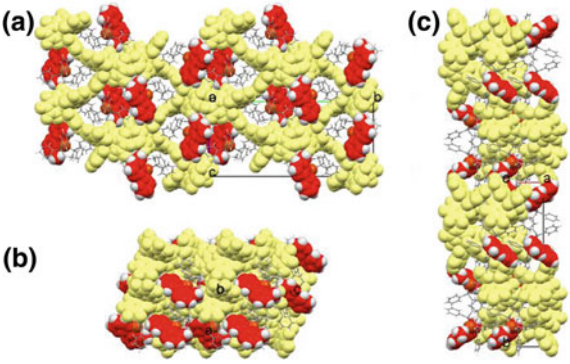

Fig. 2.21 Crystal structure of *i*-**2**·$B(C_6F_5)_4$ viewed along a-axis (**a**), b-axis (**b**), and c-axis (**c**). The Mepypm moiety, the copper atom and the BF_4^- ion are drawn as a space filling model, whereas the diphosphine moiety as a capped stick model

the large value of ΔH. I denote ΔG, x_o, and K at 298 K as ΔG_{298} x_{o298}, and K_{298}, respectively, and those at 233 K as ΔG_{233} x_{o233}, and K_{233}, respectively. Selected parameters are tabulated in Table 2.3.

The results reveal two key points: (a) the values of both ΔH and ΔS of **2**·BF_4 in $CDCl_3$ were large and positive, and (b) the values of x_{298} were reduced in more polar solvents or by making use of a larger counterion.

The values of ΔH and ΔS of **1**·BF_4 in $CDCl_3$, CD_2Cl_2, acetone-d_6, CD_3CN, and **1**·$B(C_6F_5)_4$ in $CDCl_3$ fell within a range of 0–1 kJ mol^{-1} and 6–11 J K^{-1} mol^{-1}, respectively. In contrast, both the enthalpy and entropy values for the rotation of **2**·BF_4 in $CDCl_3$ ($\Delta H = 6$ kJ mol^{-1}, $\Delta S = 25$ J K^{-1} mol^{-1}) were more positive than that tested under other conditions (Table 2.3), such as in more polar solvents CD_2Cl_2 ($\Delta H = 4$ kJ mol^{-1}, $\Delta S = 15$ J K^{-1} mol^{-1}), acetone-d_6 ($\Delta H = 3$ kJ mol^{-1}, $\Delta S = 10$ J K^{-1} mol^{-1}), and CD_3CN ($\Delta H = 3$ kJ mol^{-1}, $\Delta S = 10$ J K^{-1} mol^{-1}).

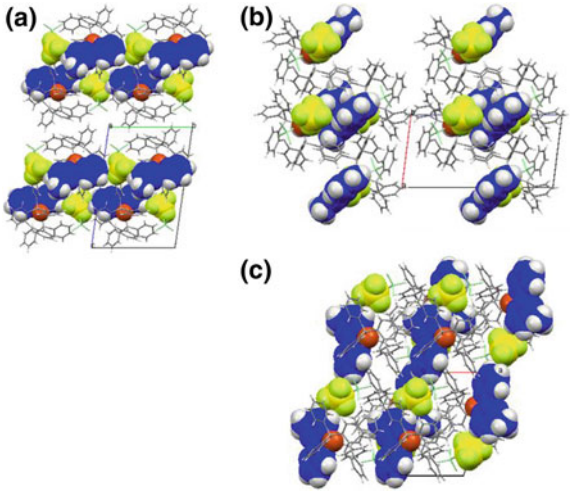

Fig. 2.22 Crystal structure of *o*-**1**·BF_4·$CHCl_3$ viewed along a-axis (**a**), b-axis (**b**), and c-axis (**c**). The Mepypm moiety, the copper atom and the BF_4^- ion are drawn as a space filling model, whereas the diphosphine moiety as a capped stick model

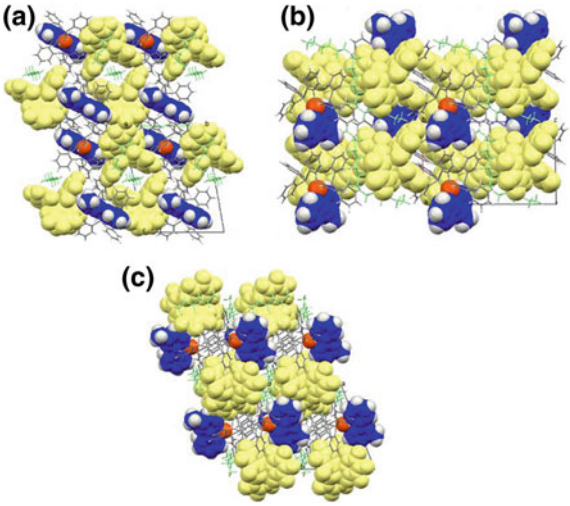

Fig. 2.23 Crystal structure of *o*-**1**·$B(C_6F_5)_4$·1.5hexane viewed along a-axis (**a**), b-axis (**b**), and c-axis (**c**). The Mepypm moiety, the copper atom and the BF_4^- ion are drawn as a space filling model, whereas the diphosphine moiety as a capped stick model

The parameters of **2**·$B(C_6F_5)_4$ in $CDCl_3$ ($\Delta H = 3$ kJ mol^{-1}, $\Delta S = 13$ J K^{-1} mol^{-1}) were more negative than those of **2**·BF_4. indicating that the solvent and counterion effects on the values of both ΔH and ΔS of $\mathbf{1}^+$ were less than those of $\mathbf{2}^+$. In all tests, the values of ΔH and ΔS of $\mathbf{2}^+$, particularly ΔH, were more positive than those of $\mathbf{1}^+$. These results suggest that the diphosphine moieties considerably affect the enthalpy and entropy for the rotational isomerization.

A lower population of the *o*-Cu^I, which corresponds to a higher value of x_o, was found in the polar solvent. The values of x_{o298} of **1**·BF_4 were 74 % in $CDCl_3$, 70 % in CD_2Cl_2, 70 % in acetone-d_6, and 65 % in CD_3CN. This trend was found not only for **1**·BF_4 but also for **2**·BF_4. The values of x_{o298} for **2**·BF_4 in CD_2Cl_2,

Table 2.2 Selected bond lengths (Å), bond angles (°), a dihedral angle (°), a torsion angle (°) of *o*-1·BF_4·$CHCl_3$, *o*-1·$B(C_6F_5)_4$·1.5hexane, *o*-2·BF_4·0.5MeOH, and *i*-2·$B(C_6F_5)_4$

	o-**1**·BF_4·$CHCl_3$	*o*-**1**·$B(C_6F_5)_4$·1.5hexane	*o*-**2**·BF_4·0.5MeOH	*i*-**2**·$B(C_6F_5)_4$
Cu–N^a_{pm}/Å	2.061(5)	2.062(4)	2.059(5) 2.063(5)	2.070(3)
Cu-N^b_{py}/Å	2.068(4)	2.092(4)	2.051(5) 2.048(5)	2.079(3)
Cu-P(1)/Å	2.2394(16)	2.2336(15)	2.2267(18) 2.2249(18)	2.2453(9)
Cu-P(2)/Å	2.2675(16)	2.2731(15)	2.2463(19) 2.246(2)	2.2561(9)
N-Cu-N/°	81.09(18)	80.24(17)	80.7(2) 80.6(2)	79.73(10)
P–Cu–P/°	114.37(5)	114.88(6)	103.45(7) 103.79(7)	102.06(3)
Dihedral anglec/°	87.21	79.04	86.6 87.96	86.22
Torsion angled/°	9.07	17.36	4.01 6.24	5.4

[a] A nitrogen atom of pyrimidine coordinating to a copper center
[b] A nitrogen atom of pyridine
[c] A dihedral angle between a N-Cu–N plane and a P–Cu–P plane
[d] A torsion angle between a pyrimidine plane and a pyridine plane

acetone-d_6, and CD_3CN were 56, 53, and 58 %, respectively, which are less than the values obtained in $CDCl_3$ (68 %). A lower population of the *o*-Cu^I, particularly in $\mathbf{2}^+$, was observed when a larger counterion was employed. The x_{o298} values of **2**·BF_4 and **2**·$B(C_6F_5)_4$ in $CDCl_3$ were 68 and 57 %, respectively. Significant counterion effects were not observed in $\mathbf{1}^+$; the ratio of **1**·$B(C_6F_5)_4$ in $CDCl_3$ ($x_{o298} = 71$ %) is slightly less than that of **1**·BF_4 in $CDCl_3$ ($x_{o298} = 74$ %). These trends are approximately observed in the full temperature range (see the van't Hoff plots in Fig. 2.24). The values of x_o of $\mathbf{1}^+$ under the conditions as we tested are almost constant over a temperature range from 233 K to 298 K. The heat-sensitivities of $\mathbf{2}^+$ are much larger than those of $\mathbf{1}^+$. For example, the population of the entropically favored *o*-Cu^I of $\mathbf{2}^+$ in $CDCl_3$ at 233 K is reduced at lower temperature ($x_o = 54$ %, $\Delta G = -0.3$ kJ mol^{-1}). Because the values of ΔH under the other conditions were relatively small, the temperature dependence of x_o and ΔG were less significant than for **2**·BF_4 in $CDCl_3$.

The parameters ΔH, ΔS, ΔG_{298}, and x_{o298} were plotted against the Kirkwood function [1], $(\varepsilon_r - 1)/(2\varepsilon_r + 1)$, where ε_r corresponds to the relative permittivity of the solvent (Fig. 2.25, $\varepsilon_r = 4.89$ for $CDCl_3$, 8.93 for CD_2Cl_2, 20.56 for acetone-d_6, and 35.94 for CD_3CN). Roughly linear relationships between the parameters and $(\varepsilon_r - 1)/(2\varepsilon_r + 1)$ indicate that solvent polarity contributes considerably to the thermodynamics of the systems considered. The slopes of the four **2**·BF_4 plots, based on a linear least square regression fitting, were much larger than those of **1**·BF_4, suggesting that $\mathbf{2}^+$ is more sensitive to solvent selection than $\mathbf{1}^+$. The

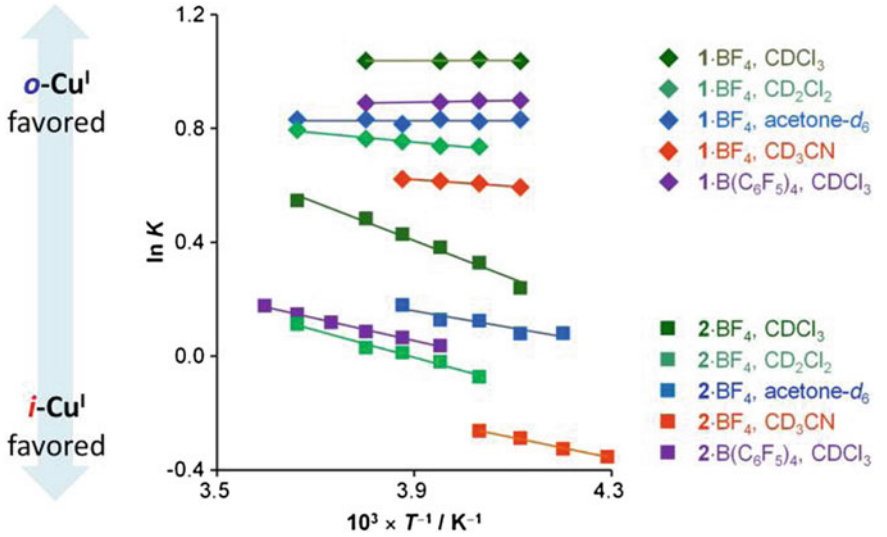

Fig. 2.24 van't Hoff plots for rotational equilibrium with the equilibrium constant, *K*, set equal to [*o*-isomer]/[*i*-isomer]

slopes of ΔG_{298} for both **1**·BF_4 and **2**·BF_4 are positive, indicating that the mechanism of the solvent dependency is similar throughout the [Cu(Me-pypm)(diphosphine)]$^+$ family. There seems to be almost no relationship between ΔG_{298} and coordination ability of solvents (negligible donating ability for $CDCl_3$ and CD_2Cl_2, 17 for acetone-d_6, and 14.1 for CD_3CN) [1].

The aforementioned weak interaction dependence of the parameters ΔH, ΔS, ΔG_{298}, and x_{o298} cannot be explained by simple consideration of chemical structures alone. For completeness, with the aid generated crystal structures, I constructed a model that considers the geometries of both the ion pair and the six-membered chelating dppp moiety, as highlighted in the following section.

2.6.2 Discussion

The geometric features of **1**$^+$ and **2**$^+$ are illustrated at Fig. 2.26a. The major bonding surface of the copper center in both **1**$^+$ and **2**$^+$ is occupied by the coordinating nitrogen atoms and the diphosphine moiety. The bonding area taken up by coordination in **2**$^+$ is reduced compared with that in **1**$^+$, which provides additional space that a counterion or a methyl group on the pyrimidine moiety can occupy. Contributions of the CIP state in $CDCl_3$ are larger than in more polar solvents such as CD_3CN (Fig. 2.26b) [1]. In other words, the population of the SSIP state in polar solvent is larger than that in less polar solvent. For clarity, I focus on the

Table 2.3 Selected thermodynamic parameters for the rotational equilibrium of [Cu(Me-pypm)(diphosphine)]$^+$ complexes under various conditions

	Solvent	ΔH^a	ΔS^b	ΔG^c_{298}	x^e_{o298}	K^g_{298}	ΔG^d_{233}	x^f_{o233}	K^h_{233}
1·BF_4	$CDCl_3$	0.0	8	−2.6	74	2.8	−2.0	74	2.8
1·BF_4	CD_2Cl_2	1.3	11	−2.1	70	2.3	−1.3	67	2.0
1·BF_4	Acetone-d_6	0.0	7	−2.1	70	2.3	−1.6	70	2.3
1·BF_4	CD_3CN	0.2	6	−1.6	65	1.9	−1.2	65	1.8
1·$B(C_6F_5)_4$	$CDCl_3$	−0.2	6	−2.2	71	2.4	−1.7	71	2.5
2·BF_4	$CDCl_3$	5.6	25	−1.9	68	2.2	−0.3	54	1.2
2·BF_4	CD_2Cl_2	4.0	15	−0.6	56	1.3	0.4	45	0.8
2·BF_4	Acetone-d_6	2.5	10	−0.3	58	1.4	−0.1	51	1.0
2·BF_4	CD_3CN	3.0	10	0.0	50	1.0	0.7	41	0.7
2·$B(C_6F_5)_4$	$CDCl_3$	3.3	13	−0.7	57	1.3	0.2	48	0.9

[a] Enthalpy for *i*-Cu^I → *o*-Cu^I rotation/kJ mol^{-1}
[b] Entropy for *i*-Cu^I → *o*-Cu^I rotation/J K^{-1} mol^{-1}
[c,d] Gibbs free energy for *i*-Cu^I → *o*-Cu^I rotation at [c] 298 K and [d] 233 K/kJ mol^{-1}
[e,f] Molar ratio of *o*-Cu^I at [e] 298 K and [f] 233 K/ %
[g,h] Equilibrium constant, [*o*-Cu^I]/[*i*-Cu^I] at [g] 298 K and [h] 233 K

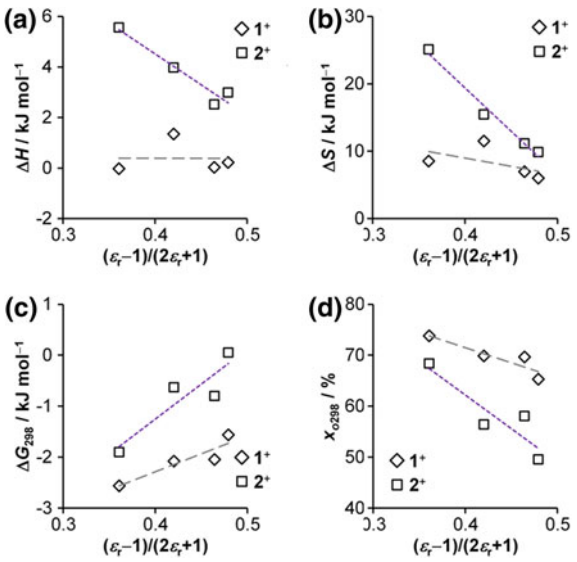

Fig. 2.25 Correlation between the Kirkwood function, $(\varepsilon_r-1)/(2\varepsilon_r + 1)$, and thermodynamic parameters, ΔH (**a**), ΔS (**b**), ΔG_{298} (**c**), and x_{o298} (**d**), of **1**·BF_4 and **2**·BF_4 in $CDCl_3$, CD_2Cl_2, acetone-d_6, and CD_3CN

representative two ion-pairing states, and omit the others. It should be noted that ion pairing between a monovalent metal complex cation and a monovalent counter anion is strengthened in $CDCl_3$, moderate in CD_2Cl_2, and weakened in more polar solvent such as acetone-d_6, reported by several groups [2–6]. On the other hand, with respect to the size of the anion, BF_4^- is significantly smaller than $B(C_6F_5)_4^-$, which is comparable with the size of the copper complex cation.

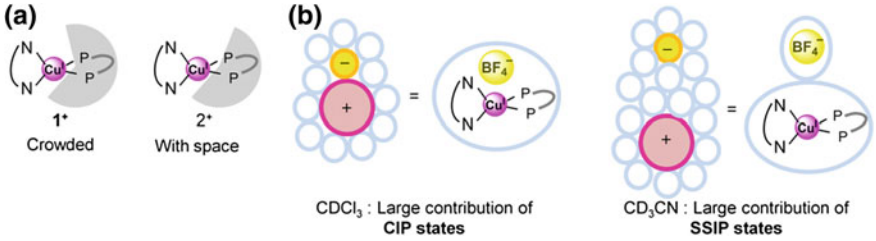

Fig. 2.26 Illustrations of the effect of ion pairing on the rotational bistability of a $[Cu(Mepypm)(diphosphine)]^+$ family. **a** Geometric features of the diphosphine moieties of $\mathbf{1}^+$ and $\mathbf{2}^+$. **b** The Cu(I) complexes in a contact ion pair (CIP) state and a solvent-separated ion pair (SSIP) state

The value of ΔH for solvated *i*-Cu^I and *o*-Cu^I is linked to intrinsic preference caused by induction effect of the methyl group, electrostatic interactions, solvation, electrostatic attraction between the electron cloud of the methyl group and the positively charged metal core of the complex, and other enthalpic factors present. The ΔS values are a reflection of their respective freedom of rotation of functional groups, along with the vibrational freedom of the ligand moieties, the solvent, and the counterion. For example, the large positive values of $\mathbf{2}\cdot BF_4$ in $CDCl_3$ indicate that the behavior of the solvated *i*-Cu^I differs significantly from the solvated *o*-Cu^I. In addition, the relatively small absolute values of both ΔH and ΔS of other conditions, $\mathbf{2}\cdot BF_4$ in polar solvent, $\mathbf{1}\cdot BF_4$ in all solvents as we tested, $\mathbf{2}\cdot B(C_6F_5)_4$ in $CDCl_3$, and $\mathbf{1}\cdot B(C_6F_5)_4$ in $CDCl_3$, indicate that the differences in the behaviors between the solvated *i*- and *o*-isomers are trivial.

The rotational equilibrium in solution is represented as a model, displayed in Fig. 2.27. Six conditions are represented: (a) $\mathbf{2}\cdot BF_4$ in $CDCl_3$, (b) $\mathbf{2}\cdot BF_4$ in CD_3CN, (c) $\mathbf{2}\cdot B(C_6F_5)_4$ in $CDCl_3$, (d) $\mathbf{1}\cdot BF_4$ in $CDCl_3$, (e) $\mathbf{1}\cdot BF_4$ CD_3CN, and (f) $\mathbf{1}\cdot B(C_6F_5)_4$ in $CDCl_3$. The equilibrium behaviors in CD_2Cl_2 and acetone-d_6 can be interpreted as a range from those in less polar $CDCl_3$ to those in more polar CD_3CN, considering their moderate thermodynamic parameters and relative permittivity. Each result has two points: (i) ΔH and ΔS, (ii) ΔG_{298} and x_{o298}.

The six conditions a–f are explained as follows. (a-i) The values of ΔH and ΔS of $\mathbf{2}\cdot BF_4$ in $CDCl_3$ are larger in magnitude and more positive than those under other conditions. In the CIP state of solvated *o*-Cu^I, there are no steric repulsion between the counterion and the methyl group (Fig. 2.27a). In contrast, the CIP state of the solvated *i*-Cu^I competes for the counterion, BF_4^-, and the methyl group on the pyrimidine unit as a result of steric repulsion. This repulsion can be correlated to destabilization of the solvated *i*-Cu^I, which corresponds to more positive values of ΔS, owing to loss of freedom in the complex cation as well as the counterion. The larger difference in solvation between *i*-Cu^I and *o*-Cu^I can cause more positive ΔH. Enhanced solvated *i*-Cu^I preference based on a combination of several enthalpic factors described above can contribute to ΔH because its movement is strongly limited by the competition. (a-ii) The negative value of

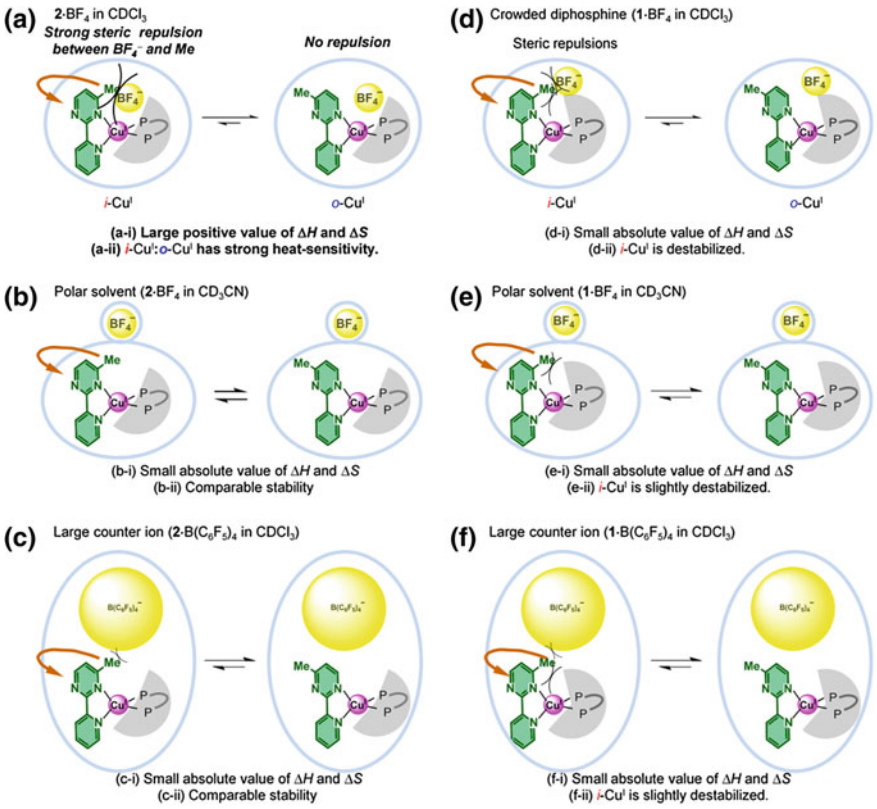

Fig. 2.27 Illustrations of the effect of ion pairing on the rotational bistability of a $[Cu(Mepypm)(diphosphine)]^+$ family. Selected chemical equilibrium between the solvated *i*- and *o*-isomers: **a** **2**·BF_4 in $CDCl_3$, **b** **2**·BF_4 in CD_3CN, **c** **2**·$B(C_6F_5)_4$ in $CDCl_3$, **d** **1**·BF_4 in $CDCl_3$, **e** **1**·BF_4 in CD_3CN, and **f** **1**·$B(C_6F_5)_4$ in $CDCl_3$

ΔG_{298} indicates that the population of the entropically-favorable solvated *o*-Cu^I, mentioned in (a-i), is larger than that of *i*-Cu^I at 298 K. At low temperature such as 233 K, where the entropic factor is less dominant, both isomers have comparable stability; absolute value of ΔG_{233} is nearly zero. The comparable stabilization effects in the viewpoint of enthalpy and entropy cause the rotational bistablity.

(b-i) The effects of solvent polarity are described in this paragraph. The ΔH and ΔS of **2**·BF_4 are positively small in polar solvents such as CD_3CN (Fig. 2.27b). The steric repulsion between the methyl group on the pyrimidine moiety and the counterion, mentioned in paragraph (a-i), is relatively small in the SSIP states of both the solvated *i*-Cu^I and *o*-Cu^I. Because difference in solvation between *i*-Cu^I and *o*-Cu^I is relatively small, the absolute values of ΔH and ΔS are also small. (b-ii) The x_{o298} values of **2**·BF_4 in CD_3CN are smaller than in $CDCl_3$ because the destabilization of the solvated *i*-Cu^I, mentioned in paragraph (a), is considerably

minimized in the SSIP state. The more positive value of ΔG_{298} in CD_3CN compared to that in $CDCl_3$ also reflects this trend.

(c-i) The effects of the counterion size are explained in this paragraph. The ΔH and ΔS of $\mathbf{2}\cdot B(C_6F_5)_4$ in $CDCl_3$ are more negative than those of $\mathbf{2}\cdot BF_4$ in $CDCl_3$ (Fig. 2.27c). Because the $B(C_6F_5)_4^-$ ion causes a small destabilization of the *i*-Cu^I in the CIP state, as described in paragraph (a), derived from its size, the small difference in solvation between two isomers contributes to small absolute values of ΔH and ΔS. (c-ii) The inhibition of the destabilization of the *i*-Cu^I also causes a decrease in x_{o298} for the $B(C_6F_5)_4^-$ ion compared with the BF_4^- ion; The more positive value of ΔG_{298} with $B(C_6F_5)_4^-$ ion compared to BF_4^- ion also reflects this trend.

(d-i) The effect of the geometry of the diphosphine ligand is described in paragraphs (d), (e), and (f). Despite the absolute values of ΔH and ΔS of $\mathbf{2}\cdot BF_4$ in $CDCl_3$ being relatively large, those of $\mathbf{1}\cdot BF_4$ in $CDCl_3$ are small since the bulkiness of the diphosphine of $\mathbf{1}^+$ reduces the steric repulsion between the methyl group of the solvated *i*-isomer and the counterion, as mentioned in (a-i) (Fig. 2.27d). The reason of nearly zero ΔH value of $\mathbf{1}^+$ can be interpreted as small difference in solvation between *i*-Cu^I and *o*-Cu^I (Fig. 2.27d). (d-ii) The value of ΔG_{298} is negative because the bulkiness of the diphosphine contributes to a destabilization of *i*-Cu^I via steric repulsion between the methyl group and the diphosphine moiety. The bulkiness is also the reason why x_{o298} of $\mathbf{1}\cdot BF_4$ in several solvents is larger than that of $\mathbf{2}\cdot BF_4$.

(e-i) The absolute values of both ΔH and ΔS of $\mathbf{1}\cdot BF_4$ in CD_3CN are small because of a combination of phenomena described in (b-i) and (d-i) (Fig. 2.27e). (e-ii) The negative ΔG stems from the steric bulk of the diphosphine as described in (d-ii). The lower x_{o298} of $\mathbf{1}\cdot BF_4$ in polar solvents compared with $\mathbf{1}\cdot BF_4$ in $CDCl_3$ was attributed to ion pairing effects, as highlighted in the above comparison of (a) and (b).

(f-i) The absolute values of both ΔH and ΔS of $\mathbf{1}\cdot B(C_6F_5)_4$ in $CDCl_3$ are small due to a combination of (c-i) and (d-i) phenomena (Fig. 2.27f). (f-ii) Since the ion pairing effects are slightly retained, the x_{o298} of $\mathbf{1}\cdot B(C_6F_5)_4$ was lower than that of $\mathbf{1}\cdot BF_4$.

The values of both ΔH and ΔS contain a contribution of the effects mentioned above as well as the following intrinsic factors. Several factors can contribute to the values. For example, the stabilization of *i*-Cu^I stemming from the electronic structure of Mepypm, which can be derived from induction effects, and thus contribute to positive ΔH values. A stabilization of *i*-Cu^I caused by an easing of the C–H interaction between the methyl group and the phenyl groups on the diphosphine, can also contribute to positive ΔH values. The entropy loss of *i*-Cu^I originates from a crowded coordination geometry, which reduces the freedom of motion of the ligand moiety, thus contributing to positive values of ΔS. These intrinsic factors also contribute to the values of x_o.

Consequently, all results related to thermodynamics can be reasonably understood based on the proposed model, suggesting that the present rotational bistability, particularly in $\mathbf{2}^+$, arises from solvated ion-pairing.

2.6.3 Notes About the Model

I note that the ^{1}H NMR signals can be the average of many kinds of conformations, such as the solvent, the counterion, and the ligands including the diphosphine moiety. The conceptual diagrams, displayed in Fig. 2.27, are representative of the real equilibrium.

Since the crystal structures of a family of [Cu(Mepypm)(diimine)]$^+$ [37–40], including a complex in Chap. 4, were very different from those of the present complexes, particularly from the viewpoint of coordination structure and location of the counterion, the ion-pairing sensitivity derived from model mentioned above is characteristic of [Cu(Mepypm)(diphosphine)]$^+$ structures.

Changes in dipole moment, hydrogen bonding interaction, and hydrophobic interactions between two states are often attributed to solvent-sensitivity not only in traditional conformational equilibrium such as axial/equatorial forms in cyclohexane derivatives[1] but also in chemistry for promising nanomaterials such as molecular machines based on supramolecules [27–36]. Because the complex cations of the two isomers are similar with respect to coordination structure, the polarity differences between *i*-Cu^I and *o*-Cu^I are expected to be small. On the other hand, the absolute value of the dipole moment of the solvated copper(I) compounds is expected to be proportional to the distance between the copper atom and the counterion center (Cu-X). Therefore, the polarity of the *i*-isomer in the CIP state is expected to be larger than that of the *o*-isomer, considering that the Cu-X distance is determined by steric repulsion. This is an additional effect caused by ion pairing as described in Fig. 2.27. The difference in polarity between the two isomers in the CIP state can contribute to the preference of the *i*-Cu^I for more polar solvent. This rationale is incomplete for three reasons: (1) the population of the CIP state in polar solvent is small, (2) the difference of the Cu-X distance between *i*- and *o*-isomers in the SSIP state is small, and (3) the large ΔH and ΔS of **2**·BF_4 in $CDCl_3$ cannot be appropriately explained by this reasoning.

If a solvent molecule, such as CD_3CN which has high affinity to copper(I) state, coordinates to the copper(I) center of present complexes, steric repulsion between the methyl group and the solvent molecule would cause a decrease of *i*-Cu^I ratio in CD_3CN compared with $CDCl_3$. This assumption can be totally denied, because of both experimental results and electronic configuration; The copper(I) center has already the coordination number of 4, so that it cannot accommodate any additional ligand.

I assume that the volume where BF_4^- ion is present, displayed in Fig. 2.27a, can be occupied by a $CDCl_3$ molecule instead of the counterion, which can destabilize *i*-Cu^I via steric repulsion between the methyl group and the solvent molecule. Since this assumption does not explain the decrease in the *o*-Cu^I molar ratio when a larger counterion is used, the effects of the size of the solvent molecule are small.

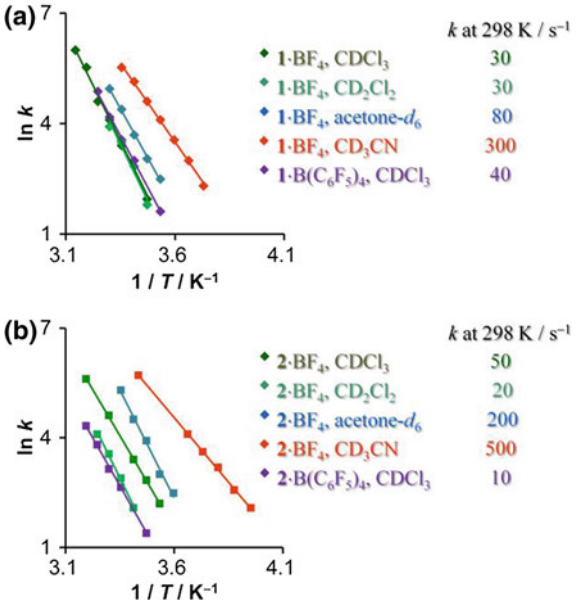

Fig. 2.28 The Arrhenius plots and the rate constant at 298 K for the *i*-Cu^I → *o*-Cu^I interconversion of $\mathbf{1}^+$ (**a**) and $\mathbf{2}^+$ (**b**) under a variety of conditions

2.7 Rate for the Isomerization in a Solution State

The rate constants for the *i*-Cu^I → *o*-Cu^I isomerization, *k*, at variable temperature were estimated from Arrhenius plots based on simulation of the broadened ^1H NMR spectra (Figs. 2.4, 2.5, 2.6, 2.7, 2.8, 2.9, 2.10, 2.11, 2.12, 2.13 and 2.28). The values of *k* at 298 K, k_{298}, which are the parameters most representative of the solvent- and counterion-sensitive kinetics, are also summarized in Fig. 2.28. Other parameters are tabulated in Table 2.4.

The kinetics analysis supports the validity of the thermodynamic analysis. The magnitude of the *k* values at the given temperature, where ^1H NMR spectra for the thermodynamic analysis were conducted, falls within a range from 10^{-2} to 10^0 s^{-1} (Fig. 2.29). Qualitatively, the values indicate that the system reaches equilibrium within 10^2 s. For the ^1H NMR spectra conducted with ca. 10^3 s intervals, the signal integrations reflect the ratio of *i*-Cu^I and *o*-Cu^I in equilibrium. Signal broadening is observed when *k* exceeds ca. 10^1 s^{-1}. The ^1H NMR spectra at high temperature are not employed for the thermodynamic analysis.

The much larger k_{298} values obtained in coordinating solvent such as CD_3CN, compared with non-coordinating solvent such as $CDCl_3$, were observed not only for $\mathbf{1}\cdot BF_4$ (30 s^{-1} in $CDCl_3$, 30 s^{-1} in CD_2Cl_2, 80 s^{-1} in acetone-d_6, and 300 s^{-1} in CD_3CN) but also for $\mathbf{2}\cdot BF_4$ (50 s^{-1} in $CDCl_3$, 20 s^{-1} in CD_2Cl_2, 200 s^{-1} in acetone-d_6, and 500 s^{-1} in CD_3CN). The promotion of the isomerization by high affinity of coordination of a solvent molecule to copper(I) ion, which assists the dissociation of the pyrimidine nitrogen atoms from the copper center, was

Table 2.4 Selected kinetic parameters for the rotational equilibrium of a family of $[Cu(Mepypm)(diphosphine)]^+$ in several conditions

	Solvent	E_a^a	log(A)[b]	k_{298}^c
1·BF_4	$CDCl_3$	100	19	30
1·BF_4	CD_2Cl_2	100	19	30
1·BF_4	Acetone-d_6	70	14	80
1·BF_4	CD_3CN	70	15	300
1·$B(C_6F_5)_4$	$CDCl_3$	90	18	40
2·BF_4	$CDCl_3$	80	16	50
2·BF_4	CD_2Cl_2	100	19	20
2·BF_4	Acetone-d_6	100	19	200
2·BF_4	CD_3CN	60	13	500
2·$B(C_6F_5)_4$	$CDCl_3$	90	16	10

[a] Activation energy for i-Cu^I → o-Cu^I rotation/kJ mol^{-1}
[b] Logarithm of frequency factor for i-Cu^I → o-Cu^I rotation
[c] Rate constant for i-Cu^I → o-Cu^I rotation at 298 K/s^{-1}

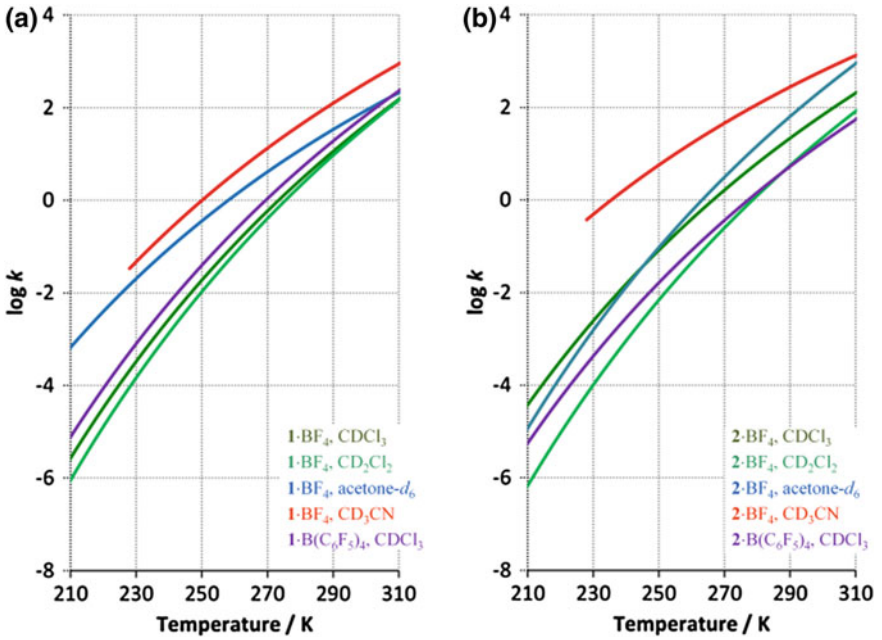

Fig. 2.29 The rate constants, k, for the i-Cu^I → o-Cu^I rotational isomerization of $\mathbf{1}^+$ (**a**) and $\mathbf{2}^+$ (**b**) in several conditions as a function of temperature, estimated from the Arrhenius plots. Regression curves of the Arrhenius plots are indicated by lines

generally found throughout the $[Cu(Mepypm)(diphosphine)]^+$ family. The value of k_{298} in a $CDCl_3$ solution of **2**·$B(C_6F_5)_4$ is 10 s^{-1}, which is smaller than that of **2**·BF_4. The decrease of k_{298} resulting from the use of a bulky counter anion

suggests that the weak coordination ability of BF_4^- can slightly assist in Cu–N bond dissociation. This behavior seems to be consistent with the model describing the BF_4^- ion approach in the CIP state. **1**·$B(C_6F_5)_4$ in $CDCl_3$ ($k_{298} = 40\ s^{-1}$) is very similar to **1**·BF_4 in $CDCl_3$. The resemblance also seems to relate to the model provided in Fig. 2.27. The rate constant associated with **1**·BF_4 in CD_2Cl_2 was comparable with that of **1**·BF_4 in $CDCl_3$, because the coordination abilities of CD_2Cl_2 and $CDCl_3$ are similarly weak. In contrast, a small decrease of k_{298} in CD_2Cl_2 compared with $CDCl_3$ was observed for **2**·BF_4. The solvent sensitivity seems to be consistent with the model illustrating that the ion-pairing sensitivity of $\mathbf{2}^+$ is larger than that of $\mathbf{1}^+$, shown in Fig. 2.27. This result can be interpreted as a promotion of rotation by enhancement of coordination ability of BF_4^- ion in CIP state. These CIP effects can contribute to the kinetics of rotation, but this effect seems to be smaller than that of the solvent coordination.

A tricoordinated intermediate, where the nitrogen atom on the pyrimidine unit is dissociated from the copper center, is one of the possible intermediates. One of the another possible intermediates is a tetracoordinated intermediate, which is coordinated by one nitrogen atom on pyridine unit, two phosphine atoms, and one solvent molecule, because the rate of rotation in the coordinative solvent such as CD_3CN, which has high coordination affinity to copper center, is found to be much faster than that in the non-coordinative solvent such as $CDCl_3$.

On the other hand, viscosity of $CHCl_3$, CH_2Cl_2, acetone, and CH_3CN is 0.5357, 0.449, 0.3029, and 0.341 cP, respectively. Rate constants for *i*-Cu^I → *o*-Cu^I at 298 K (k_{298}) in $CDCl_3$, CD_2Cl_2, acetone-d_6, and CD_3CN are 50, 20, 200, and 500 s^{-1}, respectively (Table 2.4). Additionally, viscosity of CH_3OH is 0.5513, and k_{298} in CD_3OD is 150, estimated from preliminary experiment. Contribution of viscosity seems to be much smaller than that of coordination affinity to copper(I), because rate constants in $CDCl_3$ and CD_3OD, which have similar values of viscosity, are significantly different.

The solvent sensitivity trends, mentioned above, are basically observed over the full temperature range tested (see Arrhenius plots in Fig. 2.28). The *k* value varied from 10^{-6} (frozen motion) to $10^3\ s^{-1}$ over the temperature and solvent ranges considered (Fig. 2.29).

2.8 Conclusion

A series of simple copper(I) complexes bearing a Mepypm and a diphosphine ligand, $[Cu(Mepypm)(diphosphine)]^+$, namely, **1**·$BF_4$, **1**·$B(C_6F_5)_4$, **2**·$BF_4$, and **2**·$B(C_6F_5)_4$ was synthesized. Two rotational isomers, *i*-Cu^I and *o*-Cu^I, coexist and interconvert in solution via intramolecular ligating atom exchange of the pyrimidine ring in all complexes as I tested. The interconversion between *i*-Cu^I and *o*-Cu^I is generally an intramolecular process, as confirmed by ^1H NMR analysis of a mixed solution of **1**·BF_4 and $[Cu(bpy)(DPEphos)]BF_4$. Both the enthalpy and entropy values for *i*-Cu^I → *o*-Cu^I rotation of **2**·BF_4 in $CDCl_3$ ($\Delta H = 6\ kJ\ mol^{-1}$,

$\Delta S = 25$ J K^{-1} mol^{-1}) were larger than that tested under other conditions. The absolute values of both ΔH and ΔS significantly decreased in more polar solvents, such as CD_2Cl_2, acetone-d_6, and CD_3CN. The reduced contact of the couteranion to the complex cation in polar solvent contributes to the relative stability of the isomers: The values of $x_{o298} = [o\text{-}Cu^I]/([i\text{-}Cu^I] + [o\text{-}Cu^I])$ are 68 % (**2**·BF_4 in $CDCl_3$), 50 % (**2**·BF_4 in CD_3CN), 74 % (**1**·BF_4 in $CDCl_3$), and 65 % (**1**·BF_4 in CD_3CN). This speculation based on solvated ion pairing was further confirmed by considering the rotation behavior with a bulky counterion, $B(C_6F_5)_4^-$. Crystal structures of o-Cu^I (**1**·BF_4, **1**·$B(C_6F_5)_4$ and **2**·BF_4) and i-Cu^I (**2**·$B(C_6F_5)_4$) are helpful to construct the model. The findings described herein are valuable for the design of photo- and/or redox-active molecular mechanical units that can be readily functionalized via weak electrostatic interactions. The rate constants for interconversion between i-Cu^I and o-Cu^I varied from 10^{-6} (frozen motion) to 10^3 s^{-1} over the temperature and solvent ranges considered.

The slow rate of rotation plays a key role for functions of our rotational system. For example, in the previous report, we have developed switching systems by trapping metastable states. This strategy enables me to construct PET-driven rotation system, described in Chap. 4. For another example, I have demonstrated dual emission caused by ring rotational isomerization, described in Chap. 3. Common organic solution state is found to be suitable for these desired functions.

References

1. Reichardt C (2003) Solvents and solvent effects in organic chemistry, 3rd edn. Wiley-VCH, Weinheim
2. Macchioni A (2005) Chem Rev 105:2039–2073
3. Moreno A, Pregosin PS, Veiros LF, Albinati A, Rizzato S (2009) Chem Eur J 15:6848–6862
4. Kumar PGA, Pregosin PS, Goicoechea JM, Whittlesey MK (2003) Organometallics 22:2956–2960
5. Pregosin PS, Kumar PGA, Fernández I (2005) Chem Rev 105:2977–2998
6. Martinez-Viviente E, Pregosin PS (2003) Inorg Chem 42:2209–2214
7. Lacour J, Moraleda D (2009) Chem Commun 7073–7089
8. Hebbe-Viton V, Desvergnes V, Jodry JJ, Dietrich-Buchecker C, Sauvage J-P, Lacour J (2006) Dalton Trans 2058–2065
9. Desvergnes-Breuil V, Hebbe V, Dietrich-Buchecker C, Sauvage J-P, Lacour J (2003) Inorg Chem 42:255–257
10. Hutin M, Nitschke JR (2006) Chem Commun 1724–1726
11. Merrill CL, Wilson LJ, Thamann TJ, Loehr TM, Ferris NS, Woodruff WH (1984) J Chem Soc Dalton Trans 2207–2221
12. Liang H-C, Kim E, Incarvito CD, Rheingold AL, Karlin KD (2002) Inorg Chem 41:2209–2212
13. Letko CS, Rauchfuss TB, Zhou X, Gray DL (2012) Inorg Chem 51:4511–4520
14. Lee Y, Lee D-H, Park GY, Lucas HR, Narducci Sarjeant AA, Kieber-Emmons MT, Vance MA, Milligan AE, Solomon EI, Karlin KD (2010) Inorg Chem 49:8873–8885
15. Medwid JB, Paul R, Baker JS, Brockman JA, Du MT, Hallett WA, Hanifin JW, Hardy RA, Tarrant ME, Torley LW, Wrenn S (1990) J Med Chem 33:1230–1241
16. Lafferty JJ, Case FH (1967) J Org Chem 32:1591–1596

17. Kuang SM, Cuttell DG, McMillin DR, Fanwick PE, Walton RA (2002) Inorg Chem 41:3313–3322
18. Saito K, Arai T, Takahashi N, Tsukuda T, Tsubomura T (2006) Dalton Trans 4444–4448
19. Yang L, Feng JK, Ren AM, Zhang M, Ma YG, Liu XD (2005) Eur J Inorg Chem 1867–1879
20. Altomare A, Cascarano G, Giacovazzo C, Guagliardi A, Burla MC, Polidori G, Camalli M (1994) J Appl Cryst 27:435
21. Sheldrick GM (2008) Acta Cryst A64:112–122
22. Farrugia LJ (1999) J Appl Cryst 32:837–838
23. Fulmer GR, Miller AJM, Sherden NH, Gottlieb HE, Nudelman A, Stoltz BM, Bercaw JE, Goldberg KI (2010) Organometallics 29:2176–2179
24. Atkins P, De Paula J (2006) Physical chemistry, 8th edn. W. H. Freeman, New York
25. Bain AD (2003) Prog Nucl Magn Reson Spectrosc 43:63–103
26. Sandström J (1982) Dynamic NMR spectroscopy. Academic Press, London
27. Hiraoka S, Okuno E, Tanaka T, Shiro M, Shionoya M (2008) J Am Chem Soc 130:9089–9098
28. Hiraoka S, Hisanaga Y, Shiro M, Shionoya M (2010) Angew Chem Int Ed 49:1669–1673
29. Kilbas B, Mirtschin S, Scopellitia R, Severin K (2012) Chem Sci 3:701–704
30. Leigh DA, Morales MAF, Pérez EM, Wong JKY, Saiz CG, Slawin AMZ, Carmichael AJ, Haddleton DM, Brouwer AM, Buma WJ, Wurpel GWH, León S, Zerbetto F (2005) Angew Chem Int Ed 44:3062–3067
31. Gong C, Gibson HW (1997) Angew Chem Int Ed Engl 36:2331–2333
32. Wilmes GM, France MB, Lynch SR, Waymouth RM (2004) Organometallics 23:2405–2411
33. Tafazzoli M, Ziyaei-Halimjani A, Ghiasi M, Fattahi M, Saidi MR (2008) J Mol Struct 886:24–31
34. Gennari M, Lanfranchi M, Cammi R, Pellinghelli MA, Marchiò L (2007) Inorg Chem 46:10143–10152
35. Nakafuji S, Kobayashi J, Kawashima T, Schmidt MW (2005) Inorg Chem 44:6500–6502
36. Blom R, Swang O (2002) Eur J Inorg Chem 411–415
37. Nomoto K, Kume S, Nishihara H (2009) J Am Chem Soc 131:3830–3831
38. Kume S, Nomoto K, Kusamoto T, Nishihara H (2009) J Am Chem Soc 131:14198–14199
39. Kume S, Nishihara H (2011) Chem Commun 47:415–417
40. Kume S, Nishihara H (2011) Dalton Trans 40:2299–2305

Chapter 3
Dual Emission Caused by Ring Rotational Isomerization of a Copper(I) Complex

Abstract Photophysics of metal complexes is valid for photofunctional devices. Transient emission spectra measurement is a powerful way to find difference in photoprocesses between two rotational isomers which interconvert and coexist in the solution. I developed a molecular system which exhibited heat-sensitive dual luminescence behavior caused by the pyrimidine ring rotational isomerization in copper(I) complexes. This finding is valuable for the novel way to handle the photoprocesses of transition metal complexes.

Keywords Luminescence · Photophysics · Copper(I) complex · Molecular rotation · Equilibrium

3.1 Introduction

3.1.1 The Aim of this Study

Our group has developed that the pyrimidine ring rotational isomeric system, described in Sect. 1.4, whose function is based on a collaboration of electrochemistry and rotational bistability. The aim of this study is development of a system which exhibits functions based on collaboration of photophysics with rotation dynamics.

As I described in Sect. 1.1.1, the photoprocesses of transition metal complexes are of interest for their potential use in promising devices. Recently, photofunctional molecules have been synthesized using simple metal complexes that exhibit dual phosphorescence as a result of the presence of two independent excited states [1–3]. Unfortunately, methods for selectively preparing one of the two states have thus far been limited. The state selection requires a system characterized by well-defined bistability via a reversible chemical process. Photofunctionalization of a pyrimidine ring rotational system enables me to develop the system mentioned above (Fig. 3.1).

M. Nishikawa, *Photofunctionalization of Molecular Switch Based on Pyrimidine Ring Rotation in Copper Complexes*, Springer Theses,
DOI: 10.1007/978-4-431-54625-2_3, © Springer Japan 2014

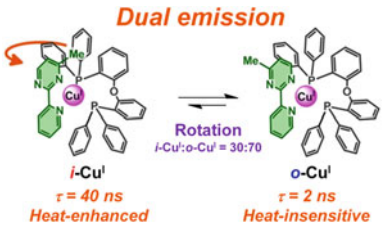

Fig. 3.1 Conceptual diagram showing dual emission caused by pyrimidine ring rotational isomerization of **1**·BF_4

3.1.2 Molecular Design

The investigation mentioned above revealed that the complexes, **1**·BF_4 and **2**·BF_4, exhibited rotational bistability in acetone (Chap. 2), which is suitable for development of desired functions. Whereas **2**·BF_4 showed negligible luminescence in solution (Sect. 3.7), **1**·BF_4 exhibited luminescence in acetone, because the copper(I) complexes coordinated by diimine and DPEphos are known to exhibit a strong emission from a long-lived CT excited state [4, 5]. Therefore, I examined the emission properties of **1**·BF_4 in solution. Since two rotational isomers are expected to be different in the emission properties due to well-established relationship between coordination structure and photophysics in copper(I) complexes (Sect. 1.2) [6, 7], dual luminescence behaviors can be expected.

3.1.3 Contents of this Chapter

I described dual emission behaviors in Sects. 3.3–3.7 and other properties related to $\mathbf{1}^+$ and $\mathbf{2}^+$ in Sect. 3.8. **1**·BF_4 exhibited mechanical bistability based on the rotational motion of the pyrimidine ring, leading to dual luminescence behavior in a solution state. ^{1}H NMR spectra in acetone-d_6 at several temperatures revealed that the two rotational isomers, *i*-Cu^I and *o*-Cu^I, interconverted in solution, and the motion was frozen below 200 K. The complex showed characteristic CT absorption and emission bands in solution. Emission lifetime measurements demonstrated that the emission could be deconvoluted into two components. The fast and slow components were assigned to o-Cu^I and *i*-Cu^I, the excited states of which were characterized by different structural relaxation process and/or additional solvent coordination properties. The emission properties of the two isomers differed not only in lifetime and wavelength but also in heat sensitivity. This study would be useful not only for a way to handle photophysics of metal complexes but also construction of a single molecular system for light-energy processing.

3.2 Experimental Section

Materials, instruments, and analysis for rotational dynamics are same as those described in Chap. 2.

UV-vis absorption spectra and emission spectra UV-vis absorption spectra were recorded with a JASCO V-570 spectrometer a Hewlett Packard 8453 spectrometer. Steady-state uncorrected emission spectra at several temperatures (Figs. 3.5 and 3.6) were recorded with a HITACHI F-4500 spectrometer equipped with UNISOKU USP-201-A cryostat. Steady-state corrected emission spectra in the solid state (Fig. 3.17) were recorded with the same spectrometer. Solid-state luminescence images were measured under blue light excitation using an Olympus BX51 fluorescence microscope. The luminescence quantum yield was estimated from tris(2,2′-bipyridine)ruthenium(II) hexafluorophosphate in acetonitrile under air (1.8 %) as a standard. Electrochemical measurements were acquired with an ALS 750A electrochemical analyzer. The working electrode was a 0.3 mm-o.d. glassy carbon electrode; a platinum wire served as the auxiliary electrode, and the reference electrode was an Ag^{+}/Ag electrode (a silver wire immersed in 0.1 M Bu_4NClO_4/0.01 M $AgClO_4/CH_3CN$). The solutions for electrochemical measurements were deoxygenated with argon prior to measurement.

For time-resolved fluorescence spectrum measurement, the output of a dye laser (FL3002, Lambda Physik) pumped by a XeCl excimer laser (LEXTRA 50, Lambda Physik) was used as a pump beam. The pump beam was focused onto the sample solution by a convex lens ($f = 150$). The fluorescence emitted perpendicularly to the pump beam from the sample was collected and collimated by another convex lens, and then focused and introduced to a streak camera (C4334, HAMAMATSU) equipped with a monochrometer (C5905, HAMAMATSU). The measured instrument response function had a full-width at half-maximum of ca. 7 ns. The emission transients were fit to a sum of two exponentials convoluted with the measured instrument response function. The experimental emission decay profiles except Fig. 3.9c were integrated at 630 ± 10 nm. The rising points in the decay profiles were standardized to 0 ns. The time-resolved spectra for the faster and slower components were obtained by integration of the data in 0 ns after excitation (15 ± 5 ns) and in 85 ns after excitation (100 ± 50 ns), respectively.

3.3 Rotational equilibrium

Synthesis and characterization of **1**·BF_4 are described in Chap. 2. I briefly summarize the rotational equilibrium of **1**·BF_4 in acetone-d_6; for detail, see Chap. 2.

The ^{1}H NMR peaks of **1**·BF_4 in acetone-d_6 at 243 K could be clearly assigned to either *i*-Cu^I or *o*-Cu^I without evidence for other coordination species (Fig. 3.2). The chemical shifts of these signals were affected by the shielding effects of the copper and the phenyl group of DPEphos moiety, and the major and minor peaks

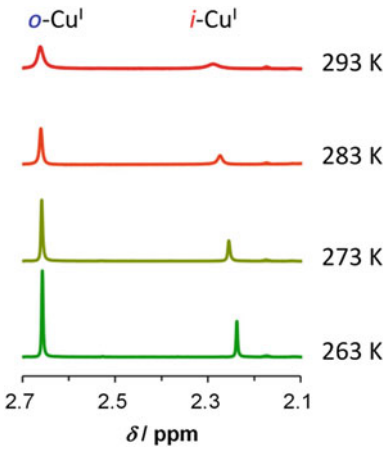

Fig. 3.2 ^{1}H NMR spectra of **1**·BF_4 in acetone-d_6 at several temperatures in the methyl group region

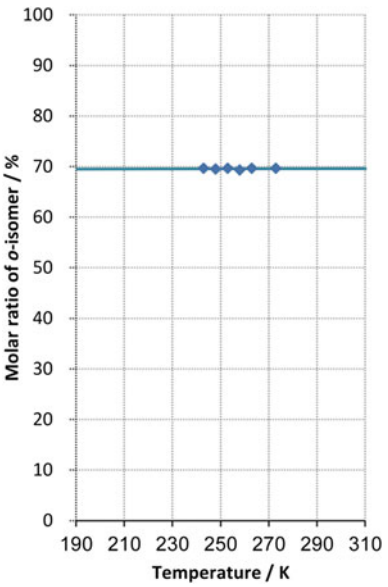

Fig. 3.3 The ratios of *o*-Cu^{I} {[*o*-Cu^{I}]/([*i*-Cu^{I}] + [*o*-Cu^{I}])} of **1**·BF_4 in acetone-d_6 at several temperatures. The experimental values are shown as the *dots*, and the values calculated from the regression of van't Hoff plot are drawn in line

were assigned, respectively, to *o*-Cu^{I} and *i*-Cu^{I}. These signals broadened upon heating, indicating that two rotational isomers, *i*-Cu^{I} and *o*-Cu^{I}, interconverted in a solution state, which occurred on the time scale of the ^{1}H NMR experiment (Fig. 3.2). The molar ratio of *i*-Cu^{I} and *o*-Cu^{I} in acetone remained 30:70 over the temperature range from 203 to 293 K (Fig. 3.3). The rate of interconversion between *i*-Cu^{I} and *o*-Cu^{I} varied from 10^{-4} to 10^{3} s^{-1} over the temperature range above (Fig. 3.4). I note that the rate of interconversion between *o*-Cu^{I} and *i*-Cu^{I} is negligibly slow compared to the timescale of luminescence decay (2 and 40 ns), described in Sects. 3.5, 3.6 and 3.7.

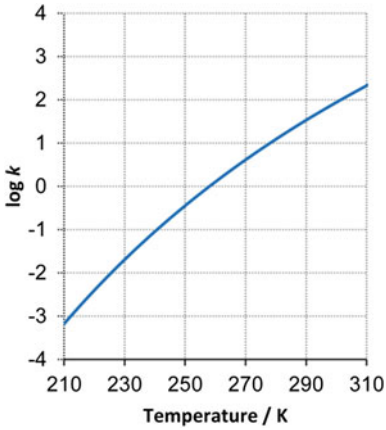

Fig. 3.4 The rate constants, k, for the i-$Cu^I \rightarrow o$-Cu^I rotational isomerization of $\mathbf{1}\cdot BF_4$ in acetone-d_6 as a function of temperature, estimated from the Arrhenius plots. Regression curves of the Arrhenius plots are indicated by lines

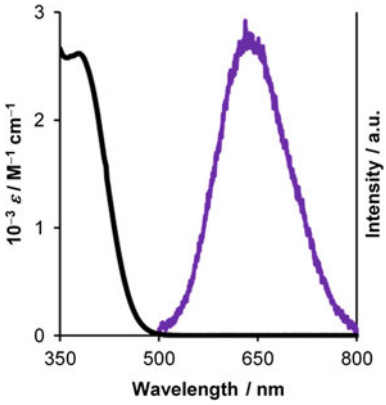

Fig. 3.5 UV-vis absorption spectrum (*black line*) and the steady-state emission spectra using 400 nm excitation (*purple line*) of $\mathbf{1}\cdot BF_4$ in acetone at room temperature

3.4 Absorption Spectra and Steady-State Emission Spectra

The UV–vis absorption spectrum of $\mathbf{1}\cdot BF_4$ in acetone showed the characteristic CT absorption bond ($\lambda_{abs} = 378$ nm, $\varepsilon = 2.7 \times 10^3$ M^{-1} cm^{-1}) of the [Cu(diimine)(diphosphine)]$^+$ family (Fig. 3.5). The absence of an absorption around 450 nm and the independence of the absorption profile on the concentration of $\mathbf{1}\cdot BF_4$ suggested that the formation of other species, such as $[Cu(Mepypm)_2]^+$, was negligible [4, 5]. The steady-state emission spectrum of $\mathbf{1}\cdot BF_4$ in acetone (Fig. 3.5) exhibited emission at $\lambda_{em} = 635$ nm from the CT state. These results indicate that the wavelengths of maximum absorption and the emission energies of the i-Cu^I and o-Cu^I were comparable. Figure 3.6 shows the steady-state emission spectra of $\mathbf{1}\cdot BF_4$ in acetone from 193 to 293 K. An increase in the emission intensity and a blue-shift with heating were observed; the details are discussed in the later sections.

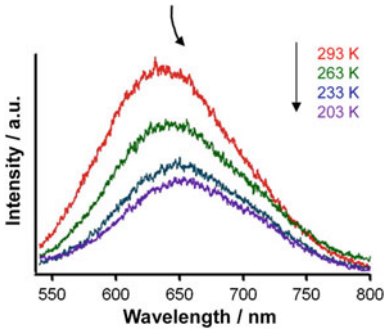

Fig. 3.6 Steady-state emission spectra using 400 nm excitation of **1**·BF_4 in acetone at 293 K (*red*), 263 K (*green*), 233 K (*blue*), and 203 K (*purple*)

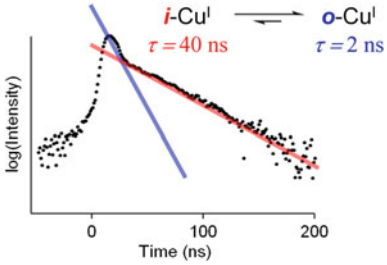

Fig. 3.7 Experimental 630 nm emission decay of **1**·BF_4 in acetone at room temperature excited at 425 nm

3.5 Time-Resolved Emission Spectra

Emission lifetime measurements of **1**·BF_4 in acetone at room temperature revealed that the decay curve could be deconvoluted into two components (Fig. 3.7). The [Cu(diimine)(diphosphine)]$^+$ family in a fluid solution state is known to show a single decay [4–7]. Therefore, the two components could be reasonably assigned to the *i*- and *o*-isomers. The faster (τ = 2 ns) and the slower (τ = 40 ns) components were attributed to emission from two rotational isomers, *o*-Cu^I and *i*-Cu^I, respectively (Fig. 3.7), because introduction of a bulky substituent into the coordination sphere is known to elongate the lifetime of the excited state of copper(I) complexes by inhibiting structural relaxation and/or preventing additional solvent coordination (Sect. 1.2) [4–7]; details are described in Sect. 3.7. This assignment was further supported by the similarities between the emission lifetimes of the *o*-Cu^I and [Cu(bpy)(DPEphos)]$^+$ (bpy = 2,2′-bipyridine), which does not contain bulky groups near the metal center (Fig. 3.8). The emission spectra of two isomers were deconvoluted using time-dependent spectral measurements. The faster component was slightly red-shifted relative to the slower component, implying that the long-lived excited state of *i*-Cu^I has the higher-energy (Fig. 3.9a). The energy difference was also confirmed from the fact that the differential spectrum, obtained by subtracting the faster component from the slower one, displays the positive values from 500 to 600 nm and the negative values from 650 to 750 nm (Fig. 3.9b). Additionally, the relative intensity of the slower component in 580 nm

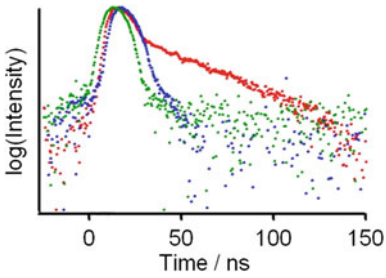

Fig. 3.8 Experimental 630 nm emission decay of **1**·BF_4 (*red dots*) and $[Cu(bpy)(DPEphos)]^+$ (*blue dots*) in acetone at room temperature. The green dots indicate instrumental response function

emission decay profile (Fig. 3.9c green dots) is slightly larger than that in 730 nm one (Fig. 3.9c red dots), supporting that luminescence maximum wavelength of *i*-Cu^I is blue-shifted from that of *o*-Cu^I.

3.6 Temperature Dependence of Time-Resolved Emission Spectra

The differences between emission behaviors of these isomers were clearly reflected in the heat sensitivity. The emission decay profile showed that the relative intensity of the slower component decreased upon cooling and became almost negligible at 203 K (Fig. 3.10). The lifetimes of the two components were almost temperature-independent, as demonstrated by the best fits of the decay profiles at each temperature (203–293 K) (Fig. 3.11). The deconvoluted emission spectra of the slower component, where contribution of emission from *i*-Cu^I is large, were blue-shifted and showed an increase in the emission intensity upon heating (Fig. 3.12a). The emission spectra of the faster component, where contribution of emission from *o*-Cu^I is large, were relatively insensitive to temperature (Fig. 3.12b). In other words, steady-state emission at low temperature and room temperature can be interpreted as emission mainly from *o*-Cu^I and that from two isomers (*i*-Cu^I and *o*-Cu^I), respectively.

3.7 Energy Diagram

I interpret these differences by the Jablonski diagram (Fig. 3.13), considering the well-established photoprocesses of copper(I) complexes (Sect. 1.2) [4–7]. Physical parameters, k_r, k_{nr}, and k_q indicate radiative, nonradiative, and solvent quenching rate constants, respectively. Energy difference between ground (GS) and Franck–Condon (FC) states in *i*-Cu^I is similar to that in *o*-Cu^I, considering small difference in absorption between two isomers. Inhibition of structural rearrangement by crowded coordination structure contributes to the larger energy difference of *i*-Cu^I

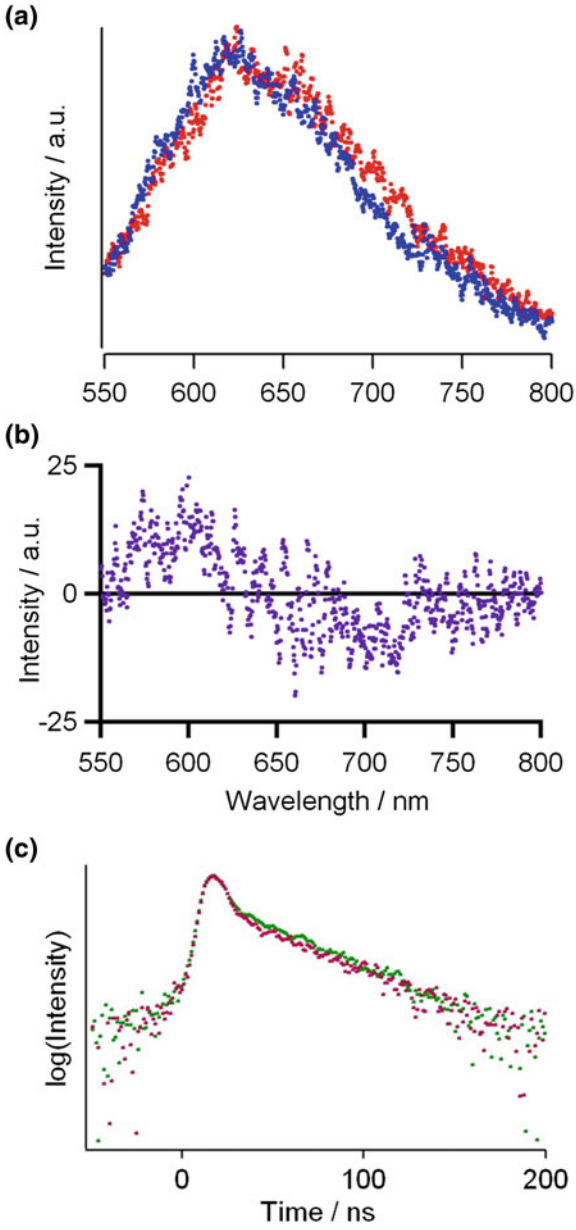

Fig. 3.9 Time-resolved emission measurement of **1**·BF_4 in acetone at room temperature. **a** Time-resolved emission spectra for the slower component $\tau = 40$ ns (*red*) and for the faster component $\tau = 2$ ns (*blue*). **b** The differential spectrum obtained by subtracting the faster component from the slower one. **c** Experimental emission decay at 580 ± 10 nm (*green dots*) and 730 ± 10 nm (*red dots*)

between GS and singlet charge transfer (^{1}CT) excited states compared to that of *o*-Cu^I. Therefore, k_{nr} in ^{1}CT of *i*-Cu^I is smaller than that of *o*-Cu^I due to energy gap law, leading to longer lifetime and higher energy emission of *i*-Cu^I compared to those of *o*-Cu^I. Inhibition of solvent coordination quenching also contributes to

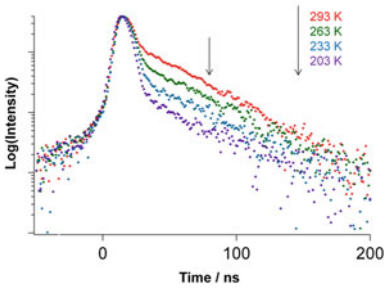

Fig. 3.10 Experimental 630 nm emission decay of **1**·BF_4 in acetone at 293 K (*red*), 263 K (*green*), 233 K (*blue*), and 203 K (*purple*) excited at 425 nm

longer lifetime emission of *i*-Cu^I, because the additional solvent coordination, which affords nonemissive 5-coordinated photoexcited species with a small energy gap, can be effectively prevented by the crowded coordinated structure. On the other hand, heat-enhanced emission of *i*-Cu^I can be explained by thermal activation from nonemissive triplet charge transfer (^{3}CT) into emissive ^{1}CT states [4, 5, 8, 9].

Because the luminescence of a family of the copper complexes bearing diimine around room temperature is assigned as delayed derived from small energy difference between ^{1}CT and ^{3}CT (ΔE), those of both *i*-Cu^I and *o*-Cu^I are also same photoprocesses. Smaller temperature dependence of emission of *o*-Cu^I compared to *i*-Cu^I can be interpreted as the contribution of one or both of two factors as follows. (1) The value of ΔE of *o*-Cu^I is smaller than that of *i*-Cu^I; (2) The thermally activated quenching of the photoexcited state of *o*-Cu^I, such as solvent coordination quenching, is more significant than that of *i*-Cu^I, considering the difference in coordination sphere between two isomers. I explain the details of the factor (1). The emission quantum yield of the delayed fluorescence is proportional to the rate of delayed fluorescence, k, which obey Arrhenius plot, $k = A\exp(E/RT)$ [9], where E indicates activation energy, T indicates absolute temperature, and R indicates gas constant. The value of ΔE is almost same as E because there is no activation required beyond reaching the energy of singlet state. Therefore, small value of ΔE reflects the small temperature dependence of the emission. The inhibition of the structural rearrangement in the crowded coordination sphere in bis(diimine)copper(I) complexes is known to reduce the value of ΔE.

3.8 Other Physical Properties

In our previous systems, $[Cu(Mepypm)(L_{anth})]^+$ and their derivatives were found to exhibit reversible copper(II/I) redox activities that were synchronized with rotational isomerization (Sect. 1.5). Cyclic voltammograms of **1**·BF_4 as well as **2**·BF_4 in 0.1 M Bu_4NBF_4-CH_2Cl_2 show irreversible oxidation waves at approximately 0.7 V versus Ag^+/Ag (1.0 V vs. $DMFc^+$/DMFc, DMFc = decamethylferrocene) (Fig. 3.14a). This irreversibility seems to be caused by an instability of the oxidized

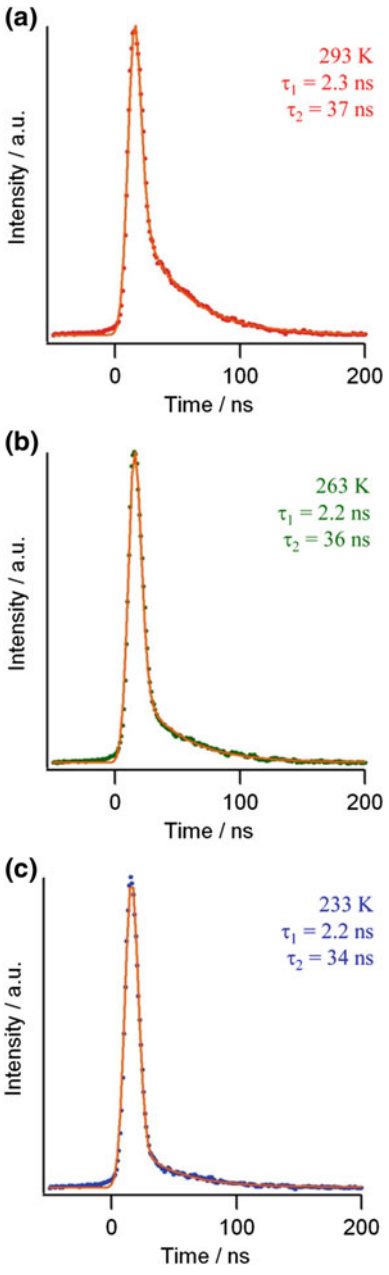

Fig. 3.11 Experimental (*dots*) and simulated (*orange line*) 630 nm emission decay of **1**·BF_4 in acetone at 293 K (**a**), 263 K (**b**), and 233 K (**c**) excited at 425 nm

[Cu(Mepypm)(diphosphine)]$^+$, which can undergo rapid adverse chemical reactions. Redox irreversibility is also observed in some [Cu(diimine)(diphosphine)]$^+$ complexes [10]. The redox potential in a solution comprising of **2**·$B(C_6F_5)_4$ in 0.1 M

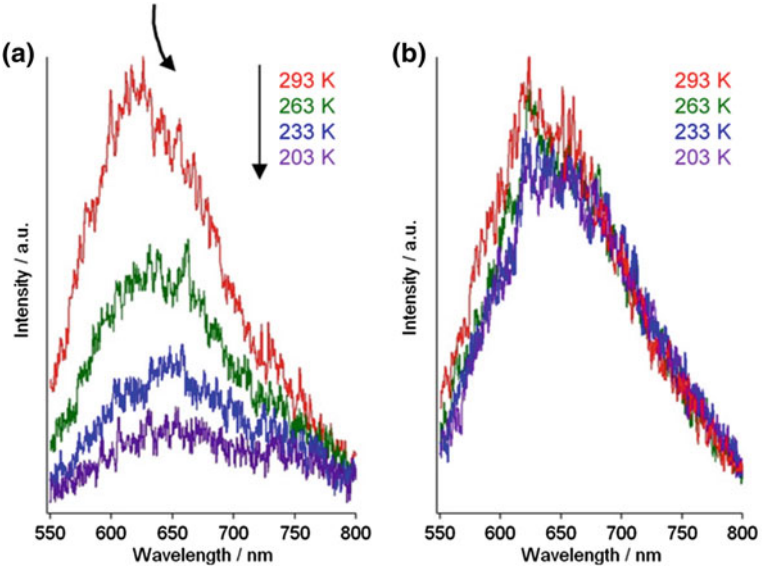

Fig. 3.12 Time-resolved emission spectra of **1**·BF_4 in acetone at several temperatures for the slower ($\tau = 40$ ns) component (**a**) and the faster ($\tau = 2$ ns) component (**b**)

$Bu_4NB(C_6F_5)_4$–CH_2Cl_2 is more positive than that of **2**·BF_4 in 0.1 M Bu_4NBF_4–CH_2Cl_2, and the reversibility of the redox wave in the solution with of $B(C_6F_5)_4^-$ (Fig. 3.14b) is better than that with BF_4^- (Fig. 3.14a). The stabilization of oxidized form by non-coordinative bulky $B(C_6F_5)_4^-$ could attribute to these results. The electrolyte effects of $B(C_6F_5)_4^-$ on reversibility of some simple redox-active molecules have been reported in literature [11].

The environment-sensitive molar ratio of rotational isomers can cause negligible change in absorption in solution. The UV-vis absorption spectrum of **2**·BF_4 in acetone displayed a CT absorption band characteristic of [Cu(diimine)(diphosphine)]$^+$ complexes (Fig. 3.15). The maximum wavelength (λ_{max}) and the molar extinction coefficient (ε) at λ_{max} of the CT absorption were 401 nm and 2.4×10^3 M^{-1} cm^{-1}, respectively. The red-shift of the absorption maximum of **2**·BF_4 compared with **1**·BF_4 ($\lambda_{max} = 378$ nm) is caused by previously reported diphosphine effects [12, 13]. Absorption maximum wavelengths of **2**·BF_4 and **2**·$B(C_6F_5)_4$ in acetone were identical. Since the effects of methyl substitution on the absorption maxima of copper(I) diimine complexes are known to be within a few nanometers [14–16], the difference in absorption between *i*-Cu^I and *o*-Cu^I is also expected to be small. The small difference in color is consistent with previous findings pertaining to the methylpyrimidine-based rotational isomers [17].

The luminescence of **2**·BF_4 and **2**·$B(C_6F_5)_4$ in acetone at room temperature, which is the same experimental condition as described for the luminescence of $\mathbf{1}^+$ (Sects. 3.3–3.7), was not detected; luminescence quantum yields of **1**·BF_4 and **2**·BF_4 were 0.02 % and less than 0.002 %, respectively. The negligible luminescence of $\mathbf{2}^+$

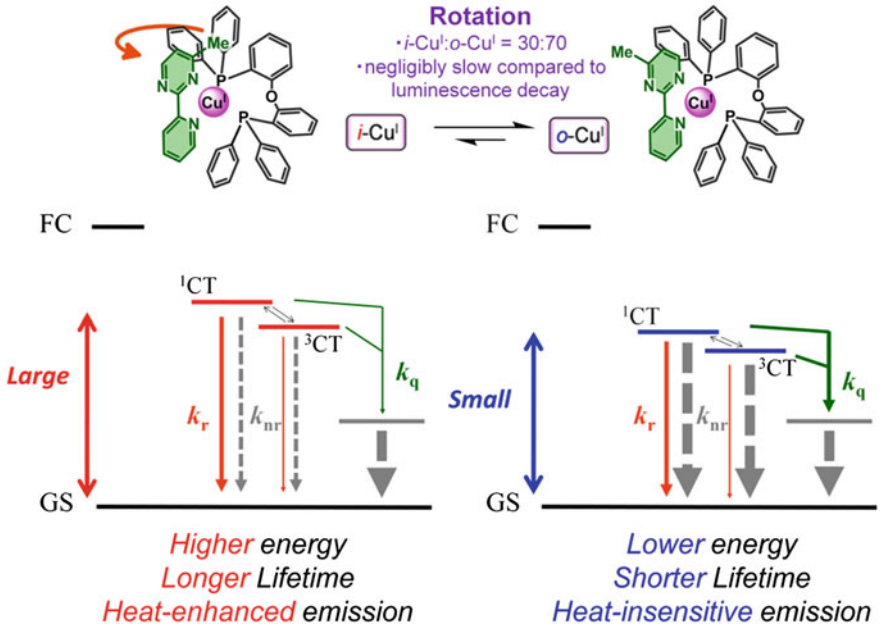

Fig. 3.13 Jablonski diagram showing difference in luminescence properties between *i*-Cu^I and *o*-Cu^I, based on well-established relationship between coordination structure and luminescence in copper(I) diimine complexes. GC: ground state. FC: Franck–Condon state. Physical parameters, k_r, k_{nr}, and k_q indicate radiative (*orange line*), nonradiative (*gray dotted line*), and solvent quenching (*green line*) rate constants, respectively

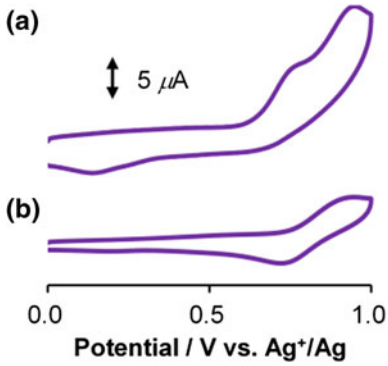

Fig. 3.14 Cyclic voltammogram of **a** **2**·BF_4 (0.4 mM) and **b** **2**·$B(C_6F_5)_4$ (0.4 mM) in 0.1 M Bu_4N·BF_4-CH_2Cl_2 at room temperature

compared with $\mathbf{1}^+$ is attributed to the different steric demands of the two diphosphines; DPEphos offers an enhanced protection towards structural deformations both in the ground and the excited state and additionally blue-shifts the absorption through electronic effects leading to a better emission performance for $\mathbf{1}^+$.[2] The values of luminescence quantum yields are consistent with well-established

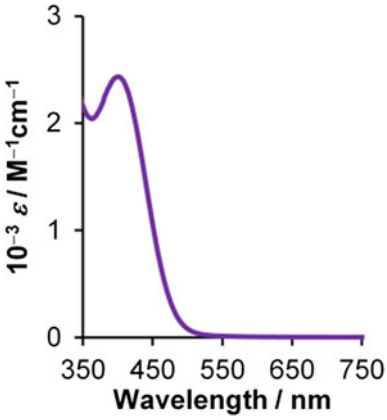

Fig. 3.15 Absorption spectrum of **2**·BF_4 in acetone at room temperature

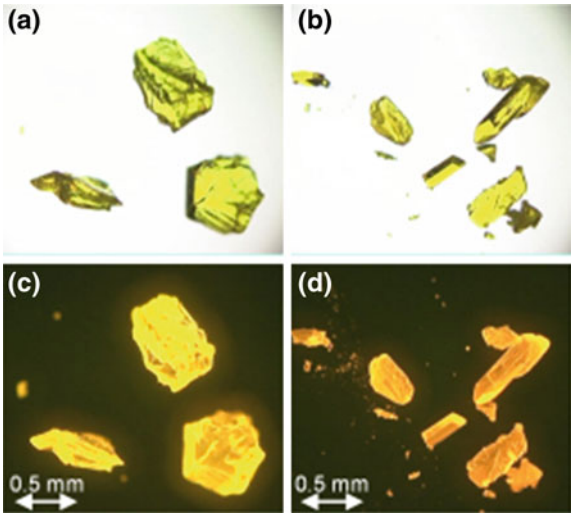

Fig. 3.16 Fluorescence microscope images of solids of **2**·BF_4 (**a**, **c**) and **2**·$B(C_6F_5)_4$ (**b**, **d**) in bright field (**a**, **c**) and under blue light excitation (**b**, **d**) at room temperature

photophysics of a family of [Cu(diimine)(diphosphine)] because of the large structural rearrangement that occurs in the photoexcited state of complexes containing less bulky Mepypm ligands compared with bulky diimines such as 2,9-dimethyl-1,10-phenanthlorine, and the high possibility of solvent coordination quenching due to the presence of the less bulky Mepypm [4, 5].

Solids of **2**·BF_4 and **2**·$B(C_6F_5)_4$ were yellow on appearance (Fig. 3.16a, c), and exhibited orange luminescence under UV and blue light excitation (Fig. 3.16b, d). The emission spectra of **2**·BF_4 and **2**·$B(C_6F_5)_4$ solids displayed CT luminescence characteristic of $[Cu(diimine)(diphosphine)]^+$ systems (Fig. 3.17) [6]. The maximum emission wavelength of **2**·BF_4 ($\lambda_{max} = 597$ nm) was blue-shifted compared with that of **2**·$B(C_6F_5)_4$ ($\lambda_{max} = 620$ nm) (Fig. 3.17). An enhancement in the solid-state luminescence over the solution luminescence, which is typical for

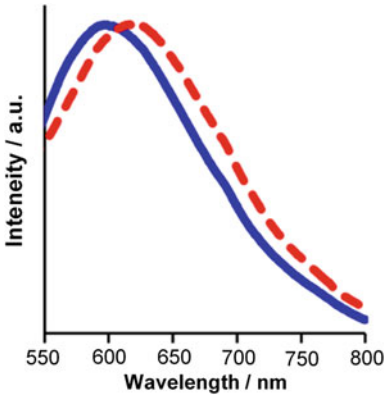

Fig. 3.17 Emission spectra of **2**·BF_4 (*blue*) and **2**·$B(C_6F_5)_4$ (*red, dotted line*) at room temperature

emissive copper(I) diimine complexes, was observed. The enhancement is attributed to inhibited structural relaxation in the solid state and/or additional solvent coordination to photoexcited species that occur in solution [6, 18–20]. The packing effects could outweigh the methyl group direction effects on emission. With a simple consideration of direction of pyrimidine in crystal structure (*o*-**2**·BF_4 and *i*-**2**·$B(C_6F_5)_4$), the emission of **2**·$B(C_6F_5)_4$ in the solid state is expected to be blueshifted than that of **2**·BF_4, because the methyl group near the copper center can prevent structural rearrangement in the photo-excited states and thus loss of energy according to well-established relationship between coordination structure and photophysics [6, 18–20]; we confirmed that both compounds appear to have similar dihedral angles in the ground state (Chap. 2). Since this simple discussion could not explain the blue-shift of **2**·BF_4 relative to **2**·$B(C_6F_5)_4$ (Fig. 3.17), there are possibilities that contribution of packing effects on emission wavelength could be larger than that of orientation of pyrimidine ring [21, 22]. The contribution of small structural difference caused by the packing effect to emission has been reported in some of Cu(I) complexes [21, 22].

3.9 Conclusion

I investigated photophysics of **1**·BF_4 in acetone (*i*-Cu^I:*o*-Cu^I = 30:70) by time-resolved emission spectra. The rate of rotational interconversion between *i*-Cu^I and *o*-Cu^I is sufficiently slow, suggesting that it may be possible to control the ring rotational motions. I conclude that the photoprocesses of the two isomers, *i*-Cu^I and *o*-Cu^I, are different in the identity of the excited state. Emission lifetime of *i*-Cu^I (τ = 40 ns) is much longer than that of *o*-Cu^I (τ = 2 ns) because of inhibition of both steric rearrangement and solvent-coordination quenching in the photo-excited state. Emission wavelength of *i*-Cu^I is blue-shifted from that of *o*-Cu^I.

Heat-sensitivity of emission of *i*-Cu^I is larger than that of *o*-Cu^I due to difference in photoprocesses between isomers. Both *i*-Cu^I and *o*-Cu^I coexist in the solution, and emit around room temperature.

Dual phosphorescence using metal complexes often requires the presence of two independent excited states. Our methods, selectively preparing one of the two states, provide dual emission caused by ring rotational isomerization, which can be a powerful way to handle promising photophysics and photoelectron devices based on metal complexes bearing π-conjugated chelating ligands.

References

1. Lo KKW, Zhang KY, Leung SK, Tang MC (2008) Angew Chem Int Ed 47:2213–2216
2. Glazer EC, Magde D, Tor Y (2007) J Am Chem Soc 129:8544–8551
3. DeAmond MK, Carlin CM (1981) Coord Chem Rev 36:325–355
4. Cuttell DG, Kuang SM, Fanwick PE, McMillin DR, Walton RA (2002) J Am Chem Soc 124:6–7
5. Kuang SM, Cuttell DG, McMillin DR, Fanwick PE, Walton RA (2002) Inorg Chem 41:3313–3322
6. Armaroli N, Accorsi G, Cardinali F, Listorti A (2007) Top Curr Chem 280:69–115
7. Vorontsov II, Graber T, Kovalevsky AY, Novozhilova IV, Gembicky M, Chen Y-S, Coppens P (2009) J Am Chem Soc 131:6566–6573
8. Siddique ZA, Yamamoto Y, Ohno T, Nozaki K (2003) Inorg Chem 42:6366–6378
9. Turro NJ (1991) Modern Molecular Photochemistry. University Science Books, Sausalito
10. Linfoot CL, Richardson P, Hewat TE, Moudam O, Forde MM, Collins A, White F, Robertson N (2010) Dalton Trans 39:8945–8956
11. LeSuer RJ, Geiger WE (2000) Angew Chem Int Ed 39:248–250
12. McCormick T, Jia W-L, Wang S (2006) Inorg Chem 45:147–155
13. Sakaki S, Mizutani H, Kase Y-I, Inokuchi K-J, Arai T, Hamada T (1996) J Chem Soc Dalton Trans 1909–1914
14. Everly RM, Ziessel R, Suffert J, McMillin DR (1991) Inorg Chem 30:559–561
15. Cunningham CT, Cunningham KLH, Michalec JF, McMillin DR (1999) Inorg Chem 38:4388–4392
16. Del Paggio AA, McMillin DR (1983) Inorg Chem 22:691–692
17. Nomoto K, Kume S, Nishihara H (2009) J Am Chem Soc 131:3830–3831
18. Zhang Q, Zhou Q, Cheng Y, Wang L, Ma D, Jing X, Wang F (2004) Adv Mater 16:432–436
19. Armaroli N, Accorsi G, Holler M, Moudam O, Nierengarten J-F, Zhou Z, Wegh RT, Welter R (2006) Adv Mater 18:1313–1316
20. Hsu C-W, Lin C–C, Chung M-W, Chi Y, Lee G-H, Chou P-T, Chang C-H, Chen P-Y (2011) J Am Chem Soc 133:12085–12099
21. Kovalevsky AY, Gembicky M, Novozhilova IV, Coppens P (2003) Inorg Chem 42:8794–8802
22. Cunningham CT, Moore JJ, Cunningham KLH, Fanwick PE, McMillin DR (2000) Inorg Chem 39:3638–3644

Chapter 4
Repeatable Copper(II)/(I) Redox Potential Switching Driven Visible Light-Induced Coordinated Ring Rotation

Abstract Repeatable PET-driven rotational isomerization is described. I demonstrated the conversion of light stimuli into electrochemical potential via reversibly working artificial molecular rotation, using two strategies, $DMFc^+$ system and partial oxidation system. In both systems, photoinduced electron transfer from copper complex to electron acceptor plays a key role for the photo- and heat-driven rotation.

Keywords Redox · Photochromism · Copper complex · Molecular switch · Photodriven rotation

4.1 Introduction

4.1.1 The Aim of this Study

As I described in Chap. 1, the aim is to harness the functions of molecules that can convert the energy of external stimuli into useful responses based on the capacities of molecular motion. Our group has developed an electrochemical potential response from an artificial molecular rotor, pyrimidine ring rotation in copper complexes, with a stimulus-convertible function, based on adding chemical reagents (Sect. 1.4). The major problem to be solved in this system is how best to drive the pyrimidine rotational isomerization in the energetically uphill direction to extract a responsive electric signal repeatedly. The aim of this study is to drive this system with light stimuli. I succeeded in driving this rotational isomeric system using visible light illumination through a PET process (Fig. 4.1).

M. Nishikawa, *Photofunctionalization of Molecular Switch Based on Pyrimidine Ring Rotation in Copper Complexes*, Springer Theses,
DOI: 10.1007/978-4-431-54625-2_4, © Springer Japan 2014

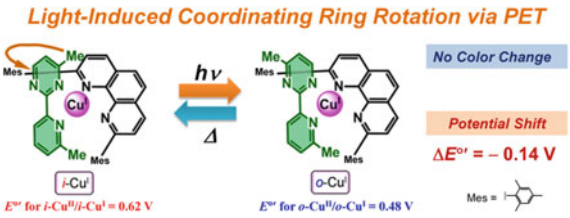

Fig. 4.1 Conceptual diagram showing the photo- and heat-driven pyrimidine ring rotational isomerization of $3{\cdot}BF_4$

4.1.2 Molecular Design

It should be noted that both $1{\cdot}BF_4$ and $2{\cdot}BF_4$, described in Chaps. 2, and 3 did not exhibit reversible redox activities; therefore, electronic signals cannot be extracted from rotation in these complexes.

I employed a 4-methyl-2-(6′-methyl-2′-pyridyl)pyrimidine (MepmMepy) ligand, which is similar to our previously described ligand, Mepypm, but includes an additional methyl group at the 6-position of the pyridyl moiety. The additional methyl group is expected to extend the MLCT excited state lifetime (Sect. 1.2) [1]. 2, 9-Dimesityl-1,10-phenanthroline (L_{Mes}) was used as an auxiliary ligand because the bulky mesityl group yielded a similar MLCT lifetime extension; L_{Mes} also helps to prevent undesirable formation of a homoleptic complex [2–5]. I employed a novel copper(I) complex bearing two bidentate diimines, $3{\cdot}BF_4$ ($3^+ = [Cu(MepmMepy)(L_{Mes})]^+$) (Fig. 4.1).

4.1.3 Contents of this Chapter

I here describe the molecular system in which electrochemical signals can be repeatedly extracted by converting bistable states related to an intramolecular ligand rotational motion, which is driven by visible light illumination, using newly synthesized $3{\cdot}BF_4$. The molecular structure for relating a redox reaction and a motion consists of a copper center and a coordinated unsymmetrically substituted pyrimidine derivative, whose rotational isomerization causes a redox potential shift. The thermodynamic and kinetic parameters of rotational and redox reactions were analyzed by electrochemical measurements at several temperatures, by considering four isomers related to copper(II)/(I) states and rotational isomeric states. The important feature of this system is that the pyrimidine ring rotation is frozen in the copper(I) state (rate constant for the rotation, $k_{Ii\rightarrow o} = 10^{-4}$ s^{-1}) but is active in the copper(II) state ($k_{IIi\rightarrow o} = 10^{-1}$ s^{-1}) at 203 K. The compound makes a bypass route to the isomeric metastable copper(I) state, via a tentative copper(II) state formed by photoelectron transfer (PET) in the presence of a redox mediator, decamethylferrocenium ion ($DMFc^+$), or upon a partial oxidation of the complex. Photodriven and heatdriven rotation in the copper(I) state with a repeatable potential shift ($\Delta E^{\circ\prime} = 0.14$ V) was monitored by cyclic voltammograms in the

electrolyte organic solution of the complex. Considering both absorption spectra changes upon chemical oxidation and literatures, a color change caused by rotational isomerization is negligible in this new type of photoswitchable system, unlike well-known photoresponsivity using photochromic molecules. A significant redox potential shift associated with the copper(II)/(I) transition accompanied the rotation, thereby providing a new type of molecular signaling system.

4.2 Experimental Section

Materials. 6-Methyl-2-pyridinecarboximidamide monohydrochloride [6, 7], tetrakis(acetonitrile)copper(I) tetrafluoroborate [8], 2,9-dimesityl-1,10-phenanthroline (L_{Mes}) [2, 3], and decamethylferrocenium tetrafluoroborate [9] were also prepared according to methods described in the literature. Other chemicals were used as purchased.

Synthesis of 4-Methyl-2-(6′-methyl-2′-pyridyl)pyrimidine (MepmMepy) (Scheme 4.1). MepmMepy was newly synthesized by Nomoto et al., who are co-author of a report related to this chapter, according to modified method described in literature [10]. I contribute to characterization of this compound. Under a nitrogen atmosphere, 6-methyl-2-pyridinecarboximidamide (1.0 g, 5.8 mmol) was dissolved in an ethanol solution of sodium ethoxide (prepared from 175 mg of sodium and 60 mL of ethanol) at room temperature. Acetylacetoaldehyde dimethylacetal (1 mL, 8 mmol) was added to the mixture. The reaction mixture was refluxed for 3 days. The reaction mixture was cooled to room temperature and acidified with acetic acid. The solvent was evaporated and the residue dissolved in water and extracted with CH_2Cl_2. The organic layer was dried over sodium sulfate, filtered, and evaporated. The residue was chromatographed on an alumina gel column eluted with ethyl acetate-hexane (1:1 v/v). The solvent was evaporated to obtain a colorless powder: yield, 0.285 g (1.54 mmol, 27 %). ^{1}H NMR (500 MHz, $CDCl_3$): δ 8.76 (d, J = 5.1 Hz, 1H), 8.29 (d, J = 7.8 Hz, 1H), 7.74 (t, J = 7.7 Hz, 1H), 7.26 (d, 1H), 7.16 (d, J = 5.1 Hz, 1H), 2.72 (s, 3H), 2.65 (s, 3H). ^{13}C NMR (100 MHz, $CDCl_3$): δ 24.7, 25.1, 119.9, 121.0, 124.7, 137.2, 154.7, 157.5, 159.1, 163.8, 168.0. Elemental analysis. Calculated for $C_{11}H_{11}N_3$: C 71.33, H 5.99, N 22.69. Found C 71.53, H 6.19, N 22.40.

Synthesis of [Cu(MepmMepy)(L_{Mes})]BF_4 (3·BF_4) (Scheme 4.2). Under a nitrogen atmosphere, $[Cu(MeCN)_4]BF_4$ (28.3 mg, 0.0900 mmol) was added to L_{Mes} (37.1 mg, 0.0891 mmol) in 5 mL CH_2Cl_2. To the resultant orange solution, MepmMepy (15.7 mg, 0.0848 mmol) was added, and the color of the solution changed immediately to dark red. The reaction mixture was stirred for 30 min. The solution was filtered, and diethyl ether (15 mL) was added to the solution to precipitate the product, a deep red solid of 3·BF_4: yield, 42 mg (0.055 mmol, 65 %). ^{1}H NMR (500 MHz, CD_2Cl_2 273 K): δ 8.71−8.66 (m, *i*-3H + *o*-2H), 8.30 (d, J = 7.7 Hz, *i*-1H), 8.24 (d, J = 7.7 Hz, *o*-1H), 8.20 (s, *i*-2H), 8.19 (s, *o*-2H), 8.14 (d, J = 5.4 Hz, *o*-1H), 7.87−7.80 (m, *i*-3H + *o*-3H), 7.30 (d, J = 4.1 Hz, *i*-1H),

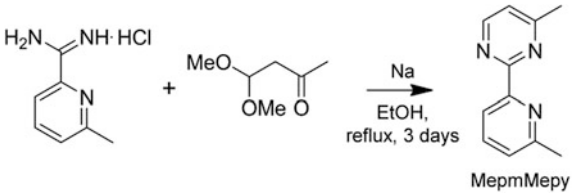

Scheme 4.1 Synthesis of MepmMepy

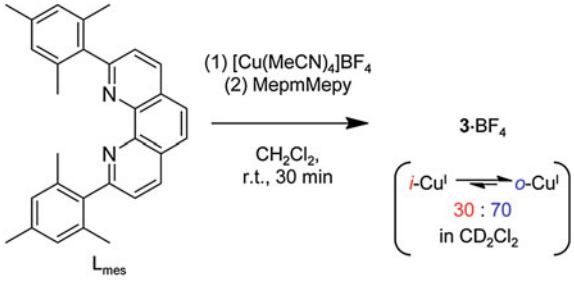

Scheme 4.2 Synthesis of $3{\cdot}BF_4$

7.29 (d, $J = 7.7$ Hz, *o*-1H), 7.25 (d, $J = 5.6$ Hz, *o*-1H), 7.22 (d, $J = 4.8$ Hz, *i*-1H), 6.39 (s, *i*-2H), 6.33 (s, *i*-2H), 6.32 (s, *o*-2H), 6.28 (s, *o*-2H), 2.64 (s, *o*-3H), 2.05 (s, *i*-3H), 1.97 (s, *o*-3H), 1.95 (s, *o*-6H), 1.93 (s, *i*-6H), 1.90 (s, *i*-3H), 1.77 (s, *o*-6H), 1.69 (s, *i*-6H), 1.68 (s, *o*-6H), 1.61 (s, *i*-6H). Elemental analysis. Calculated for $C_{41}H_{39}N_5CuBF_4{\cdot}C_{0.1}H_{0.2}Cl_{0.2}$: C 64.90, H 5.19, N 9.21. Found C 64.71, H 5.33, N 8.92.

X-ray Structural Analysis. A red single crystal of $3{\cdot}BF_4{\cdot}CH_2Cl_2{\cdot}0.5$hexane was obtained by diffusing hexane into a dichloromethane solution of $3{\cdot}BF_4$. Diffraction data were collected with an AFC10 diffractometer coupled with a Rigaku Saturn charge-coupled device (CCD) system equipped with a rotating-anode X-ray generator producing graphite-monochromated MoKα radiation ($\lambda = 0.7107$ Å). Lorentz polarization and numerical absorption corrections were performed with the program Crystal Clear 1.3.6. The structure was solved by the direct method using SIR 92 software [11] and refined against F^2 using SHELXL-97 [12]. WinGX software was used to prepare the material for publication [13]. The crystallographic data are listed in Table 4.1. The isomeric structures were almost identical, except for the position of the methyl group. Occupancy refinement of the cyrstallographic disorder gave a *i*-:*o*- = 3:7 isomer ratio, as analyzed by the PART option of the SHELX-97 program. The disorders of the BF_4^- molecules in the crystals were analyzed by the PART, ISOR, DELU, and SIMU options of the SHELX-97 program.

Instrumentation. Nuclear magnetic resonance (NMR) spectra at several temperatures in the dark were recorded using a Bruker DRX 500 spectrometer, using a ca. 20 min data-recording interval. The ^{13}C NMR spectrum of MepmMepy was

Table 4.1 Crystallographic data of $3{\cdot}BF_4{\cdot}CH_2Cl_2{\cdot}0.5$ Hexane

	$3{\cdot}BF_4{\cdot}CH_2Cl_2{\cdot}0.5$Hexane
Molecular formula	$2(C_{41}H_{38}CuN_5)$, C_6H_{14}, $2(BF_4)$, $2(CH_2Cl_2)$
Mw/g mol^{-1}	1758.27
Crystal system	Triclinic
Space group	P-1
T/K	113
a/Å	14.4589(16)
b/Å	14.9720(18)
c/Å	21.711(3)
α/°	87.903(5)
β/°	76.771(4)
γ/°	70.003(4)
V/Å^3	4294.9(9)
Z	2
Reflections collected	34,468
Independent reflections	18,855
R_{int}	0.0293
ρ_{calcd}/g cm^{-3}	1.426
λ/Å	0.7107
μ/cm^{-1}	0.812
R_1^a	0.0805
wR_2^b	0.2408
GOF^c	1.055

[a] $R_1 = \Sigma||F^o|-|F^c||/\Sigma|F^o|$ $(I > 2\sigma(I))$
[b] $wR_2 = [\Sigma(w(F^{o2}-F^{c2})^2/\Sigma w(F^{o2})^2]^{1/2}$ $(I > 2\sigma(I))$
[c] $\mathrm{GOF} = [\Sigma(w(F^{o2}-F^{c2})^2/\Sigma(N^r-N^p)^2]$

recorded using a JEOL ECX 400 spectrometer. The reported chemical shifts of the solvent residual peaks were used for calibration of the NMR spectra in chloroform-d_1 ($CDCl_3$, $\delta = 7.26$ ppm for ^{1}H, $\delta = 77.16$ ppm for ^{13}C) and dichloromethane-d_2 (CD_2Cl_2, $\delta = 5.32$ ppm for ^{1}H) [14]. UV–vis absorption spectra in the dark were recorded with a JASCO V-570 spectrometer and a Hewlett-Packard 8453 spectrometer equipped with a USP-203-A UNISOKU cryostat, using a quartz cell with a 1 cm optical path length. Steady-state corrected emission spectra were recorded with a HITACHI F-4500 spectrometer. Electrochemical measurements were recorded with an ALS 750A electrochemical analyzer (BAS. Co., Ltd.) and a HZ-3000 electrochemical analyzer (Hokuto Denko Co. Ltd.), each equipped with a UNISOKU cryostat. The working electrode was a 0.3 mm o.d. glassy carbon electrode; a platinum wire served as the auxiliary electrode, and the reference electrode was an Ag^+/Ag electrode (a silver wire immersed in 0.1 M Bu_4NClO_4/0.01 M $AgClO_4/CH_3CN$). The solutions were deoxygenated with pure argon prior to the electrochemical measurements. Light irradiation was performed using a MAX-302 xenon lamp (ASAHI SPECTRA) equipped with an optical fiber with a long-pass filter (cut-on 400 nm) or a bandpass filter (central wavelength 450 nm, full width at half-maximum 80 nm).

Thermodynamic and Kinetic Analysis. The molar ratios of isomers of $3{\cdot}BF_4$ in solution at several temperatures were determined from the ^1H NMR signal integration in the methyl group on the basis of pyrimidine moieties. The broad spectra at around room temperature were excluded from the thermodynamic analysis. The experimental cyclic voltammograms were simulated using BASi Digisim 3.03a software, based on two independent double-step electron transfer systems. The isomer equilibrium constants in the copper(II) state were derived from the experimentally obtained equilibrium constants of isomers in the copper(I) state and the two redox potentials of *i*- and *o*-isomers. The van't Hoff plots were based on an equilibrium constant of [*o*-isomer]/[*i*-isomer]. The molar ratios of isomers at variable temperatures were calculated from extrapolations of the van't Hoff plots. The rate constants for rotational processes from the *i*- to *o*-isomer were determined from the simulation analysis of the cyclic voltammograms. The rates of the rotations at various temperatures were calculated from the slopes and intercepts of the Arrhenius plots. The good fit of simulated curves with the experimental voltammograms confirmed the validity of the analyses.

Monitoring of Photorotation from *i*-Cu^I to *o*-Cu^I in the Redox Mediator System. The electrochemical cell, shielded from room light by covering with aluminum foil, was equipped with electrodes, a cryostat, and the optical fiber connected to the xenon lamp. The electrochemical cells were interfaced with a cryostat container, whose size and shape fitted the cells. The opening between the cell and the container is filled with methanol. The electrochemical measurements were performed in the static solution at 203 K in the dark after vigorous stirring. Under an argon atmosphere, a 2 mL 0.1 M Bu_4NBF_4–CH_2Cl_2 solution of $3{\cdot}BF_4$ (0.45 mM) was cooled at 203 K in the dark, followed by electrochemical measurements. Then, the solution was stirred and photoirradiated with visible light ($\lambda > 400$ nm) at 203 K for 60 min, followed by further measurements, which showed a negligible change in the voltammograms. Then, a 100 μL deoxygenated CH_2Cl_2 solution of $DMFc{\cdot}BF_4$ (1.8 mM, 4 equiv to $3{\cdot}BF_4$) was added to the solution at room temperature. The solution was cooled at 203 K in the dark, followed by measurements in the initial state. Then, the solution was stirred at 203 K in the dark for several minutes, followed by measurements to check that no changes were detected in the voltammogram with time. Then, the solution was stirred and photoirradiated with visible light ($\lambda > 400$ nm) at 203 K for 60 min, followed by measurements which showed considerable voltammogram changes. The solution was stirred at 203 K in the dark for several minutes, followed by measurements for the persistence of the irradiated state. After a 2 min heating of the solution to 250 K in the dark with stirring, the solution was cooled to 203 K in the dark, followed by measurements in the warmed state. The operations were repeated three times, with a 60 min photoirradiation at 203 K and a 2 min heating in the dark at 250 K, to achieve repeatable voltammogram changes. Then, the operations were performed using blue light ($\lambda = 450 \pm 40$ nm) instead of visible light. The solution was heated to 225 K in the dark, followed by measurements performed at 225 K instead of at 203 K. The solution was stirred and

photoirradiated with 20 min of visible light ($\lambda > 400$ nm) at 225 K, followed by measurement at 225 K, which showed a negligible change.

Monitoring of Photorotation from *i*-Cu^{I} to *o*-Cu^{I} in the Partially Oxidized System. The measurements were performed using the same electrochemical cell mentioned above. Electrochemical measurements were performed for the static solution at 225 K in the dark after vigorous stirring. Under an argon atmosphere, a 100 μL of a deoxygenated acetone solution of ammonium hexanitratocerate (IV) (0.3 mM, 0.4 equiv to 3·BF_4) was added to 2 mL of 0.1 M Bu_4N·BF_4–CH_2Cl_2 solution of 1·BF_4 (0.75 mM) at room temperature. Then, the solution was cooled to 225 K in the dark, followed by measurements in the initial state. The solution was stirred and photoirradiated with visible light ($\lambda > 400$ nm) at 225 K for 3 min, followed by measurements in the irradiated state, which gave a considerable voltammogram change. The solution was stirred for 20 min at 225 K in the dark, followed by the measurements. The operation was repeated 10 times, with 3 min of visible light ($\lambda > 400$ nm) irradiation at 225 K followed by a 20 min interval at 225 K in the dark, to achieve a repeatable voltammogram change.

4.3 Synthesis and Characterization

MepmMepy was newly synthesized by a condensation of a reported amidine [8, 9] with acetylacetoaldehyde dimethylacetal, according to the modified procedure described in the literature [10]. A new compound, [Cu(MepmMepy)(L_{Mes})]BF_4 (3·BF_4), was synthesized by a reaction of tetrakis(acetonitrile)copper(I) tetrafluoroborate ([Cu(MeCN)$_4$]BF_4) with MepmMepy and L_{Mes} [2, 3] in dichloromethane at room temperature, according to the slightly modified procedures described in our previous literature (see Sect. 4.2) [15]. The sample of 3·BF_4, which contained a slight amount of CH_2Cl_2, was employed for the experiments in the manuscript, considering the elemental analysis results; the weight ratio of CH_2Cl_2 to 3·BF_4 is 1 %. ^{1}H NMR measurement in CD_2Cl_2 revealed a presence of the residual dichloromethane, considering the reported values [14]. For clarity, I omitted the remained solvent.

X-ray structural analysis of 3·BF_4·CH_2Cl_2·0.5hexane reveals that both *i*- and *o*-coordination forms were present in the same crystal (Fig. 4.2 and Table 4.1). The crystal structure was treated as a disorder between the *i*- and *o*-forms, considering that the isomeric structures are almost identical, except for the position of the methyl group. Occupancy refinement of the disorder gave a *i*-Cu^{I}:*o*-Cu^{I} isomer ratio = 30:70.

The rotational behavior of 3·BF_4 in a solution state was investigated by nuclear magnetic resonance (NMR) spectroscopy. The ^{1}H NMR spectrum in dichloromethane-d_2 at 273 K shows two sets of signals, which were assigned to *i*-Cu^{I} and *o*-Cu^{I} according to their chemical shifts, after consideration of the shielding effects of the copper and L_{Mes} moieties (Figs. 4.3 and 4.4). Chemical shift of two methyl groups of MepmMepy is found at $\delta = 2.73$ and 2.66 ppm. I assigned the signals in

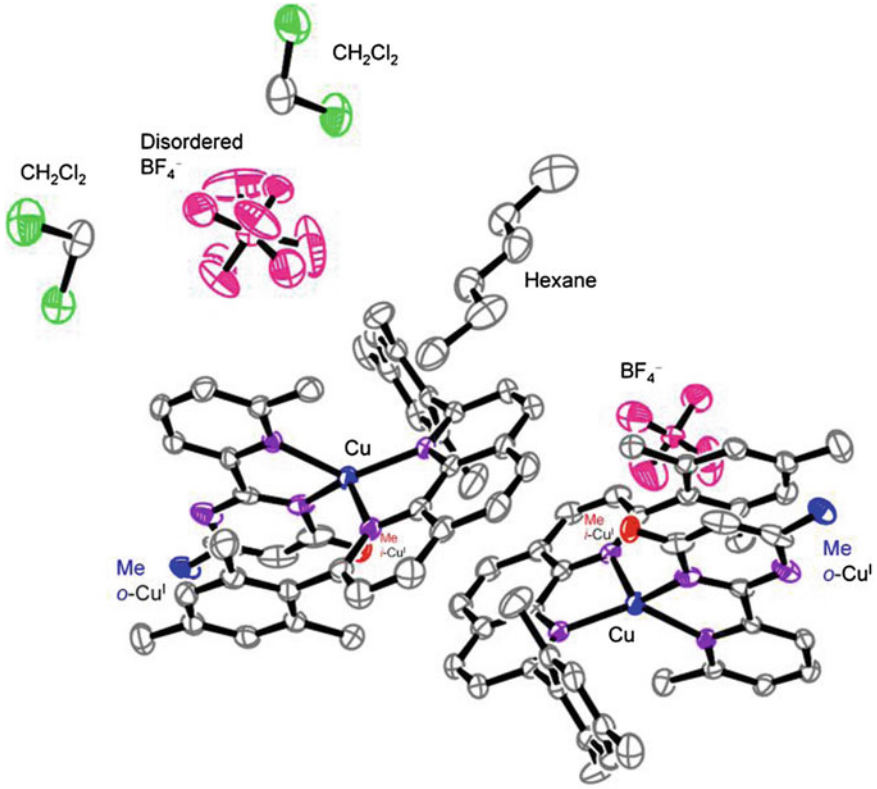

Fig. 4.2 ORTEP view of $3{\cdot}BF_4{\cdot}CH_2Cl_2{\cdot}0.5$hexane. The displacement ellipsoids are drawn at a 50 % probability level. Hydrogen atoms are omitted for clarity

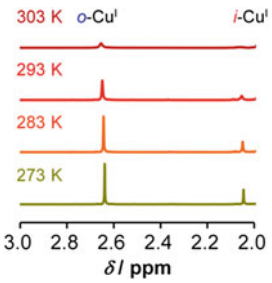

Fig. 4.3 Temperature dependence of the methyl signal on the pyrimidine moiety in the ^{1}H NMR spectrum of $3{\cdot}BF_4$ in CD_2Cl_2 in the *dark*

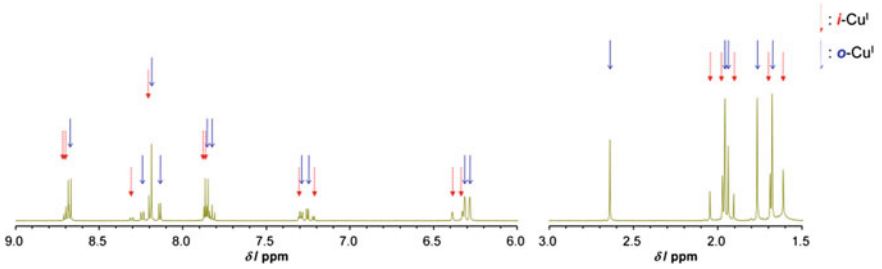

Fig. 4.4 ^{1}H NMR spectrum of 3·BF_4 in CD_2Cl_2 in the *dark* at 273 K

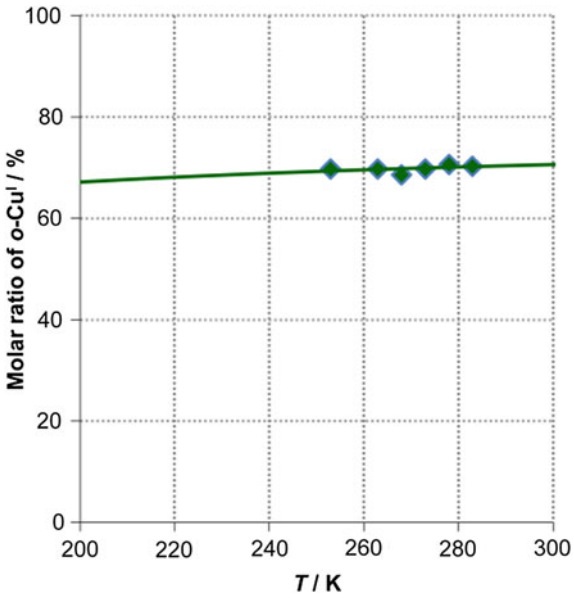

Fig. 4.5 The ratios of *o*-Cu^{I} at variable temperatures, estimated from the signal integration of ^{1}H NMR spectra in CD_2Cl_2. The experimental values are shown as the dots, and the regression curve of van't Hoff plot is drawn in line

3·BF_4 at $\delta = 2.66$ and 1.99 ppm as *o*-Cu^{I} and $\delta = 2.07$ and 1.93 ppm as *i*-Cu^{I}, respectively, because the shielding effects on signal of methyl group on pyrimidine in *o*-Cu^{I} are expected to be small. Broadening of the peaks upon heating indicates that the two isomers coexisted and interconverted via rotational motions (Fig. 4.3). The molar ratio of *i*-Cu^{I} and *o*-Cu^{I}, estimated from signal integration, remained fixed at 30:70 over the range 200–300 K (Fig. 4.5).

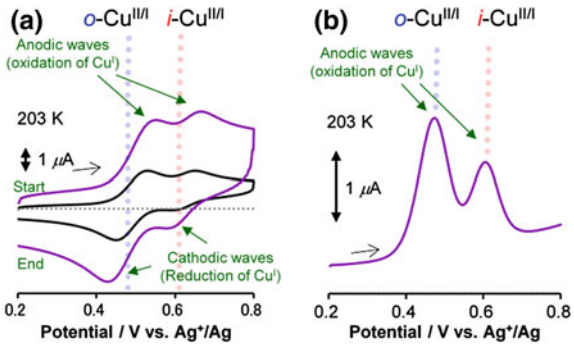

Fig. 4.6 **a** Cyclic voltammograms of $3{\cdot}BF_4$ (0.45 mM) in 0.1 M Bu_4NBF_4-CH_2Cl_2 at a scan rate of 250 (*purple line*) and 50 mV s^{-1} (*black line*) at 203 K. **b** Differential pulse voltammogram under the same condition as (**a**)

4.4 Electrochemistry

Two points are required to manipulate an electron transfer via rotation processes: (i) the copper(II/I) redox potential between *i*- and *o*- isomers is different, and (ii) the rotational interconversion can be frozen and activated at an accessible temperature range [15–18]. I conducted cyclic voltammetry, as it provides information on both redox properties and rotational behaviors.

A voltammogram at low temperature (203 K) in Bu_4NBF_4–CH_2Cl_2 at a scan rate of both 250 and 50 mV s^{-1} showed two reversible waves derived from the *o*-$Cu^{II/I}$ and *i*-$Cu^{II/I}$ redox reactions at $E^{\circ\prime} = 0.48$ and 0.62 V versus Ag^+/Ag, respectively (Fig. 4.6a) ($E^{\circ\prime} = 0.89$ and 1.03 V vs. $DMFc^{+/0}$). The value of $E^{\circ\prime}$ for *i*-$Cu^{II/I}$ is more positive than that of *o*-$Cu^{II/I}$, because a bulky substituent around the copper center shifted the potential toward positive values by preventing the square planar geometry favored in the copper(II) state (Sect. 1.2) [19, 20]. The prominence of the wave at $E^{\circ\prime} = 0.48$ V compared with that at $E^{\circ\prime} = 0.62$ V was consistent with the molar ratios (*i*-Cu^I:*o*-Cu^I = 30:70) estimated from ^1H NMR measurements. A differential pulse voltammogram showed both *o*-$Cu^{II/I}$ and *i*-$Cu^{II/I}$ waves, where the peak currents reflect *i*-Cu^I:*o*-Cu^I (Fig. 4.6b). Repeated potential sweeps in cyclic voltammetry gave identical current ratios of the isomers. The nice reversibility of these two waves suggests that four states, *i*-Cu^I, *o*-Cu^I, *i*-Cu^{II}, and *o*-Cu^{II}, are sufficiently stable without subsequent chemical degradation. A reduction wave of $3{\cdot}BF_4$ was not observed with potential sweeps down to −1.8 V versus Ag^+/Ag (Fig. 4.7).

As the temperature was increased to 225 K at a scan rate of 250 mV s^{-1} (Fig. 4.8a, purple line), the cathodic wave (*i*-$Cu^{II} + e^- \rightarrow$ *i*-Cu^I) slightly decreased; the decrease was more apparent at a scan rate of 50 mV s^{-1} (Fig. 4.8a, black line). Further warming to 275 K caused a transformation of the entire voltammogram, as if there was one cathodic wave (*o*-$Cu^{II} + e^- \rightarrow$ *o*-Cu^I) (Fig. 4.8b, purple line).

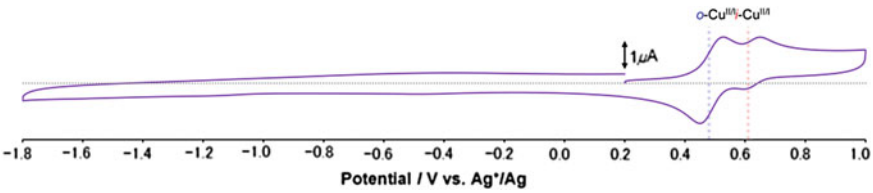

Fig. 4.7 Cyclic voltammograms of $3{\cdot}BF_4$ (0.45 mM) in 0.1 M Bu_4NBF_4–CH_2Cl_2 at a scan rate of 50 mV s^{-1} at 203 K

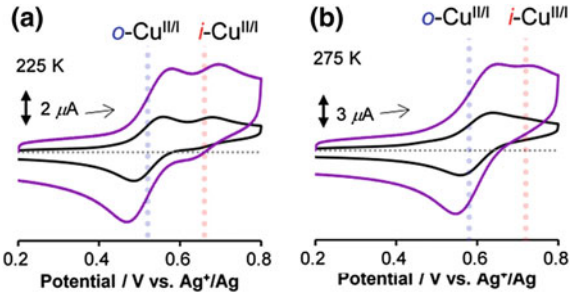

Fig. 4.8 Cyclic voltammograms of $3{\cdot}BF_4$ (0.45 mM) in 0.1 M Bu_4NBF_4–CH_2Cl_2 at a scan rate of 250 (*purple line*) and 50 mV s^{-1} (*black line*) at 225 K **a** and 275 K **b** in the *dark*

The convergence into a single wave suggests that oxidation promotes a rotation from *i*-Cu^{II} to *o*-Cu^{II} on the time scale of the potential sweep (*i*-Cu^{I}-e^{-} → *i*-Cu^{II} → *o*-Cu^{II}) [21–25]. The preference of the square planar geometry in the copper(II) state converted *i*-Cu^{II} into *o*-Cu^{II} because of steric repulsion of the methyl group via a thermally activated process. From the voltammograms at a scan rate of 50 mV s^{-1}, it appears as if there is a single reversible redox process when both interconversions in copper(II) and copper(I) states are sufficiently rapid (Fig. 4.8b). This trend was continuously observed in voltammograms at 203, 215, 225, 235, 245, 255, 265, 275, and 285 K at a scan rate of 25, 50, 100, 250 mV s^{-1} (Fig. 4.9).

As described above, I deduced that the shape of the voltammogram is mostly determined by the competence of the potential sweep and the nature of the rotational dynamics. A quantitative simulation analysis using cyclic voltammograms (Fig. 4.9 and Table 4.2) provides further constraints on the experimental conditions at which photodriven *i*-Cu^{I} → *o*-Cu^{I} rotation can be achieved [21–25]. I assumed a square scheme between four stable isomers, *i*-Cu^{I}, *o*-Cu^{I}, *i*-Cu^{II}, and *o*-Cu^{II}, and reproduced the experimental voltammograms at several temperatures. These simulations provide thermodynamic and kinetic parameters for the redox potentials and rotations in both copper(I) and copper(II) states, as described in Fig. 4.9 and Table 4.2 [21–25].

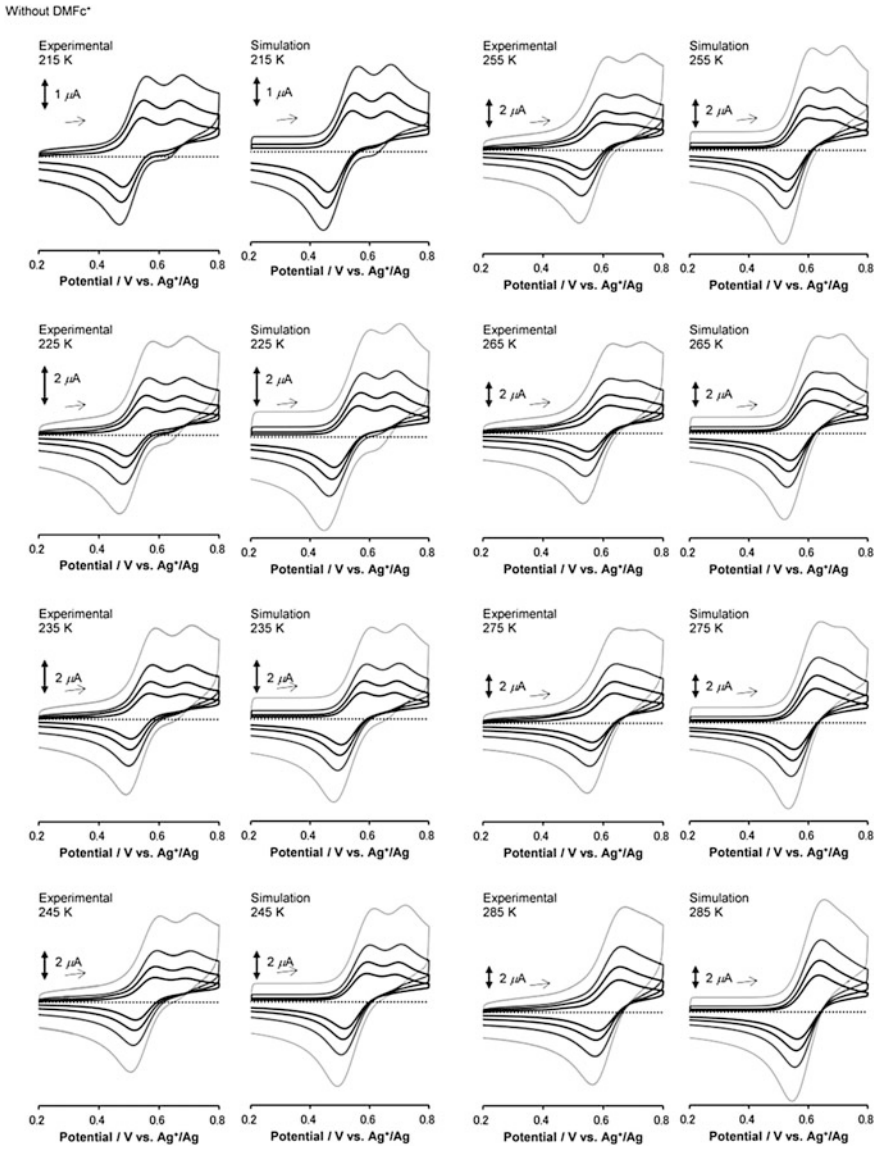

Fig. 4.9 Experimental and simulated cyclic voltammograms of $3{\cdot}BF_4$ (0.45 mM) at several temperatures in 0.1 M Bu_4NBF_4–CH_2Cl_2 in the *dark* at the scan rate of 250, 100, 50, and 25 mV s^{-1}

Table 4.2 Selected parameters obtained from the simulated cyclic voltammograms (Fig. 4.9) of $3{\cdot}BF_4$ at the scan rate of 250, 100, 50, and 25 mV s^{-1} in 0.1 M Bu_4NBF_4–CH_2Cl_2

Temperature/K	285	275	265	255	245	235	225	215	203
$E^{\circ\prime}{}_o$/V[a]	0.59	0.58	0.57	0.56	0.55	0.54	0.52	0.5	0.48
$E^{\circ\prime}{}_i$/V[b]	0.73	0.72	0.71	0.7	0.69	0.68	0.66	0.64	0.62
$E^{\circ\prime}{}_o$/V[c]	0.93	0.93	0.93	0.93	0.92	0.92	0.91	0.9	0.89
$E^{\circ\prime}{}_i$/V[d]	1.07	1.07	1.07	1.07	1.06	1.06	1.05	1.04	1.03
K_I[e]	2.3	2.3	2.3	2.3	2.3	2.3	2.3	2.3	2.3
K_{II}[f]	688	846	1057	1345	1744	2313	3144	4399	7754
k_{ETi}/cm^{-1}[g]	0.3	0.1	0.05	0.05	0.02	0.01	0.008	0.005	0.002
k_{ETo}/cm^{-1}[g]	0.05	0.02	0.01	0.008	0.005	0.003	0.002	0.0015	0.0005
$k_{Ii\rightarrow o}$/s^{-1}[h]	10	3	1	0.3	0.1	<0.1	<0.1	<0.1	<0.1
$k_{IIi\rightarrow o}$/s^{-1}[i]	>10	>10	>10	10	5	3	1	0.5	<0.1
α[j]	0.5	0.5	0.5	0.5	0.5	0.5	0.5	0.5	0.5
R_u/W[k]	1500	1500	1500	2000	2000	2000	3000	3000	3000
C_{dl} μF[l]	5×10^{-6}	5×10^{-6}	5×10^{-6}	5×10^{-6}	5×10^{-6}	5×10^{-6}	5×10^{-6}	5×10^{-6}	5×10^{-6}
D/cm^2 s^{-1}[m]	5.5×10^{-6}	4.5×10^{-6}	4.0×10^{-6}	3.5×10^{-6}	3.0×10^{-6}	2.5×10^{-6}	2.0×10^{-6}	1.5×10^{-6}	9×10^{-7}

[a] Redox potential for o-$Cu^{II/I}$ versus Ag^+/Ag
[b] Redox potential for i-$Cu^{II/I}$ versus Ag^+/Ag
[c] Redox potential for o-$Cu^{II/I}$ versus $DMFc^{+/0}$
[d] Redox potential for i-$Cu^{II/I}$ versus $DMFc^{+/0}$
[e] Equilibrium constant, set as [o-Cu^I]/[i-Cu^I]
[f] Equilibrium constant, set as [o-Cu^{II}]/[i-Cu^{II}]
[g] Rate constant for the electron transfer
[h] Rate constant for the i-$Cu^I \rightarrow o$-Cu^I rotation
[i] Rate constant for the i-$Cu^{II} \rightarrow o$-Cu^{II} rotation
[j] Transfer coefficient
[k] Resistance
[l] Capacitance
[m] Diffusion coefficient for all species

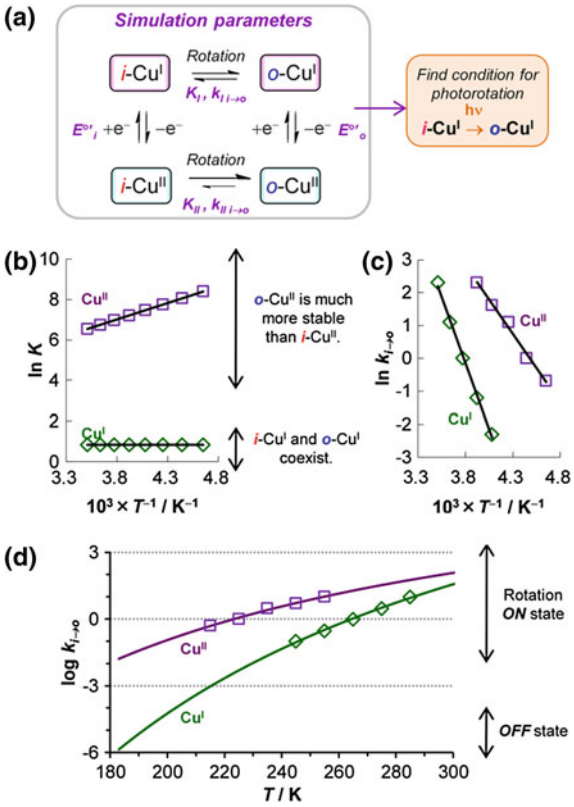

Fig. 4.10 The thermodynamics and kinetics for rotational equilibrium in 0.1 M Bu_4NBF_4–CH_2Cl_2 in the *dark*. **a** Illustration for an aim of the simulation analysis based on the square scheme comprising the redox reaction (*vertical*) and the pyrimidine ring rotation (*horizontal*). **b** The van't Hoff plots for $K_I = [o\text{-}Cu^I]/[i\text{-}Cu^I]$ (*green dots*) and $K_{II} = [o\text{-}Cu^{II}]/[i\text{-}Cu^{II}]$ (*purple dots*). **c** The Arrhenius plots for the $k_{Ii\to o}$ ($i\text{-}Cu^I \rightarrow o\text{-}Cu^I$, *green dots*) and $k_{IIi\to o}$ ($i\text{-}Cu^{II} \rightarrow o\text{-}Cu^{II}$, *purple dots*). **d** The logarithm of $k_{Ii\to o}$ (*green dots*) and $k_{IIi\to o}$ (*purple dots*) as a function of temperature, estimated from the Arrhenius plots. Values determined from a simulated fit to the experimental cyclic voltammograms are shown as dots. Regression curves of the Arrhenius plots are indicated by lines

4.5 Thermodynamics and Kinetics for the Rotation

Since the strategy for PET-driven rotation is based on the light-induced switching between equilibrium and metastable states, detail analysis of thermodynamic and kinetic analysis using square scheme is important (Fig. 4.10a).

The equilibrium constant for the rotation in the copper(I) state ($K_I = [o\text{-}Cu^I]/[i\text{-}Cu^I]$) remained 2.3 (same as $i\text{-}Cu^I/o\text{-}Cu^I = 30{:}70$) over the temperature range 200–300 K (Fig. 4.10b). This result indicates that the two isomers were comparably stable. In contrast, a much larger equilibrium constant in the oxidized

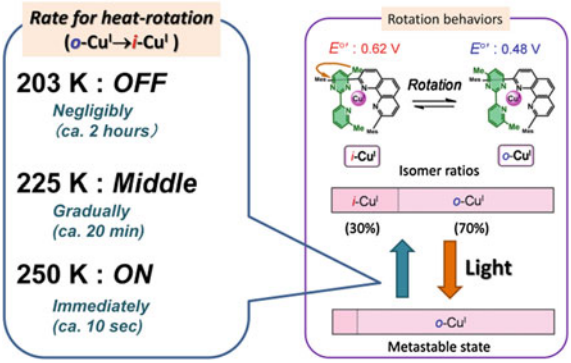

Fig. 4.11 Conceptual diagram showing summary for thermodynamics and kinetics for the rotation in 0.1 M Bu_4NBF_4–CH_2Cl_2, described in this chapter

(copper(II)) state ($K_{II} = [o\text{-}Cu^{II}]/[i\text{-}Cu^{II}]$), obtained from the electrochemical analysis, indicates that nearly all molecules were present as the *o*-isomer under equilibrium, when the system is oxidized from initial copper(I) state (Fig. 4.10b).

The rate constant for the $i\text{-}Cu^{I} \rightarrow o\text{-}Cu^{I}$ rotation estimated from the Arrhenius plots ($k_{Ii\rightarrow o}$), was less than 10^{-4} s^{-1} at 203 K, which indicates that the rotational motion was substantially frozen, which I call the "*OFF* state" (Fig. 4.10c, d). When the temperature was raised to 250 K, $k_{Ii\rightarrow o}$ increased to 10^{-1} s^{-1}, indicating that the rotation was sufficiently activated from *OFF* to *ON* in the copper(I) state. At the intermediate temperature of 225 K, $k_{Ii\rightarrow o}$ was 10^{-3} s^{-1}, implying that the rotation proceeded slowly over a period of several minutes, which enabled me to trace the time progression of the rotational conversion. In contrast, the rate constant for the $i\text{-}Cu^{II} \rightarrow o\text{-}Cu^{II}$ rotation ($k_{IIi\rightarrow o}$) was 10^{-1} s^{-1}, even at 203 K, indicating that the rotation was active on the time scale of 1 min (*ON* state) (Fig. 4.10c, d). The activation energies, E_a, for $i\text{-}Cu^{I} \rightarrow o\text{-}Cu^{I}$ and $i\text{-}Cu^{II} \rightarrow o\text{-}Cu^{II}$, estimated from the slope of the Arrhenius plots, are 67 and 35 kJ mol^{-1}, respectively.

These results suggest that I can thermally capture a metastable copper(I) state out of the *i*-/*o*- equilibrium at 203 K, if light converts a coordination isomer into another form (Fig. 4.11). The value of inverse of $k_{Ii\rightarrow o}$ ($k_{Ii\rightarrow o}^{-1}$) reflects the time for trapping this metastable state. For example, at 203 K, it takes ca. 2 h (10^4 s), and the heat-driven rotation is frozen. At 250 K, it takes only 10 s and the rotation is active. Also, the metastable state can be reset to its initial state by heating to 250 K, at which thermal rotation proceeds to the equilibrium state within several seconds. The unique heat-induced *ON*–*OFF* switching of the rotation process in the copper(I) state is a key phenomenon for photoinduction of our rotational system.

As described above, the rate constant from $i\text{-}Cu^{I}$ to $o\text{-}Cu^{I}$ qualitatively reflects the restoring time from light-induced metastable state into initial state. Next, I describe the quantitative explanation of the heat-driven rotation.

The isomer ratio of *o*-Cu^I and *i*-Cu^I is denoted as follows.

$$\left[o\text{-}Cu^I\right] = x \tag{4.1}$$

$$\left[i\text{-}Cu^I\right] = 1 - x \tag{4.2}$$

The light and heat stimuli induce the isomer ratio change as follows: (i) $x = 0.70$ (initial isomer ratio of *o*-Cu^I), (ii) $x = 0.88$ (metastable state after light irradiation). The chemical equilibrium between *o*-Cu^I and *i*-Cu^I can be represented as following equations.

$$o\text{-}Cu^I \rightarrow i\text{-}Cu^I(k_{Io\rightarrow i}) \tag{4.3}$$

$$i\text{-}Cu^I \rightarrow o\text{-}Cu^I(k_{Ii\rightarrow o}) \tag{4.4}$$

Therefore, the reaction rate can be estimated from rate constants.

$$d\left[o\text{-}Cu^I\right]/dt = -k_{Io\rightarrow i}\left[o\text{-}Cu^I\right] + k_{Ii\rightarrow o}\left[i\text{-}Cu^I\right] \tag{4.5}$$

$$d\left[i\text{-}Cu^I\right]/dt = k_{Io\rightarrow i}\left[o\text{-}Cu^I\right] - k_{Ii\rightarrow o}\left[i\text{-}Cu^I\right] \tag{4.6}$$

Therefore,

$$dx/dt = -(k_{Ii\rightarrow o} + k_{Io\rightarrow i})x + k_{Ii\rightarrow o} \tag{4.7}$$

The differential equation can be solved.

$$x = \left(x_{t=0} + \frac{k_{Ii\rightarrow o}}{k_{Ii\rightarrow o} + k_{Io\rightarrow i}}\right)\exp(-(k_{Ii\rightarrow o} + k_{Io\rightarrow i})t) + \frac{k_{Ii\rightarrow o}}{k_{Ii\rightarrow o} + k_{Io\rightarrow i}} \tag{4.8}$$

The values of $k_{I\ o\rightarrow i}$ and $k_{I\ i\rightarrow o}$ at valuable temperature can be determined from Arrhenius plots, shown in Sect. 4.5. The isomer ratio changes from light-induced metastable state into the initial state, which are caused by heat-driven rotation from *o*-Cu^I to *i*-Cu^I during several minutes, are negligible at 200 K (Fig. 4.12a), gradual at 225 K (Fig. 4.12b), and immediately at 250 K (Fig. 4.12c).

The rotational behavior in acetone was also very similar to that in dichloromethane (Figs. 4.13 and 4.14, and Table 4.3).

4.6 Photophysical Properties

To fuel the rotational isomerization of $3{\cdot}BF_4$ by light illumination, I examined the absorption and luminescence spectra of $3{\cdot}BF_4$. The absorption spectrum of $3{\cdot}BF_4$ in CH_2Cl_2 at room temperature is shown in Fig. 4.15a. Absorption bands in the UV ($\lambda_{max} = 276$ nm) and the visible region ($\lambda_{max} = 456$ nm, $\varepsilon = 4.8 \times 10^3$ M^{-1} cm^{-1}) were attributed to transitions from the ground state to the π-π^* and to the singlet MLCT excited state, respectively, which appear generally in the

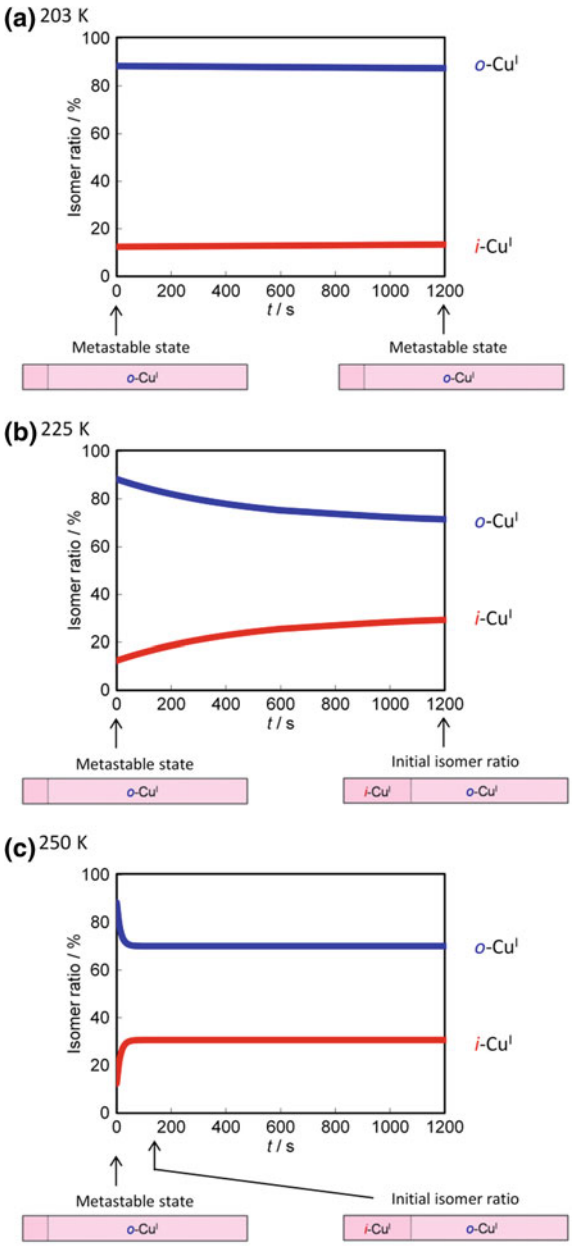

Fig. 4.12 The time profile of the amount of each species after light irradiation at 203 K (**a**), 225 K (**b**), and 250 K (**c**) in 0.1 M Bu_4NBF_4–CH_2Cl_2 in the *dark*. Parameters for rotational equilibrium in Table 4.2 were used

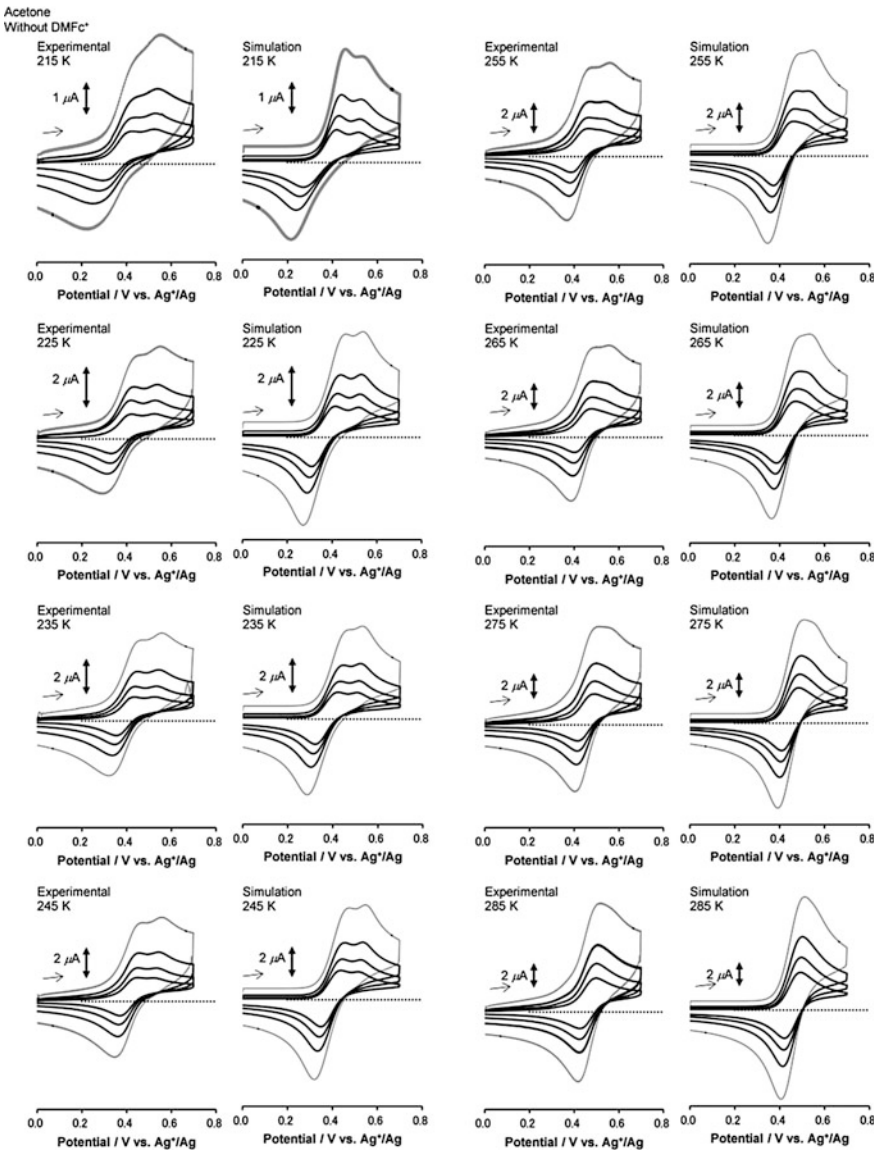

Fig. 4.13 Experimental and simulated cyclic voltammograms of $3{\cdot}BF_4$ (0.45 mM) at several temperatures in 0.1 M Bu_4NBF_4-acetone in the *dark* at the scan rate of 250, 100, 50, and 25 mV s^{-1}

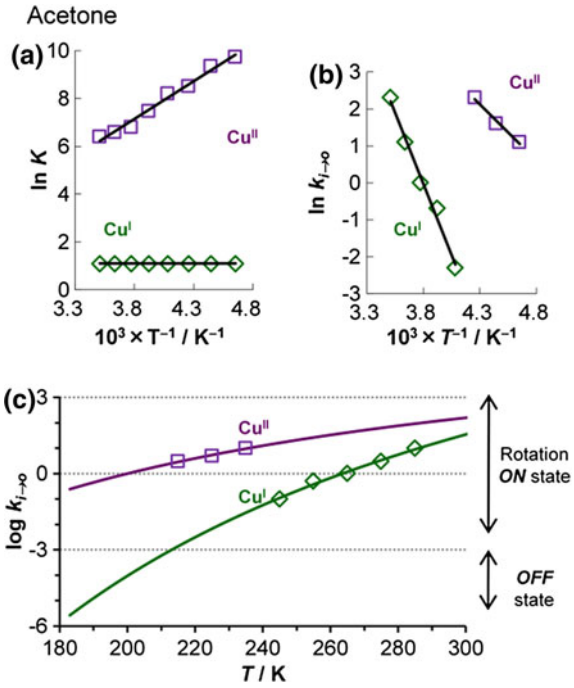

Fig. 4.14 The thermodynamics and kinetics for rotational equilibrium in 0.1 M Bu_4NBF_4-acetone in the *dark*. **a** The van't Hoff plots for $K_I = [o\text{-}Cu^I]/[i\text{-}Cu^I]$ (*green dots*) and $K_{II} = [o\text{-}Cu^{II}]/[i\text{-}Cu^{II}]$ (*purple dots*). **b** The Arrhenius plots for the $k_{Ii\rightarrow o}$ ($i\text{-}Cu^I \rightarrow o\text{-}Cu^I$, *green dots*) and $k_{IIi\rightarrow o}$ ($i\text{-}Cu^{II} \rightarrow o\text{-}Cu^{II}$, *purple dots*). **c** The logarithm of $k_{Ii\rightarrow o}$ (*green dots*) and $k_{IIi\rightarrow o}$ (*purple dots*) as a function of temperature, estimated from the Arrhenius plots. Values determined from a simulated fit to the experimental cyclic voltammograms are shown as dots. Regression curves of the Arrhenius plots are indicated by lines

bis(diimine)copper(I) complex family. The absorption spectra of $3{\cdot}BF_4$ in acetone at both 293 K and 193 K were similar to those in dichloromethane.*

The difference between the absorption spectra of $o\text{-}Cu^I$ and $i\text{-}Cu^I$ was examined, on the basis of spectral changes upon chemical oxidation of $3{\cdot}BF_4$, as follows. The absorption spectral changes of $3{\cdot}BF_4$ upon addition of 0, 0.14, 0.29, 0.43, 0.57, 0.71, 0.86, and 1.0 equiv $(NH_4)_2[Ce(NO_3)_6]$ (ammonium hexanitratocerate (IV)) [26] in acetone at 193 K are shown in Fig. 4.15b. The redox potential of cerium(IV)/(III) in water is known to be 1.36 V versus $DMFc^{+/0}$ in CH_2Cl_2, which is enough positive to oxidize the copper(I) complexes [26]. The oxidation diminished the MLCT absorption band of copper(I) complexes and increased a weak *d–d* transition band of copper(II) complexes [19]. The oxidation reaction of $i\text{-}Cu^I$ and $o\text{-}Cu^I$ (with the ratio, 30:70) proceeded almost independently, because the rotation was frozen at 193 K. As $o\text{-}Cu^I$ is oxidized more easily than $i\text{-}Cu^I$, the early (from 0 to 0.7 equiv) and later (from 0.7 to 1.0 equiv) spectral changes qualitatively show absorption changes of $o\text{-}Cu^I$ and $i\text{-}Cu^I$ upon oxidation,

Table 4.3 Selected parameters obtained from the simulated cyclic voltammograms of $3{\cdot}BF_4$ at the scan rate of 250, 100, 50, and 25 mV s^{-1} in 0.1 M Bu_4NBF_4-acetone

Temperature/K	285	275	265	255	245	235	225	215
$E^{\circ\prime}{}_o$/V[a]	0.45	0.44	0.42	0.41	0.39	0.37	0.36	0.35
$E^{\circ\prime}{}_i$/V[b]	0.58	0.57	0.55	0.55	0.54	0.52	0.52	0.51
K_I[c]	3	3	3	3	3	3	3	3
K_{II}[d]	597	724	891	1754	3653	4943	11510	16,890
k_{ETi}/cm^{-1}[e]	0.2	0.1	0.05	0.03	0.02	0.01	0.008	0.003
k_{ETo}/cm^{-1}[e]	0.02	0.01	0.005	0.003	0.002	0.001	0.0008	0.0003
$k_{Ii\rightarrow o}$/s^{-1}[f]	10	3	1	0.5	0.1	<0.1	<0.1	<0.1
$k_{IIi\rightarrow o}$/s^{-1}[g]	>10	>10	>10	>10	>10	10	5	3
α[h]	0.5	0.5	0.5	0.5	0.5	0.5	0.5	0.5
R_u/W[i]	1000	1000	1000	1000	1000	1000	1000	1000
C_{dl} μF[j]	3×10^{-6}	3×10^{-6}	3×10^{-6}	3×10^{-6}	3×10^{-6}	3×10^{-6}	3×10^{-6}	3×10^{-6}
D/cm^2 s^{-1}[k]	5.5×10^{-6}	4.5×10^{-6}	4.0×10^{-6}	3.5×10^{-6}	3.0×10^{-6}	2.5×10^{-6}	2.0×10^{-6}	1.5×10^{-6}

[a] Redox potential for *o*-$Cu^{II/I}$, versus Ag^+/Ag
[b] Redox potential for *i*-$Cu^{II/I}$, versus Ag^+/Ag
[c] Equilibrium constant, set as [*o*-Cu^I]/[*i*-Cu^I]
[d] Equilibrium constant, set as [*o*-Cu^{II}]/[*i*-Cu^{II}]
[e] Rate constant for the electron transfer
[f] Rate constant for the *i*-Cu^I → *o*-Cu^I rotation
[g] Rate constant for the *i*-Cu^{II} → *o*-Cu^{II} rotation
[h] Transfer coefficient
[i] Resistance
[j] Capacitance
[k] Diffusion coefficient for all species

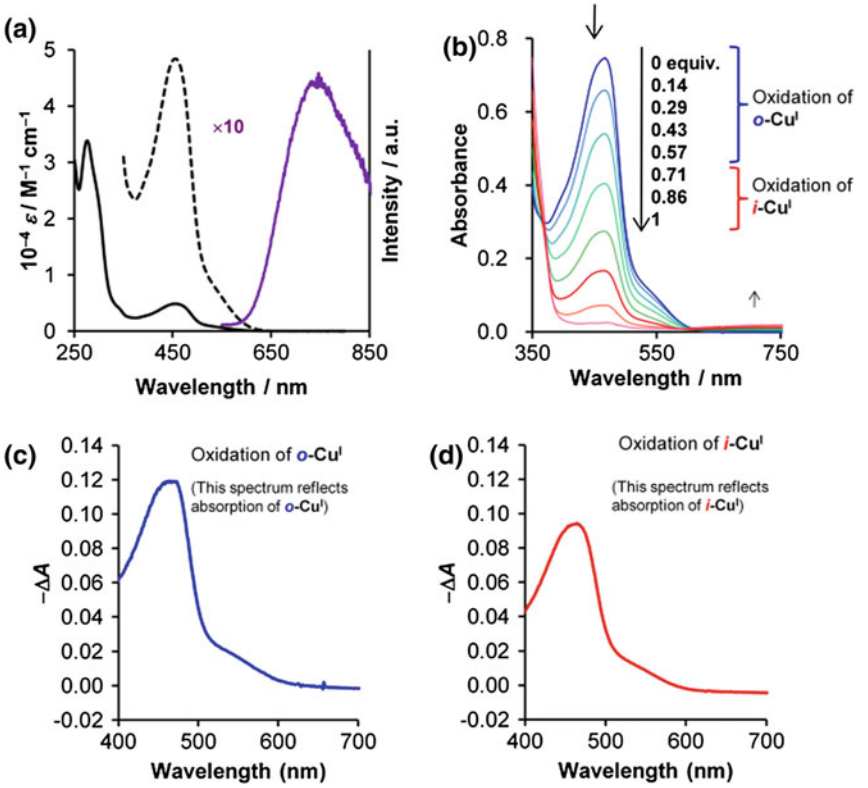

Fig. 4.15 **a** UV–vis spectra of 3·BF_4 in CH_2Cl_2 at room temperature: absorption spectrum in the *dark* (*black*); absorption spectrum in the *dark*, × 10 (*dashed black*); emission spectrum (*purple*). **b** Absorption spectra of 3·BF_4 in the *dark* upon addition of 0, 0.14, 0.29, 0.43, 0.57, 0.71, 0.86, and 1.0 equiv. of $(NH_4)_2[Ce(NO_3)_6]$ in acetone at 193 K. (**c**, **d**) Differences in absorption spectra of 3·BF_4 in acetone at 193 K in the *dark* upon oxidation with $(NH_4)_2[Ce(NO_3)_6]$ between 0.14 equiv. and 0.29 equiv. **c**, and between 0.71 equiv. and 0.86 equiv. (**d**)

respectively. The changes in the region from 400 to 500 nm reflect the absorption of *o*-Cu^I and *i*-Cu^I, as MLCT absorption is much more intense than that of the *d–d* transition of copper(II) complexes.

Figure 4.15c, d display the differences in absorption spectra upon oxidation in the early (0.14 → 0.29 equiv, where only *o*-Cu^I is oxidized, $\lambda_{max} = 466$ nm) and later (0.71 → 0.86 equiv, where only *i*-Cu^I is oxidized, $\lambda_{max} = 465$ nm) spectral changes, respectively. As the absorption change is constant during the addition of $(NH_4)_2[Ce(NO_3)_6]$, the difference in absorption between *o*-Cu^I and *i*-Cu^I would be very small. The small absorption difference is similar to that in our previous rotational system, based on $[Cu(Mepypm)(L_{Anth})]BF_4$ [15]. It should be noted that introducing methyl substituents into ligands of a bis(diimine)copper(I) family slightly affects their absorption spectra, within several nanometers of the

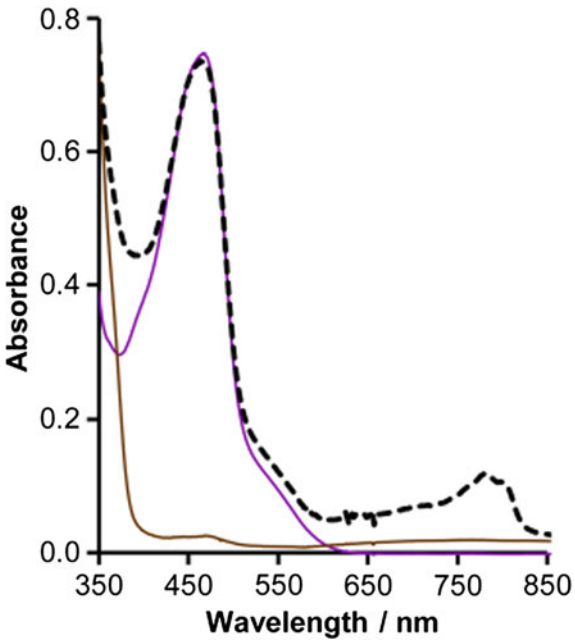

Fig. 4.16 Absorption spectra of $3{\cdot}BF_4$ in acetone at 193 K in the *dark* (*green line*), after adding 1.0 equiv $(NH_4)_2[Ce(NO_3)_6]$ into the solution (*brown line*), and after adding 1.0 equiv $DMFc^0$ into the oxidized solution (*black dotted line*)

maximum absorption change [27, 28]. The absorption spectra of the solutions were reversed by chemical reduction using decamethylferrocene ($DMFc^0$), suggesting that oxidation of $3{\cdot}BF_4$ proceeds without the subsequent chemical degradation (Fig. 4.16).

Definition of photochromism is a reversible transformation of a chemical species induced in one or both directions by absorption of electromagnetic radiation between two forms, A and B, having different absorption spectra [29]. As described in later sections, *i*-Cu^I and *o*-Cu^I are photo- and heat-switchable. Therefore, photoresponsivity without significant color change, described in this chapter, provides a further methodology to construct photodriven materials (Fig. 4.17).

The redox potential of the excited state of $3{\cdot}BF_4$, which is important for constructing a strategy for photodriven *i*-$Cu^I \rightarrow$ *o*-Cu^I rotation, can be estimated using its luminescence spectra. The redox potential in the excited state was estimated according to well-established method [30]. A broad emission band from $3{\cdot}BF_4$ in CH_2Cl_2 was observed in the red region ($\lambda_{max} = 750$ nm) (Fig. 4.15a). It should be noted that this emission band may have arisen predominantly from the *i*-isomer, as the steric hindrance among substituents around the copper(I) center significantly increases the emission efficiency [1, 19].

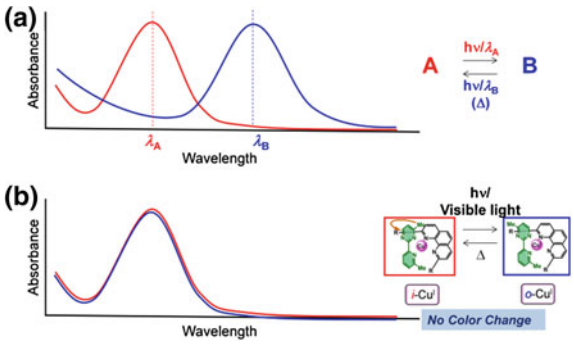

Fig. 4.17 Conceptual diagram showing photoresponsivity using (**a**) photochromic molecule and (**b**) photo- and heat-driven rotation, described in this chapter

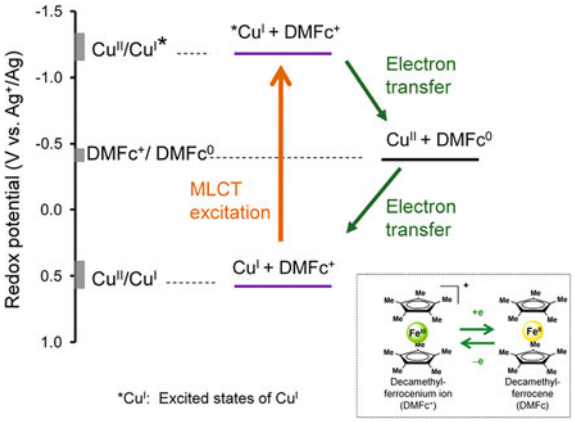

Fig. 4.18 Energy diagram for estimation of redox potential of photoexcited state of $3{\cdot}BF_4$

The energy difference between the ground and excited states was estimated at ca. 1.6 eV from the maxima of the emission spectra (Fig. 4.18) [30]. The redox potential of the ground state of i-$Cu^{II/I}$ was 0.62 V versus Ag^+/Ag at 203 K; thus, the redox potential of the excited i-Cu^I state (i-Cu^{II}/i-Cu^{I}*) was ca. −1.0 V, sufficient for oxidation by the decamethylferrocenium ion ($DMFc^+$) with a reduction potential of −0.4 V at 203 K. The transiently formed copper(II) complex would be expected to return to the copper(I) state by the subsequent back electron transfer process. The copper(II)/(I) redox potential values for both the i- and o-isomers (0.62 V and 0.48 V vs. Ag^+/Ag at 203 K) were sufficiently positive to reoxidize $DMFc^0$ (−0.4 V vs. Ag^+/Ag at 203 K). This estimation was also supported by the fact that similar copper(I) complexes bearing diimines undergo PET fairly efficiently,[19] and $DMFc^{+/0}$ works as an excellent redox mediator [31].

4.7 Photodriven and Heat-Driven Rotation with Redox Mediator

4.7.1 Results

First, I summarize data in Bu_4NBF_4–CH_2Cl_2, described in Sects. 4.2–4.6. (I) Ratio in initial state under equilibrium: *i*-Cu^I:*o*-Cu^I = 30:70 from 200 to 300 K. (II) Rate in initial state: rate constant for *i*-Cu^I → *o*-Cu^I is frozen at 203 K ($k_{Ii\rightarrow o} = 10^{-4}$ s^{-1}) but active at 250 K ($k_{Ii\rightarrow o} = 10^{-1}$ s^{-1}). (III) Redox potentials: copper(II/I) redox potentials between two isomers are different ($\Delta E^{\circ\prime} = 0.14$ V, $E^{\circ\prime}$for *i*-$Cu^{II/I} = 0.62$ V, $E^{\circ\prime}$for *o*-$Cu^{II/I} = 0.48$ V versus Ag^+/Ag at 203 K). (IV) The ratio in the oxidized state under equilibrium: *o*-Cu^{II} is much more stable than *i*-Cu^{II}. (V) Rate in the oxidized state: *i*-Cu^{II} → *o*-Cu^{II} is active from 200 to 300 K ($k_{Ii\rightarrow o} > 10^{-1}$ s^{-1}).

The above results provide a basis for controlling a photoinduced rotation. The PET process is likely to form a tentative copper(II) state, which can make a bypass from *i*-Cu^I to *o*-Cu^I, as the activation energy for rotation in copper(II) is less than that in copper(I). In addition, DMFc can be a potential electron acceptor to complete the PET scheme.

The voltammograms of 3·BF_4 in Bu_4NBF_4–CH_2Cl_2 at several temperatures in the dark were not altered by addition of 4 equiv DMFc·BF_4, suggesting that $DMFc^+$ does not disturb thermal rotational dynamics (Fig. 4.19). Since $DMFc^+$ does not oxidize 3·BF_4 considering their redox potentials, the ratio of rotational isomers, *i*-Cu^I:*o*-Cu^I:*i*-Cu^{II}:*o*-Cu^{II}, is 30:70:0:0. For clarity, I hereafter describe only the rotational isomer ratio *i*-Cu^I:*o*-Cu^I.

In the presence of 4 equiv of DMFc·BF_4 (1.8 mM), the cyclic voltammogram of a solution containing 3·BF_4 (0.45 mM) was significantly altered upon photoirradiation in Bu_4NBF_4–CH_2Cl_2. The experimental procedures and results of this $DMFc^+$ system are summarized in Fig. 4.20. Prior to photoirradiation (Fig. 4.20a, purple lines), two redox waves, one each for *i*-$Cu^{II/I}$ and *o*-$Cu^{II/I}$ in a ratio of 30:70, were observed. The peak currents of the waves reflect the isomer ratio (*i*-Cu^I:*o*-Cu^I = 30:70). The shape of the voltammograms remained constant in the dark, demonstrating that there were no ongoing processes in the absence of photoirradiation (Fig. 4.22a). At 60 min, with photoirradiation with visible light ($\lambda > 400$ nm) at 203 K, the redox waves gradually converged to a wave corresponding to *o*-$Cu^{II/I}$ (Fig. 4.20b). The ratio of *i*-Cu^I to *o*-Cu^I in this metastable state is *i*-Cu^I:*o*-Cu^I = 12:88, estimated from a simulated model fit to the cyclic voltammograms (Fig. 4.21b). The shapes of the voltammograms after photoirradiation did not change with incubation at 203 K in the dark for 10 min, reflecting the persistence of the irradiated state (Fig. 4.22b). Subsequent heating for 2 min at 250 K in the dark recovered the initial voltammogram (*i*-Cu^I:*o*-Cu^I = 30:70), indicating thermal relaxation of the metastable state (Fig. 4.20c, pink lines). Changes in the differential pulse voltammograms of the solution during the process corresponded to the changes in the cyclic voltammograms (Fig. 4.21d, f).

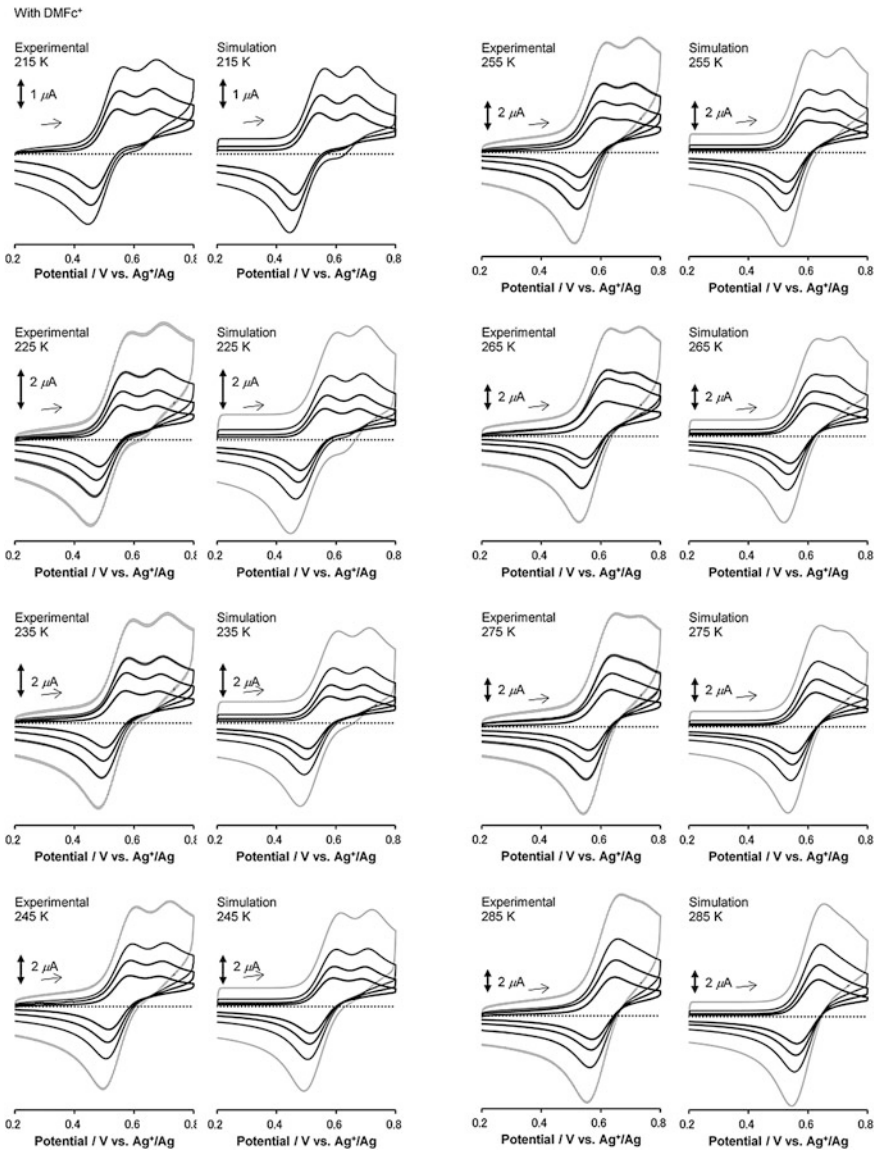

Fig. 4.19 Experimental and simulated cyclic voltammograms of $3{\cdot}BF_4$ (0.45 mM) containing 1.8 mM $DMFc{\cdot}BF_4$ at several temperatures in 0.1 M $Bu_4N{\cdot}BF_4$–CH_2Cl_2 in the *dark* at the scan rate of 250, 100, 50, and 25 mV s^{-1}. Parameters in Table 4.2 were used for simulations

Figure 4.23 displays the changes in the peak current for the *o*-$Cu^{II/I}$ anodic wave in the experimental cyclic voltammograms (Fig. 4.24) upon repeated operations with alternating light irradiation and heating. The process worked repeatedly, demonstrating that the photoinduced isomerization and the redox switching

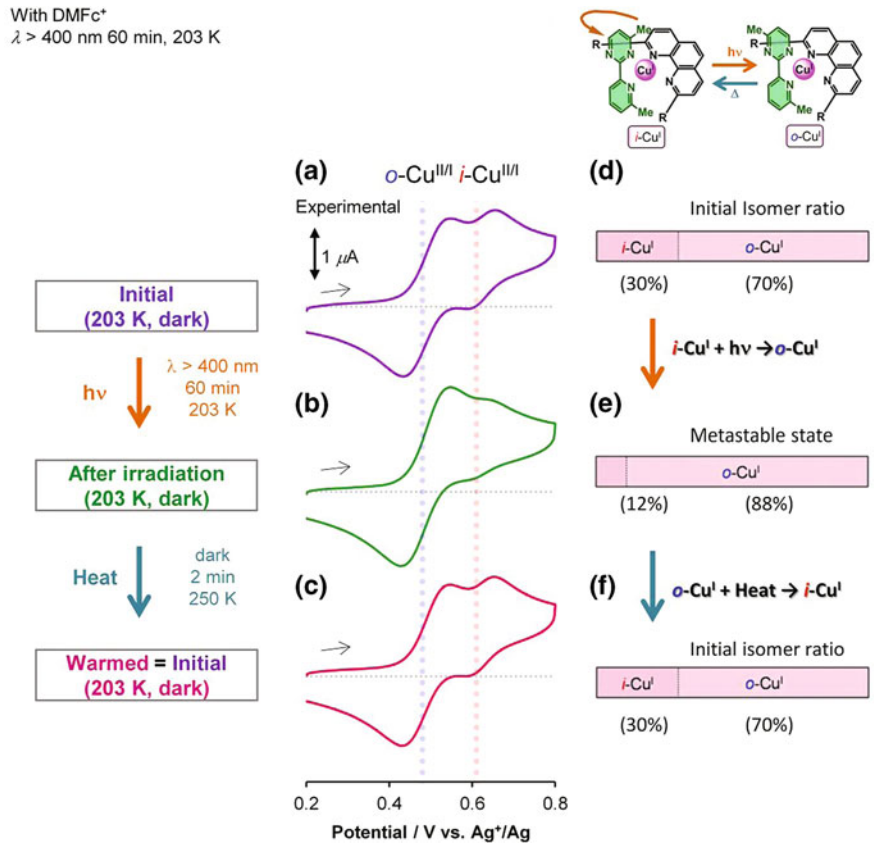

Fig. 4.20 Photorotation experiments in the $DMFc^+$ system with notes about the procedures. Experimental cyclic voltammograms at a scan rate of 50 mV s^{-1}. Investigated $DMFc^+$ systems comprise $3{\cdot}BF_4$ (0.45 mM) in 0.1 M Bu_4NBF_4–CH_2Cl_2 containing 1.8 mM $DMFc{\cdot}BF_4$ at 203 K in the *dark*. **a** initial state (*purple lines*). **b** after 60 min visible light irradiation ($\lambda > 400$ nm) at 203 K (*green lines*). **c** after 2 min heating at 250 K in the *dark* (*pink lines*). (**d**, **e**, **f**) The reversible changes in the molar ratios of the isomers upon light irradiation and heating

were reversible. These results clearly demonstrate a reversible change in the molar ratios of isomers based on photo- and heat-driven rotational isomerization.

The convergence of redox waves at 203 K in the $DMFc^+$ system with visible light irradiation was negligible after 5 min, considerable after 20 min, and nearly saturated after 60 min (Table 4.4 and Figs. 4.25, 4.26, 4.27, 4.28). As selective irradiation with blue light ($\lambda = 450 \pm 40$ nm) also induced isomerization from the *i*- to the *o*-isomer, isomerization could have resulted from excitation of the MLCT absorption band (Table 4.4). Because photoisomerization did not occur in the absence of $DMFc^+$, a reaction pathway through PET from copper(I) complexes to the electron acceptor ($DMFc^+$) appeared to be a key step for the *i*- to *o*-conversion (Table 4.4). It should be noted that 20 min of visible light irradiation at

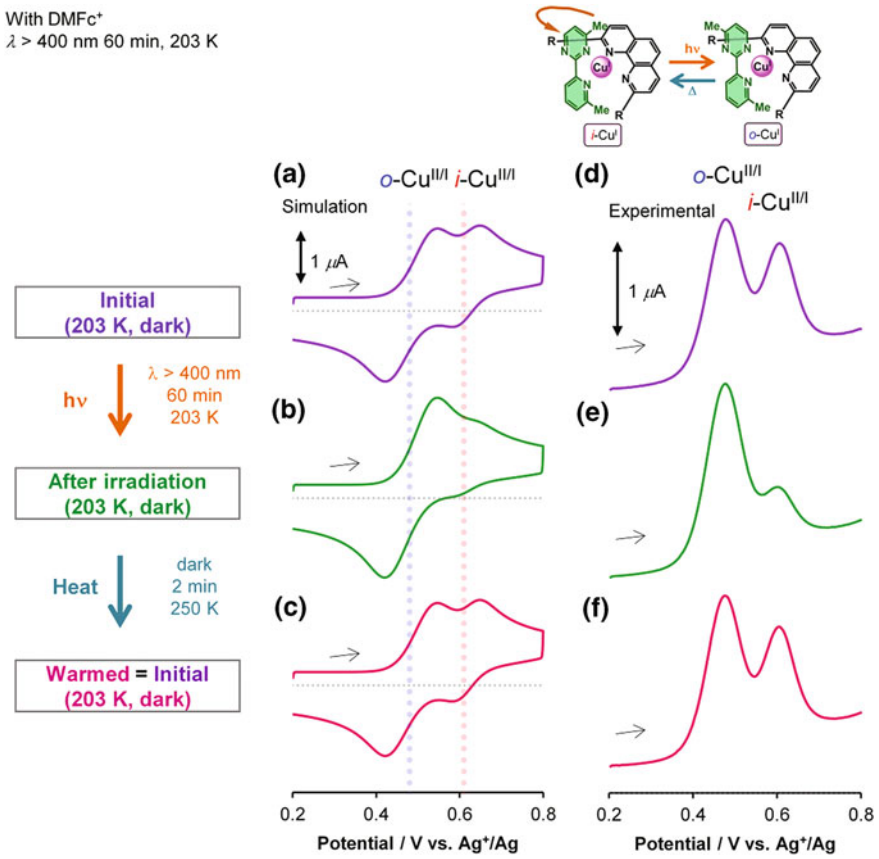

Fig. 4.21 Photorotation experiments in the $DMFc^+$ system under the same condition as Fig. 4.7.2 with notes about the procedures. Simulated cyclic voltammograms at a scan rate of 50 mV s^{-1} (**a**, **b**, **c**) and differential pulse voltammogram (**d**, **e**, **f**). Parameters in Table 4.2 with a modification for initial ratio of *i*-Cu^I and *o*-Cu^I were used for simulation

225 K did not alter the voltammogram (Table 4.4); these results are discussed in the final section.

4.7.2 Mechanism

The schematic representation of PET driven rotation from *i*-Cu^I to *o*-Cu^I in the $DMFc^+$ system (Fig. 4.29) is described as follows.

(i) $i\text{-}Cu^I + h\nu \rightarrow i\text{-}Cu^{I}*$
(ii) $i\text{-}Cu^{I}* + DMFc^+ \rightarrow i\text{-}Cu^{II} + DMFc^0$

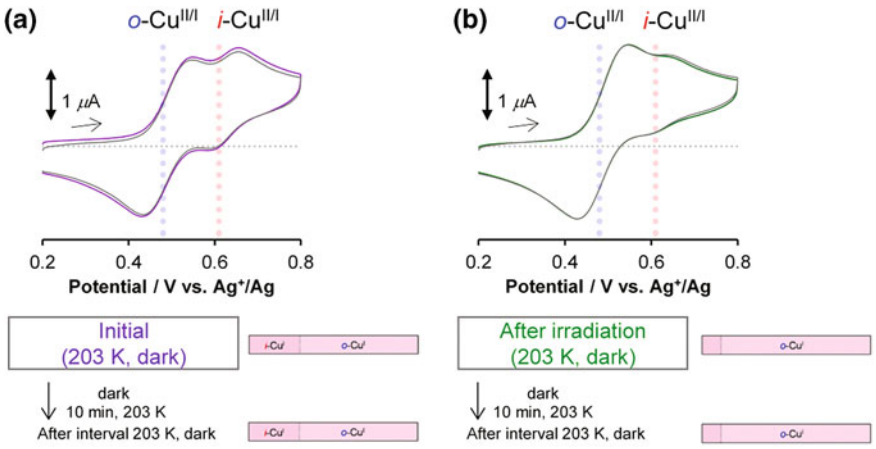

Fig. 4.22 Photorotation experiments in the $DMFc^+$ system with notes about the procedures. Cyclic voltammograms at a scan rate of 50 mV s^{-1} of $3{\cdot}BF_4$ (0.45 mM) in 0.1 M Bu_4NBF_4–CH_2Cl_2 containing 1.8 mM $DMFc{\cdot}BF_4$ at 203 K in the dark. **a**, *purple line*: initial state. **a**, *grey line*: after 10 min interval of the initial state in the dark at 203 K. **b**, *green line*: after 60 min visible light irradiation ($\lambda > 400$ nm) at 203 K. **b**, *grey line*: after 10 min interval of the irradiated state in the dark at 203 K

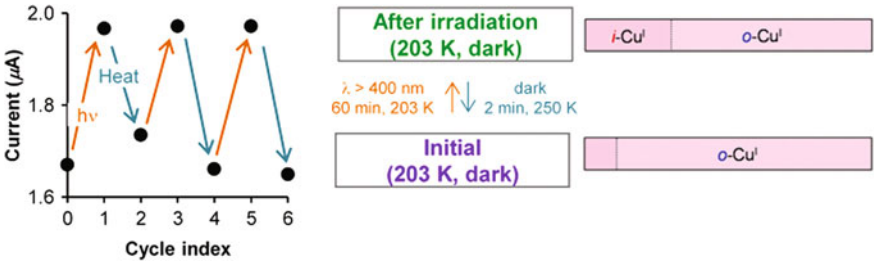

Fig. 4.23 Changes in the anodic peak current at 0.55 V in the experimental cyclic voltammograms of $3{\cdot}BF_4$ (0.45 mM) in 0.1 M Bu_4NBF_4–CH_2Cl_2 containing 1.8 mM $DMFc{\cdot}BF_4$ at 203 K. The voltammograms are shown in Fig. 4.24

(iii) $i\text{-}Cu^{II} \rightarrow o\text{-}Cu^{II}$
(iv) $o\text{-}Cu^{II} + DMFc^0 \rightarrow o\text{-}Cu^{I} + DMFc^+$

The observed photo- and heat-driven isomerization mechanisms can be interpreted in terms of the kinetics of the transition between the preferred ligand geometries of the copper(I) and copper(II) states, obtained from simulation fits to the voltammograms (Sect. 4.5). The two isomers, $i\text{-}Cu^I$ and $o\text{-}Cu^I$, are present in the initial copper(I) state in a ratio of 30:70 ($K_I = [o\text{-}Cu^I]/[i\text{-}Cu^I] = 2.3$). Photoillumination of the solution induces PET from the light excited $i\text{-}Cu^I$ state ($^*i\text{-}Cu^I$) to the redox mediator ($DMFc^+$), as the oxidation potential of $^*i\text{-}Cu^I$ is -1.0 V. The transiently formed $i\text{-}Cu^{II}$ isomerizes to $o\text{-}Cu^{II}$ because of two reasons: (i) the

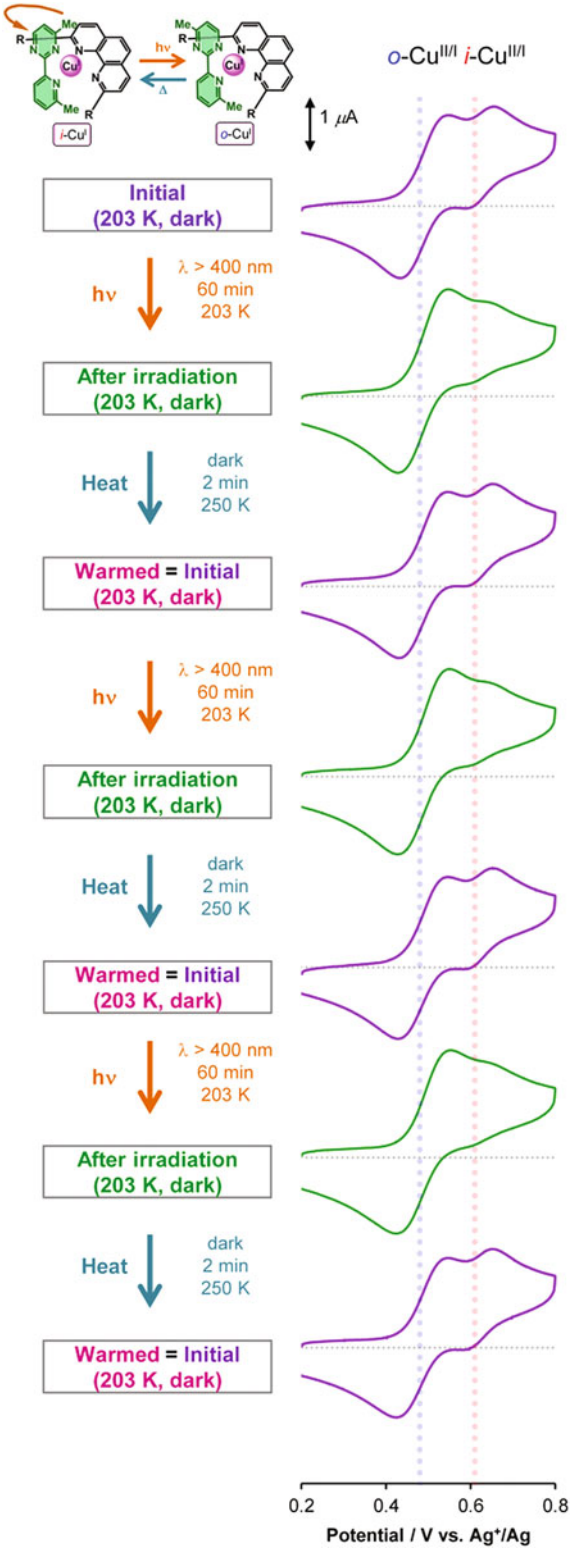
hν
Δ
i-Cu^I
o-Cu^I
o-Cu^II/I
i-Cu^II/I
1 μA
Initial
(203 K, dark)
hν
λ > 400 nm
60 min
203 K
After irradiation
(203 K, dark)
Heat
dark
2 min
250 K
Warmed = Initial
(203 K, dark)
hν
λ > 400 nm
60 min
203 K
After irradiation
(203 K, dark)
Heat
dark
2 min
250 K
Warmed = Initial
(203 K, dark)
hν
λ > 400 nm
60 min
203 K
After irradiation
(203 K, dark)
Heat
dark
2 min
250 K
Warmed = Initial
(203 K, dark)
0.2
0.4
0.6
0.8
Potential / V vs. Ag+/Ag

◀**Fig. 4.24** Photorotation experiments in the $DMFc^+$ system with notes about the procedures. Cyclic voltammograms at a scan rate of 50 mV s^{-1} of $3{\cdot}BF_4$ (0.45 mM) in 0.1 M Bu_4NBF_4–CH_2Cl_2 containing 1.8 mM $DMFc{\cdot}BF_4$ at 203 K in the dark upon repeated operations with the 60 min visible light irradiation ($\lambda > 400$ nm) at 203 K and the 2 min heating at 250 K in the dark

Table 4.4 Photorotation experiments under several conditions using cyclic voltammograms

Entry	t/min[a]	λ/nm[b]	$DMFc^+$/equiv. [c]	T/K[d]	Changes in i-Cu^I:o-Cu^I [e]
1	5	>400	4	203	Negligible
2	20	>400	4	203	30:70 → 15:85
3	60	>400	4	203	30:70 → 12:88
4	60	450 ± 40	4	203	30:70 → 20:80
5	60	>400	0	203	Negligible
6	20	>400	4	225	Negligible

[a] Irradiation time
[b] Irradiation wavelength
[c] Chemical equivalent of $DMFc{\cdot}BF_4$ to total $3{\cdot}BF_4$
[d] Temperature
[e] Changes in i-Cu^I:o-Cu^I upon light irradiation, judging from a simulated model fit to the experimental cyclic voltammograms of $3{\cdot}BF_4$ (0.45 mM) containing 1.8 mM $DMFc{\cdot}BF_4$ in 0.1 M Bu_4NBF_4–CH_2Cl_2 at a scan rate of 50 mV s^{-1} in the *dark* at T K before and after light irradiation. All voltammograms are displayed from Figs. 4.25, 4.26, 4.27, 4.28

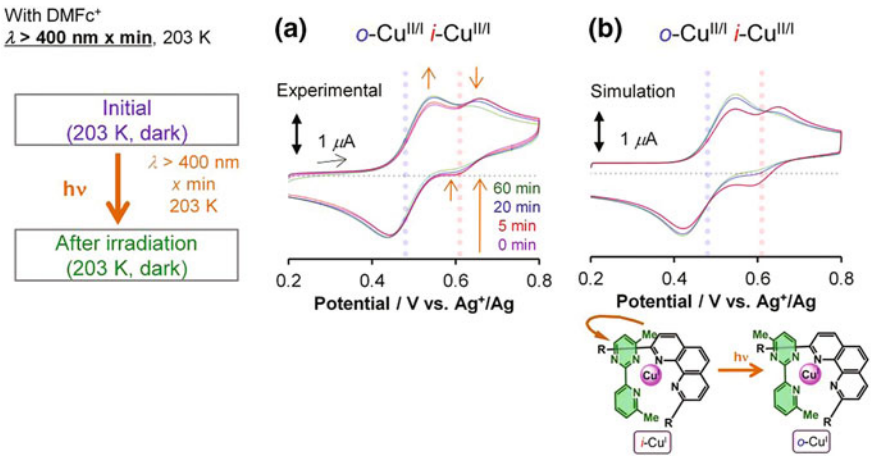

Fig. 4.25 Photorotation experiments in the $DMFc^+$ system with notes about the procedures. Experimental (**a**) and simulated (**b**) cyclic voltammograms at a scan rate of 50 mV s^{-1}. Investigated $DMFc^+$ systems comprise $3{\cdot}BF_4$ (0.45 mM) in 0.1 M $Bu_4N{\cdot}BF_4$–CH_2Cl_2 containing 1.8 mM $DMFc{\cdot}BF_4$ at 203 K in the *dark*. *Purple line*: initial state. *Pink*, *blue*, and *green*: after x min visible light irradiation ($\lambda > 400$ nm) at 203 K, $x = 5$ (*pink*), $x = 20$ (*blue*), and $x = 60$ (*green*)

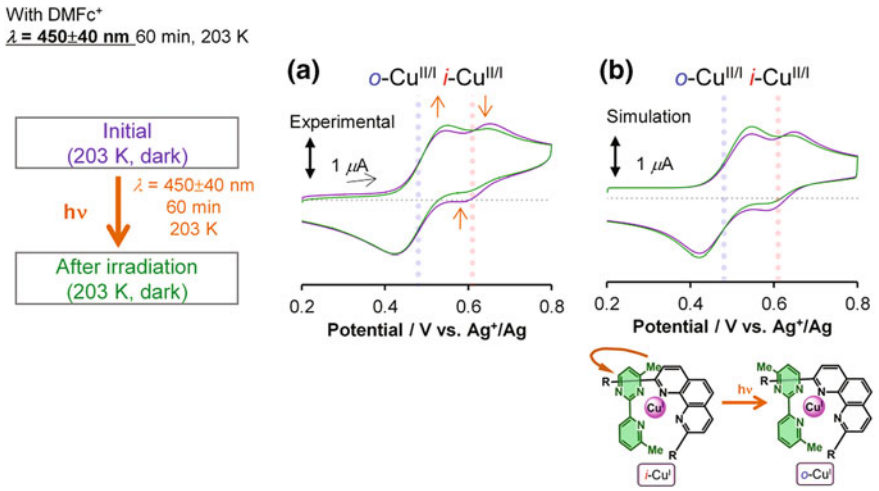

Fig. 4.26 Photorotation experiments in the $DMFc^+$ system with notes about the procedures. Experimental (**a**) and simulateive (**b**) cyclic voltammograms at a scan rate of 50 mV s^{-1}. Investigated $DMFc^+$ systems comprise $3{\cdot}BF_4$ (0.45 mM) in 0.1 M Bu_4NBF_4–CH_2Cl_2 containing 1.8 mM $DMFc{\cdot}BF_4$ at 203 K in the *dark*. *Purple line*: initial state. *Green line*: after 60 min visible light irradiation ($\lambda > 400$ nm) at 203 K

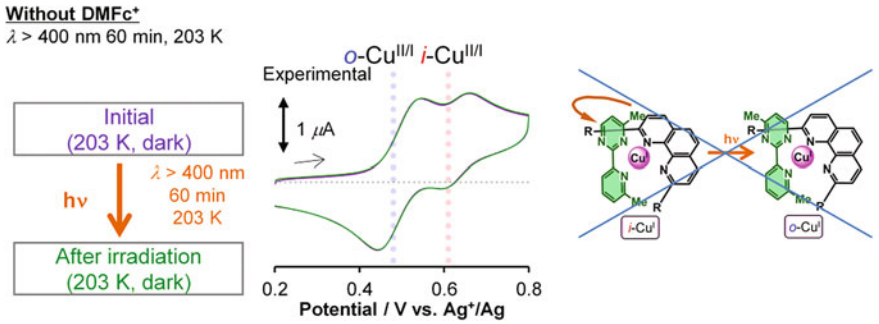

Fig. 4.27 Photorotation experiments in the $DMFc^+$ system with notes about the procedures. Experimental cyclic voltammograms at a scan rate of 50 mV s^{-1}. Investigated $DMFc^+$ systems comprise $3{\cdot}BF_4$ (0.45 mM) in 0.1 M Bu_4NBF_4–CH_2Cl_2 without $DMFc{\cdot}BF_4$ at 203 K in the *dark*. *Purple line*: initial state. *Green line*: after 60 min visible light irradiation ($\lambda > 400$ nm) at 203 K

rotational isomerization within the copper(II) state was active ($k_{\mathrm{II}i\rightarrow o} = 10^{-1}$ s^{-1}, in the *ON* state); and (ii) *i*-Cu^{II} was not thermodynamically preferred as compared with *o*-Cu^{II}, on account of large steric repulsion ($K_{II} = [o\text{-}Cu^{II}]/[i\text{-}Cu^{II}] > 10^2$). Then, the transiently formed *o*-Cu^{II} is reduced to *o*-Cu^{I} through an electron transfer with $DMFc^0$. The net process proceeds through the photoinduced conversion of *i*-Cu^{I} to *o*-Cu^{I}. If the forward conversion rate (from *i*-Cu^{I} to *o*-Cu^{I} by light illumination) is sufficiently faster than the thermally activated reverse rate (from *o*-Cu^{I}

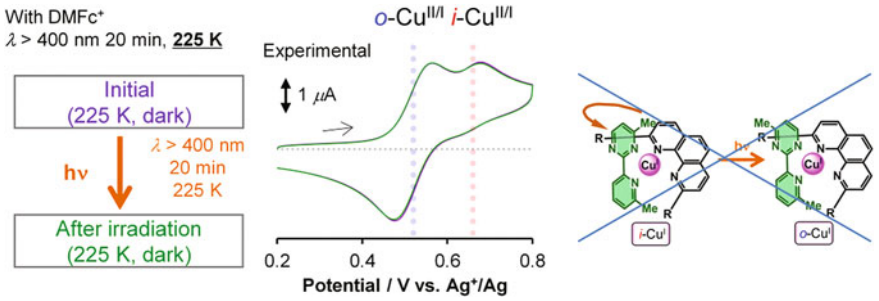

Fig. 4.28 Photorotation experiments in the $DMFc^+$ system with notes about the procedures. Experimental cyclic voltammograms at a scan rate of 50 mV s^{-1}. Investigated $DMFc^+$ systems comprise $3{\cdot}BF_4$ (0.45 mM) in 0.1 M Bu_4NBF_4–CH_2Cl_2 without $DMFc{\cdot}BF_4$ at 225 K in the *dark*. *Purple line*: initial state. *Green line*: after 20 min visible light irradiation ($\lambda > 400$ nm) at 225 K

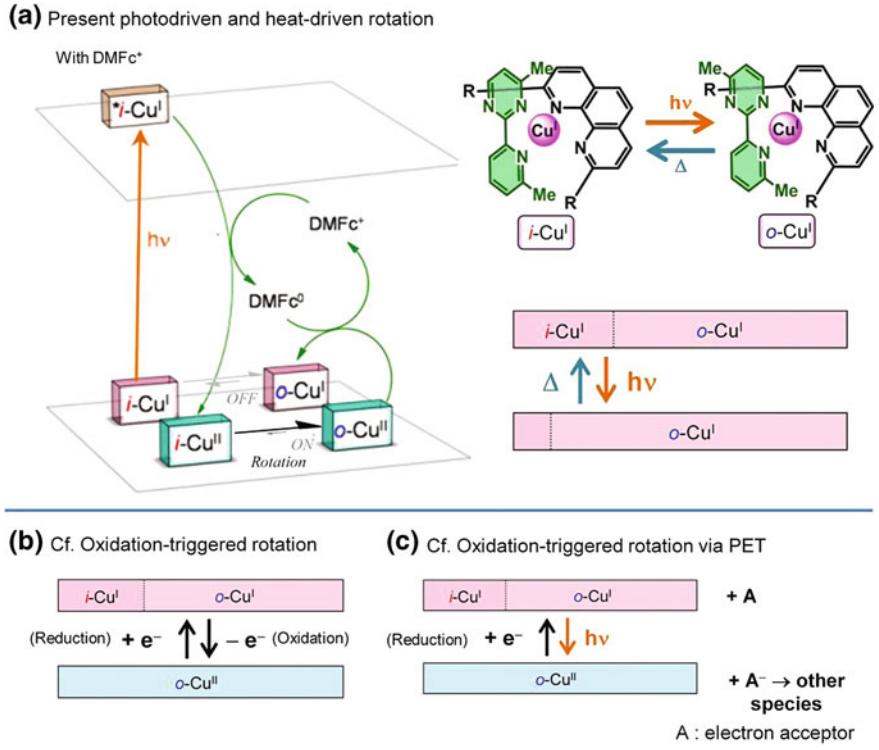

Fig. 4.29 **a** Schematic representation of the PET-driven *i*-Cu^I to *o*-Cu^I ligand geometry isomerization of $3{\cdot}BF_4$ in the presence of $DMFc^+$. The reversible changes in the molar ratios of the isomers upon light irradiation and heating are illustrated in the right panel. **b**, **c** The expected ratio changes in the molar ratio of isomer using well-established oxidation-triggered rotation

to *i*-Cu^{I}, $k_{Io\rightarrow i} = 10^{-4}$ s^{-1} at 203 K, in the *OFF* state), the photodriven *i*-Cu^{I} → *o*-Cu^{I} isomerization proceeds. Therefore, the rate of *i*-Cu^{I} → *o*-Cu^{I} photodriven rotation is greater than 10^{-4} s^{-1} in the $DMFc^{+}$ system at 203 K. The photodriven rotation induces the change in a ratio of *i*-Cu^{I}:*o*-Cu^{I} (in the conditions of Sect. 4.7.1, from 30:70 to 12:88). The reversion from the light-induced metastable state by the thermal process at 203 K would take on the order of 10^{4} s, judging from the rate constant value, $k_{Io\rightarrow i} = 10^{-4}$ s^{-1}. Heating to 250 K ($k_{Io\rightarrow i} = 10^{-1}$ s^{-1}, in the *ON* state) provides sufficient thermal energy to the copper complex that the initial isomer ratio is restored through back-isomerization from *o*-Cu^{I} to *i*-Cu^{I}. Consequently, the results show that the *i*-Cu^{I} → *o*-Cu^{I} rotation via the redox potential shift in the $DMFc^{+}$ system can be driven by light.

It is considered that the several undesired reactions can contribute to a deactivation for the *i*-Cu^{I} → *o*-Cu^{I} photorotation. For example, the back electron transfer process, *i*-Cu^{II} + $DMFc^{0}$ → *i*-Cu^{I} + $DMFc^{+}$, can compete the rotation in the copper(II) state, *i*-Cu^{II} → *o*-Cu^{II}. For another example, both radiative and non-radiative transition of the photo-excited state, **i*-Cu^{I} → *i*-Cu^{I} + hν'or heat, can compete the PET process, **i*-Cu^{I} + $DMFc^{+}$ → *i*-Cu^{II} + $DMFc^{0}$. Energy transfer in the photo-excited states also contributes to the deactivation. One or more of them can be reasons why the *i*-Cu^{I} → *o*-Cu^{I} photorotation is slow, considering that the sufficient light-induced voltammograms changes requires long (60 min) irradiation time in the $DMFc^{+}$ system. However, these deactivation processes are not critical to stop the photo-driven rotation.

I would like to emphasize the remarkable difference between photodriven *i*-Cu^{I} → *o*-Cu^{I} rotation and well-established oxidation-triggered rotation based on supramolecules developed by Sauvage et al. The present pyrimidine system exhibits the well-established oxidation-triggered rotation (*i*-Cu^{I}-e^{-} → *i*-Cu^{II} → *o*-Cu^{II}; Cu^{I} to Cu^{II}), which is similar to Sauvage's system. Additionally, well-established oxidation-triggered rotation via PET (in this system, *i*-Cu^{I} + A + hν → *i*-Cu^{II} + A^{-}, *i*-Cu^{II} → *o*-Cu^{II}, A^{-} → other products; Cu^{I} to Cu^{II}) is also expected to be achieved like Sauvage's system. Adding reductive agents is required to reverse the Cu^{II} state to the Cu^{I} state. The present photodriven *i*-Cu^{I} → *o*-Cu^{I} rotation (Cu^{I} to Cu^{I}), however, is not the oxidation-triggered rotation; both *i*-Cu^{II} and *o*-Cu^{II} are only transient species.

4.8 Photodriven and Heat-Driven Rotation Under Partial Oxidation

I next attempted to construct a combined photodriven-rotation-redox switching system without the need for a redox mediator, to show its high versatility. The mechanism described above predicts that a more efficient repeatable transition is expected if the copper(II) complex itself acts as an electron acceptor ($E^{\circ\prime} = 0.48$ V), in place of the relatively weaker $DMFc^{+}$ state ($E^{\circ\prime} = -0.41$ V) (Fig. 4.30).

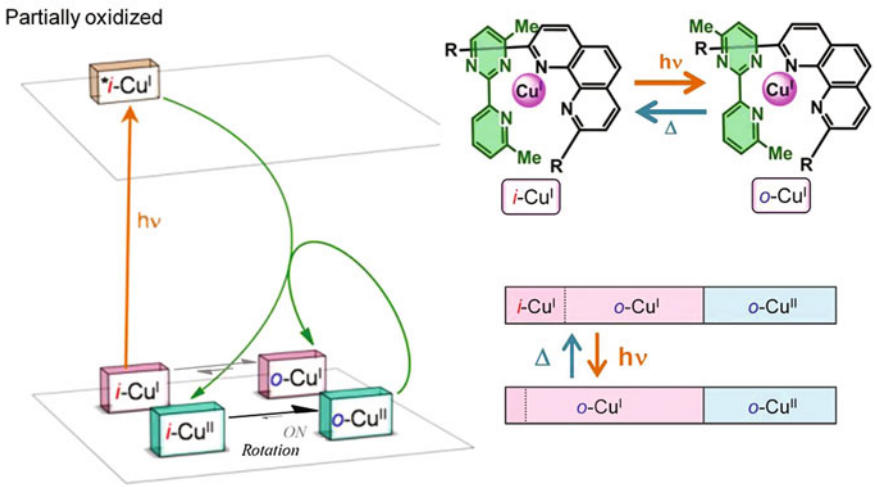

Fig. 4.30 Schematic representation of the PET-driven *i*-Cu^{I} to *o*-Cu^{I} ligand geometry isomerization of the partial oxidation of 3·BF_4 by $(NH_4)_2[Ce(NO_3)_6]$. The reversible changes in the molar ratios of the isomers upon light irradiation and heating are illustrated in the right panels

To test this speculation, 3·BF_4 in Bu_4NBF_4–CH_2Cl_2 was partially oxidized by 0.4 equiv $(NH_4)_2[Ce(NO_3)_6]$. The changes in the partially oxidized system with light illumination and heating were basically similar to those of the $DMFc^+$ system, judging from the anodic waves in the voltammograms.

In this case, the sample contains four components, *i*-Cu^{I}, *o*-Cu^{I}, *i*-Cu^{II}, and *o*-Cu^{II}, as it includes copper(II) species even in the dark condition. The ratio of each component was estimated as follows.

$$1 - a = [o\text{-}Cu^{I}] + [i\text{-}Cu^{I}] \tag{4.9}$$

$$x(1 - a) = [o\text{-}Cu^{I}] \tag{4.10}$$

$$a = [o\text{-}Cu^{II}] + [i\text{-}Cu^{II}] \tag{4.11}$$

$$[o\text{-}Cu^{I}] + [i\text{-}Cu^{I}] + [o\text{-}Cu^{II}] + [i\text{-}Cu^{II}] = 1 \tag{4.12}$$

Here, the total amount of copper(II) species is expressed as *a,* which is identical to an equivalent amount of oxidative agent. The ratio of *o*-Cu^{I} to total copper(I) species is expressed as *x*. Because the rotation in the copper(II) state is always under equilibrium, the molar ratio of *i*-Cu^{II} is negligible, considering its large equilibrium constant ($K_{II} = [o\text{-}Cu^{II}]/[i\text{-}Cu^{II}] > 10^2$). Therefore,

$$a = [o\text{-}Cu^{II}] + [i\text{-}Cu^{II}] \cong [o - Cu^{II}] \tag{4.13}$$

Since $K_I = [o\text{-}Cu^I]/[i\text{-}Cu^I] = 2.3$ remains constant over a temperature range from 203 to 250 K, x in the initial state is

$$x = K_I/(1 + K_I) = 0.7 \tag{4.14}$$

In the case of $a = 0.4$, the molar ratio in the initial state of the partially oxidized system is $i\text{-}Cu^I$:$o\text{-}Cu^I$:$i\text{-}Cu^{II}$:$o\text{-}Cu^{II}$ = 30:70:0:66. For clarity, I describe the rotational isomer ratio only as $i\text{-}Cu^I$:$o\text{-}Cu^I$, considering that the copper(II) state is always under equilibrium and that $i\text{-}Cu^{II}$ can be set to 0. Thus, oxidation of 0.75 mM of $3{\cdot}BF_4$ by 0.4 equiv $(NH_4)_2[Ce(NO_3)_6]$ (0.30 mM) in Bu_4NBF_4–CH_2Cl_2 yields 0.45 mM of $3{\cdot}BF_4$ solution with copper(II) complexes (0.30 mM) as redox mediator.

Cyclic voltammograms of the partially oxidized system noted above showed two anodic waves at 225 K, one each for the *i*- and *o*-isomers, in a ratio of 30:70, whose peak currents reflect the molar ratio ($i\text{-}Cu^I$:$o\text{-}Cu^I$) in the solution (Fig. 4.31a, purple line). No deformation of cyclic voltammograms in the dark occurred, suggesting that the expected self-exchange electron transfer between the copper species induced negligible changes in the $i\text{-}Cu^I$:$o\text{-}Cu^I$ isomer ratio (Fig. 4.32a). The redox waves converged into a single wave corresponding to the *o*-isomer upon 3 min of photoirradiation with visible light ($\lambda > 400$ nm) at 225 K (Fig. 4.31b, green line). It should be noted that present irradiation time (3 min) is much shorter than that for $DMFc^+$ system at 203 K (60 min). The convergence can be qualitatively explained by a change in molar ratio from $i\text{-}Cu^I$:$o\text{-}Cu^I$ = 30:70 to ca. 12:88, since the light-induced changes in the voltammograms resemble those of the $DMFc^+$ system from the viewpoint of anodic waves; simulation of the anodic waves also supported the isomer ratio changes (Fig. 4.33 and Table 4.5). The cyclic voltammograms gradually recovered to the initial state in the dark (Fig. 4.32b), and were restored after a 20 min interval (Fig. 4.31c, purple). Fig. 4.34 displays the changes in anodic peak currents of the *o*-isomer in the voltammograms at 225 K in the partially oxidized system for 10 repeated operations of 3 min light illumination at 225 K and 20 min interval in the dark (experimental voltammograms are displayed in Fig. 4.35). The result shows the excellent repeatability of the photodriven and heatdriven rotation accompanied with redox potential switching.

The PET process of the partially oxidized system can be described as follows (Fig. 4.30).

(i) $i\text{-}Cu^I + h\nu \rightarrow i\text{-}Cu^I{*}$
(ii) $i\text{-}Cu^I{*} + o\text{-}Cu^{II} \rightarrow i\text{-}Cu^{II} + o\text{-}Cu^I$
(iii) $i\text{-}Cu^{II} \rightarrow o\text{-}Cu^{II}$

Photoillumination of $i\text{-}Cu^I$ followed by PET to $o\text{-}Cu^{II}$ yields $i\text{-}Cu^{II}$ and $o\text{-}Cu^I$, leading to a rapid rotational isomerization from $i\text{-}Cu^{II}$ to $o\text{-}Cu^{II}$. The net scheme is $i\text{-}Cu^I$ to $o\text{-}Cu^I$ without back-electron transfer to $o\text{-}Cu^{II}$, unlike in the $DMFc^+$-mediated system. It should be noted that the photodriven rotation proceeds even at 225 K, unlike in the $DMFc^+$ system, and in a very short time frame. The rate

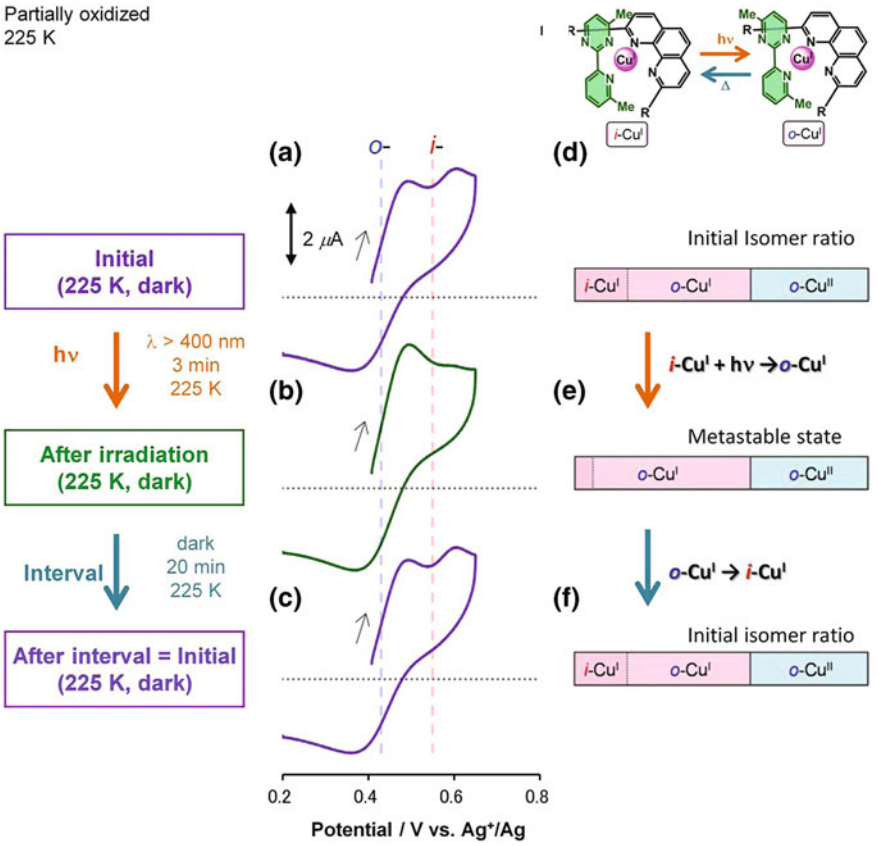

Fig. 4.31 **a**–**c** Experimental cyclic voltammograms at a scan rate of 100 mV s^{-1} of 3·BF_4 (0.75 mM) in Bu_4NBF_4–CH_2Cl_2/acetone (v/v 20:1) upon addition of 0.4 equiv. $(NH_4)_2[Ce(NO_3)_6]$ (0.3 mM) at 225 K in the dark. **a**, (*purple line*): initial state. **b**, (*green line*): after 3 min visible light irradiation ($\lambda > 400$ nm) at 225 K. **c**, (*purple line*): after a 20 min interval at 225 K in the *dark*. The reversible changes in the molar ratios of the isomers upon light irradiation and heating are illustrated in the right panel

constant of *i*-Cu^I → *o*-Cu^I photodriven rotation is larger than 10^{-3} s^{-1} in the partially oxidized system at 225 K, coincident with the competitive thermal back-isomerization process (*o*-Cu^I → *i*-Cu^I), with rate constant $k_{Io \to i} = 10^{-3}$ s^{-1}. The scheme contributes considerably to changes in the isomer ratio, *i*-Cu^I:*o*-Cu^I, from initial to metastable states (in Fig. 4.31, from 30:70 to ca. 12:88). The rate constant of thermal reversion at 225 K is $k_{Io \to i} = 10^{-3}$ s^{-1}, which qualitatively suggests that the metastable state is restored to equilibrium after 10^3 s. The estimation is consistent with the 20 min recovery process displayed in the voltammogram at 225 K. Consequently, partial oxidation turns out to be a powerful way to achieve the conversion of light stimuli to redox potential signals through *i*-Cu^I → *o*-Cu^I photodriven rotation.

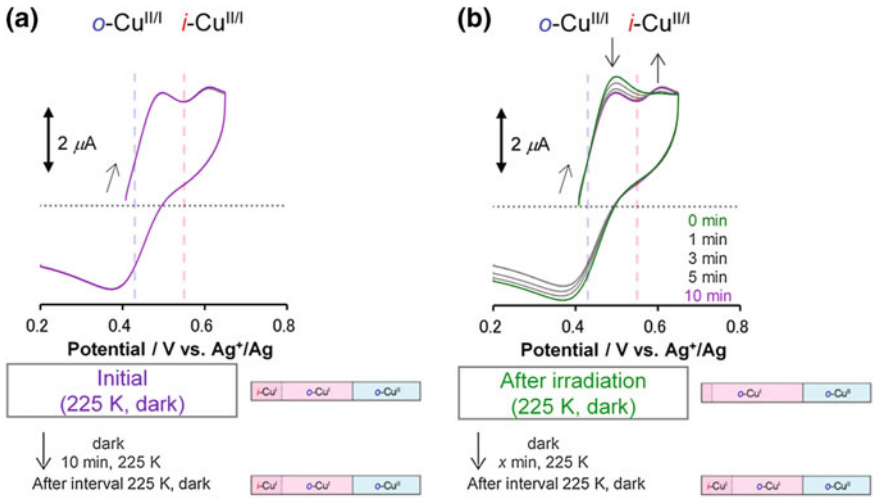

Fig. 4.32 Photorotation experiments in the partially oxidized system with illustrations for procedures. (**a**, **b**) Experimental cyclic voltammograms at a scan rate of 100 mV s^{-1} of 3·BF_4 (0.75 mM) in Bu_4NBF_4–CH_2Cl_2/acetone (v/v 20:1) upon addition of 0.4 equiv. $(NH_4)_2[Ce(NO_3)_6]$ (0.3 mM) at 225 K in the *dark*: the initial state (**a**, *purple line*), after 10 min interval of the initial state in the *dark* at 203 K (**a**, *grey line*), after irradiation state (**b**, *green line*), after 1 (**b**, *grey line*), 3(**b**, *grey line*), 5(**b**, *grey line*), and 10 min (**b**, *purple line*) interval of the irradiated state in the dark at 203 K

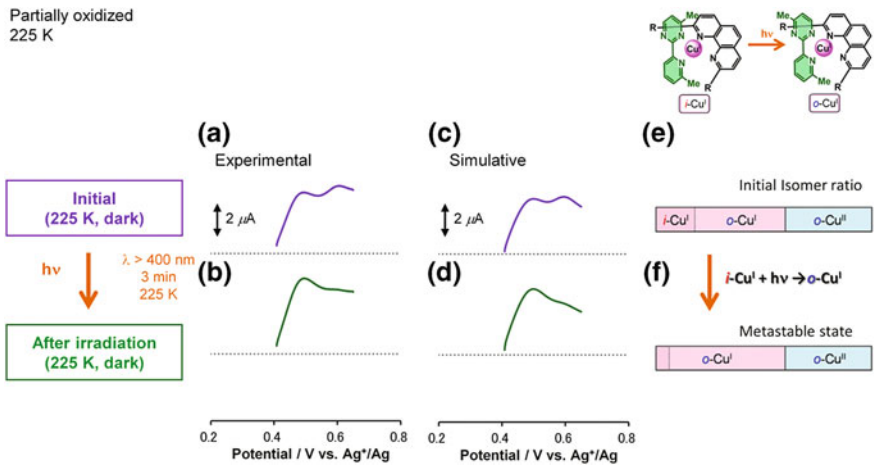

Fig.4.33 Experimental (**a**, **b**) and simulated (**c**, **d**) cyclic voltammograms at a scan rate of 100 mV s^{-1} of 3·BF_4 (0.75 mM) in Bu_4NBF_4–CH_2Cl_2/acetone (v/v 20:1) upon addition of 0.4 equiv. $(NH_4)_2[Ce(NO_3)_6]$ (0.3 mM) at 225 K in the *dark*. (**a**, **c**), (*purple line*): initial state. (**b**, **d**), (*green line*): after 3 min visible light irradiation ($\lambda > 400$ nm) at 225 K. (**e**, **f**) The changes in the molar ratios of the isomers upon light irradiation

Table 4.5 Parameters obtained from simulated cyclic voltammograms of $1{\cdot}BF_4$ in Bu_4NBF_4–CH_2Cl_2/acetone (v/v 20:1) in the partially oxidized system

Temperature/K	225
$E^{\circ\prime}{}_o$/V[a]	0.41
$E^{\circ\prime}{}_i$/V[b]	0.57
K_I^c	2.3
K_{II}^d	8821
k_{ETi}/cm^{-1}[e]	0.008
k_{ETo}/cm^{-1}[e]	0.0008
$k_{Ii\rightarrow o}$/s^{-1}[f]	<0.1
$k_{IIi\rightarrow o}$/s^{-1}[g]	1
α[h]	0.5
R_u/W[i]	3000
C_{dl} μF[j]	5×10^{-6}
D/cm^2 s^{-1}[k]	2×10^{-6}

[a] Redox potential for o-$Cu^{II/I}$, versus Ag^+/Ag
[b] Redox potential for i-$Cu^{II/I}$, versus Ag^+/Ag
[c] Equilibrium constant, set as $[o\text{-}Cu^I]/[i\text{-}Cu^I]$
[d] Equilibrium constant, set as $[o\text{-}Cu^{II}]/[i\text{-}Cu^{II}]$
[e] Rate constant for the electron transfer
[f] Rate constant for the i-$Cu^I \rightarrow o$-Cu^I rotation
[g] Rate constant for the i-$Cu^{II} \rightarrow o$-Cu^{II} rotation
[h] Transfer coefficient
[i] Resistance
[j] Capacitance
[k] Diffusion coefficient for all species

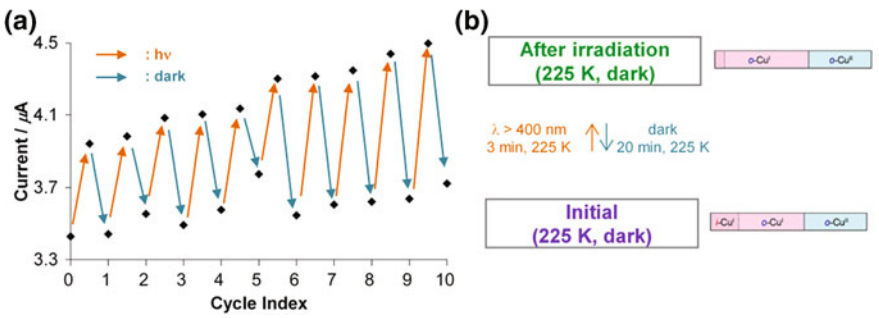

Fig. 4.34 **a** Changes in the anodic peak current at 0.50 V at 225 K in the experimental cyclic voltammograms of the solution upon repeated operation with 3 min of visible light irradiation ($\lambda > 400$ nm) at 225 K and 20 min intervals at 225 K in the dark. The voltammograms are shown in Fig. 4.35. **b** The changes in the molar ratios of the isomers upon the repeated operation

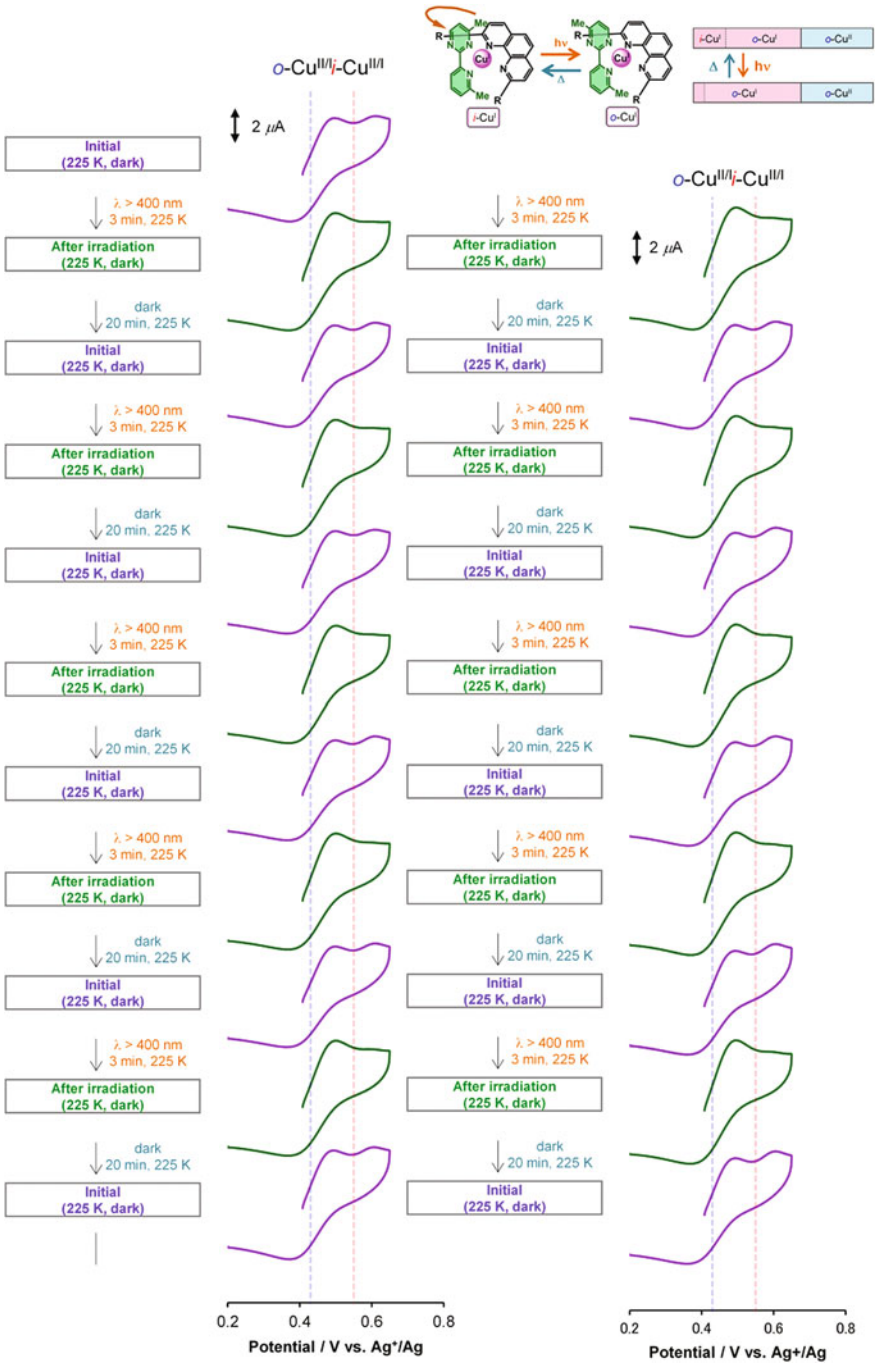

Fig. 4.35 Photorotation experiments in the partially oxidized system with illustrations for procedures. Experimental cyclic voltammograms at a scan rate of 100 mV s^{-1} of 3·BF_4 (0.75 mM) in Bu_4NBF_4–CH_2Cl_2/acetone (v/v 20:1) upon addition of 0.4 equiv. $(NH_4)_2[Ce(NO_3)_6]$ (0.3 mM) at 225 K in the *dark* upon repeated operations with 3 min visible light irradiation ($\lambda > 400$ nm) at 225 K and 20 min interval at 225 K in the *dark*

4.9 Factors Dominating Photorotation Rate

Rate of photodriven rotation in partially oxidized system is much faster than that in the presence of $DMFc^+$. The rate difference is beyond that attributable to concentration or temperature and, therefore, must originate from the rotation mechanism.

When I used $DMFc^+$ with 20 min of visible light irradiation at 225 K and at 200 K (Table 4.4), the light-induced voltammogram changes at 225 K were negligible, because the rate of $o\text{-}Cu^I \rightarrow i\text{-}Cu^I$ thermal reversion at 225 K ($k_{Io\rightarrow i} = 10^{-3}\ s^{-1}$) overcomes that of photodriven $i\text{-}Cu^I \rightarrow o\text{-}Cu^I$. Photodriven rotation in the $DMFc^+$ system, on the other hand, requires cooling to 203 K ($k_{Io\rightarrow i} = 10^{-4}\ s^{-1}$). As the conditions were identical, with the exception of temperature, I determined that the rate increment of $k_{Io\rightarrow i}$ due to heating is larger than that of photodriven rotation. In other words, the slow thermal reversion rate is a determining factor for photodriven rotation at 203 K in the $DMFc^+$ system.

On the other hand, $i\text{-}Cu^I \rightarrow o\text{-}Cu^I$ photodriven rotation was observed at 225 K in a partially oxidized system (Fig. 4.30). Possible variables in the experimental conditions of the $DMFc^+$ and partially oxidized systems related to photorotation behavior are as follows: (i) temperature (225 K), (ii) concentrations of total copper(I) species (0.45 mM), (iii) light irradiation time (3 or 20 min), (iv) concentration of the redox mediator (0.30 or 1.8 mM), and (v) type of redox mediator (copper(II) complex or $DMFc^+$. Conditions (i) and (ii) are identical in both systems. Conditions (iii) and (iv) are considered to work against rapid rotation in a partially oxidized system, by decreasing the density of photons and the probability of collisions during intermolecular electron transfer. Therefore, enhancement of the photorotation rate must be related to redox mediator processes. In a comparison of the two $i\text{-}Cu^I \rightarrow o\text{-}Cu^I$ photorotation schemes (Figs. 4.29 and 4.30), the partially oxidized system does not require back electron transfer processes, which correspond to $o\text{-}Cu^{II} + DMFc^0 \rightarrow o\text{-}Cu^I + DMFc^+$ in $DMFc^+$ system, to complete the scheme. Also, the highly reducing driving force of $o\text{-}Cu^{II}$ can contribute to the higher efficiency of photodriven rotation in the partially oxidized system, as compared with the case in the $DMFc^+$ system. The expected slow rate of electron transfer in copper(II/I) species may contribute to the efficiency of rotation processes.

Consequently, I succeeded in establishing two kinds of systems in which light stimuli are reversibly converted into copper(II/I) redox potentials via molecular rotation, but which exhibited different photorotation behaviors.

4.10 Conclusion

I demonstrated that light stimuli can be repeatedly converted into electrochemical potential via artificial molecular rotation. I synthesized a novel copper(I) complex, $3{\cdot}BF_4$. Two rotational isomers, $i\text{-}Cu^I$ and $o\text{-}Cu^I$, coexist and interconvert in the

solution. The rotational interconversion between *i*-Cu^{I} and o-Cu^{I} is found to be frozen at 203 K and active at 250 K. Two redox reactions, *i*-$Cu^{II/I}$ and o-$Cu^{II/I}$, are different in potentials ($\Delta E^{\circ\prime} = 0.14$ V). The interconversion of oxidized rotational isomers, *i*-Cu^{II} and *o*-Cu^{II}, is faster than that of copper(I) state, and *o*-Cu^{II} is thermodynamically more preferred than *i*-Cu^{II}. Both *i*-Cu^{I} and o-Cu^{I} absorb visible light in solution, and redox potential of light excited state is sufficiently large to induce PET with redox mediator, $DMFc^{+}$. Repeatable electrochemical potential switching based on photodriven rotation, *i*-Cu^{I} → *o*-Cu^{I} and heat-driven rotation, *o*-Cu^{I} → *i*-Cu^{I} was demonstrated. Here, external stimuli induce isomer ratio switching between initial state (*i*-Cu^{I}:*o*-Cu^{I} = 30:70) and metastable state (*i*-Cu^{I}:*o*-Cu^{I} = 12:88). PET processes can take a bypass route in the rotation of the copper(I) complex (*i*-Cu^{I} + hν → *i*-Cu^{I}*, *i*-Cu^{I}* + $DMFc^{+}$ → *i*-Cu^{II} + $DMFc^{0}$, *i*-Cu^{II} → *o*-Cu^{II}, *o*-Cu^{II} + $DMFc^{0}$ → *o*-Cu^{I} + $DMFc^{+}$). Difference in absorption between *i*-Cu^{I} and *o*-Cu^{I} is very small, considering the results of UV–vis spectra upon chemical oxidation at low temperature. The system works not only with a redox mediator but also upon partial oxidation, in which the copper complex itself considerably assists the photorotation, in contrast to the role of $DMFc^{+}$ in the $DMFc^{+}$ system.

Generally, photodriven bistable material changes, based on photochromic molecule, are accompanied by significant color changes, which involve light absorption efficiency and reconstruction of the electronic state [29]. Our present photo- and heat-driven rotation system works without a significant color change or copper(I) ^{1}MLCT absorption, but it can induce electron transfer. It is a representative feature for a new type of photoresponsivity.

Since molecular electronics components such as transistor [32, 33] and memory [34] work by charge injection, the present redox potential response can be progressed into other types of signals via intramolecular electron transfer. The function of the light-driven redox-synchronized molecular rotor can provide electronic, magnetic, and other molecular signaling characteristics.

References

1. Armaroli N, Accorsi G, Cardinali F, Listorti A (2007) Top Curr Chem 280:69–115
2. Schmittel M, Michel C, Wiegrefe A, Kalsani V (2001) Synthesis 10:1561–1567
3. Schmittel M, Ganz A (1997) Chem Commun 999–1000
4. Schmittel M, Michel C, Liu S-X, Schildbach D, Fenske D (2001) Eur J Inorg Chem 1155–1166
5. Pallenberg AJ, Koenig KS, Barnhart DM (1995) Inorg Chem 34:2833–2840
6. Hsieh H-Y, Lin C-H, Tu G-M, Chi Y, Lee G-H (2009) Inorg Chim Acta 362:4734–4739
7. Medwid JB, Paul R, Baker JS, Brockman JA, Du MT, Hallett WA, Hanifin JW, Hardy RA, Tarrant ME, Torley LW, Wrenn S (1990) J Med Chem 33:1230–1241
8. Merrill CL, Wilson LJ, Thamann TJ, Loehr TM, Ferris NS, Woodruff WH (1984) J Chem Soc Dalton Trans 10:2207–2221
9. Tabbi G, Cassino C, Cavigiolio G, Colangelo D, Ghiglia A, Viano I, Osella D (2002) J Med Chem 45:5786–5796

10. Lafferty JJ, Case FH (1967) J Org Chem 32:1591–1596
11. Altomare A, Cascarano G, Giacovazzo C, Guagliardi A, Burla MC, Polidori G, Camalli M (1994) J Appl Cryst 27:435
12. Sheldrick GM (2008) Acta Cryst A64:112–122
13. Farrugia LJ (1999) J Appl Cryst 32:837–838
14. Fulmer GR, Miller AJM, Sherden NH, Gottlieb HE, Nudelman A, Stoltz BM, Bercaw JE, Goldberg KI (2010) Organometallics 29:2176–2179
15. Nomoto K, Kume S, Nishihara H (2009) J Am Chem Soc 131:3830–3831
16. Kume S, Nomoto K, Kusamoto T, Nishihara H (2009) J Am Chem Soc 131:14198–14199
17. Kume S, Nishihara H (2011) Chem Commun 47:415–417
18. Kume S, Nishihara H (2011) Dalton Trans 40:2299–2305
19. Ruthkosky M, Kelly CA, Castellano FN, Meyer GJ (1998) Coord Chem Rev 171:309–322
20. Ruthkosky M, Castellano FN, Meyer GJ (1996) Inorg Chem 35:6406–6412
21. Le Poul N, Campion M, Douziech B, Rondelez Y, Le Clainche L, Reinaud O, Le Mest Y (2007) J Am Chem Soc 129:8801–8810
22. Bard AJ, Faulkner LR (2001) Electrochemical methods, fundamentals and applications, 2nd edn. Wiley, New York
23. Jacq J (1971) J Electroanal Chem 29:149–180
24. Carano M, Echegoyen L (2003) Chem Eur J 9:1974–1981
25. Lerke SA, Evans DH, Feldberg SW (1990) J Electroanal Chem 296:299–315
26. Connelly NG, Geiger WE (1996) Chem Rev 96:877–910
27. Everly RM, Ziessel R, Suffert J, McMillin DR (1991) Inorg Chem 30:559–561
28. Cunningham CT, Cunningham KLH, Michalec JF, McMillin DR (1999) Inorg Chem 38:4388–4392
29. Durr H (1990) Photochromism: molecules and systems. Elsevier, Amsterdam
30. Juris A, Balzani V, Barigelletti F, Campagna S, Belser P, von Zelewsky A (1988) Coord Chem Rev 84:85–277
31. Fery-Forgues S, Delavaux-Nicot B (2000) J Photochem Photobiol A 132:137–159
32. Kubatkin S, Danilov A, Hjort M, Cornil J, Brédas J-L, Stuhr-Hansen N, Hedegård P, Bjørnholm T (2003) Nature 425:698–701
33. Park J, Pasupathy AN, Goldsmith JI, Chang C, Yaish Y, Petta JR, Rinkoski M, Sthena JP, Abruña HD, McEuen PL, Ralph DC (2002) Nature 417:722–725
34. Green JE, Wook Choi J, Boukai A, Bunimovich Y, Johnston-Halperin E, DeIonno E, Luo Y, Sheriff BA, Xu K, Shik Shin Y, Tseng H-R, Stoddart JF, Heath JR (2007) Nature 445:414–417

Chapter 5
Concluding Remarks

As I described in Chap. 1, metal complexes bearing π-conjugated chelating ligands are valid for both application and novel properties (Sect. 1.1). Their unique photophysics, derived from a formation of long-lived charge transfer excited state, is of much interest for dye-sensitized solar cell, light-emitting devices, and photocatalyst. Reversible redox activities of metal complexes are useful in nanotechnology applications such as in molecular electronics, photoelectronic functions, and molecular machines, where the function of muscle is well-imitated at the molecular level. I have rather aimed to develop a single molecular system which imitates five senses of human being. Our group has developed molecular systems exhibiting an electrochemical potential response from an artificial molecular rotor with a stimulus-convertible function, using two rotational isomers, *i*-Cu^I and *o*-Cu^I, in copper complexes bearing two bidentate ligands including unsymmetrically substituted pyridylpyrimidine derivatives (Sect. 1.4). Functions of our previous system are based on a collaboration of electrochemistry and rotational bistability, considering well-established unique relationships between structure and properties in copper complexes (Sect. 1.2).

The aim of studies in my Ph.D course is to develop new properties by photofunctionalization of this molecular system. I developed new classes of luminescence (Chap. 3) and photoresponsivity (Chap. 4).

In Chap. 2, I described details of the equilibrium between *i*-Cu^I and *o*-Cu^I in a series of copper(I) complexes bearing two bidentate ligands, Mepypm and diphosphine, for rational molecular design. **1**·BF_4, **1**·$B(C_6F_5)_4$, **2**·BF_4, and **2**·$B(C_6F_5)_4$ were newly synthesized and characterized. The rotational bistability of these complexes in common organic solvent was characterized using ^{1}H NMR analysis at several temperatures. The interconversion between *i*-Cu^I and *o*-Cu^I is generally an intramolecular process, as confirmed by ^{1}H NMR analysis of a mixed solution of **1**·BF_4 and [Cu(bpy)(DPEphos)]BF_4. The isomer ratio of *i*-Cu^I and *o*-Cu^I was solvent- and counterion-sensitive, because the reduced contact of the counterion to the complex cation in polar solvent seems to contribute to the relative stability of *i*-Cu^I and *o*-Cu^I.

M. Nishikawa, *Photofunctionalization of Molecular Switch Based on Pyrimidine Ring Rotation in Copper Complexes*, Springer Theses,
DOI: 10.1007/978-4-431-54625-2_5, © Springer Japan 2014

In Chap. 3, I described development of system which exhibits dual emission caused by ring rotational isomerization, using **1**·BF_4. The excited states of *i*-Cu^I and *o*-Cu^I were characterized by different structural relaxation process and/or additional solvent coordination properties. In other words, both *i*-Cu^I and *o*-Cu^I emit at room temperature with different emission lifetime. The emission properties of the two isomers differ in lifetime, wavelength, and heat sensitivity. This finding is a novel way to handle the photoprocesses of metal complexes bearing π-conjugated chelating ligands.

As I mentioned above, collaboration of photophysics and rotational bistability enable me to develop a new type of emission. Therefore, combination of photophysics, redox ability, and rotation must provide another new type of function.

In Chap. 4, I described repeatable copper(II/I) redox potential switching driven by visible light-induced coordinated ring rotation. Since **1**·BF_4 and **2**·BF_4 did not exhibit reversible redox activities, I designed and prepared a novel copper(I) complex, **3**·BF_4. The rotational bistability of 3^+ was characterized in a similar method to $\mathbf{1}^+$ and $\mathbf{2}^+$. Prior to photoirradiation (*i*-Cu^I:*o*-Cu^I = 30:70) at 203 K in the presence of a redox mediator, decamethylferrocenium ion ($DMFc^+$), two redox waves, one each for the *i*-$Cu^{II/I}$ (0.62 V vs Ag^+/Ag) and *o*-$Cu^{II/I}$ (0.48 V vs Ag^+/Ag) were observed in the cyclic voltammogram. Photoirradiation with visible light at 203 K, the redox waves gradually converged to a wave corresponding to the *o*-$Cu^{II/I}$. The ratio of *i*-Cu^I to *o*-Cu^I in this metastable state is *i*-Cu^I:*o*-Cu^I = 12:88. Subsequent heating for 2 min at 250 K in the dark recovered the initial voltammogram (*i*-Cu^I:*o*-Cu^I = 30:70), indicating thermal relaxation of the metastable state. Consequently, photodriven rotation, *i*-Cu^I → *o*-Cu^I, and heat-driven rotation, *o*-Cu^I → *i*-Cu^I, are demonstrated. PET processes can take a bypass route in the rotation of the copper(I) complex (*i*-Cu^I + hν → *i*-Cu^I*, *i*-Cu^I* + $DMFc^+$ → *i*-Cu^{II} + $DMFc^0$, *i*-Cu^{II} → *o*-Cu^{II}, *o*-Cu^{II} + $DMFc^0$ → *o*-Cu^I + $DMFc^+$). The system works not only with a redox mediator but also upon partial oxidation, in which the copper complex itself considerably assists the photodriven rotation, *i*-Cu^I → *o*-Cu^I. Generally, photodriven molecular switch based on photochromic molecule are accompanied by significant color changes. This photodriven and heatdriven rotational isomeric system works without a significant color change, which is a representative feature to show a new type of photoresponsivity.

In conclusion, I developed a new type of emission, dual emission caused by ring rotational isomerization. This strategy is applicable not only for luminescence itself but also for properties related to light excited state such as photocatalysis ability and photoelectron conversion in solar cell. Moreover, I developed a new type of photoresponsivity, PET-induced rotation with redox potential switching. This can provide stimuli-convertible functions at a single molecular level, which are related to functions of five senses and motor protein, because of repeatable conversion of external stimuli into redox potential signals.

About the Author

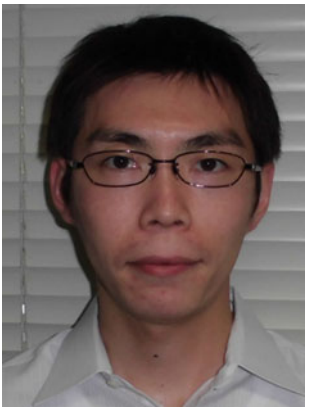

Michihiro Nishikawa
Current affiliation address
City Tokyo, Japan,
Zipcode 180-8633
Country Japan
e-mail: nishikawa@st.seikei.ac.jp
Web: http://www.ml.seikei.ac.jp/tsubomura/

Appoinments

- Assistant Professor, Seikei University (April 2013–)
- Research Fellowship of the Japan Society for the Promotion of Science for Young Scientists (DC2) (2011–2013)

Education

- Doctor of Science (Ph.D.), The University of Tokyo (2010–2013), advisors Dr. Hiroshi Nishihara
- Master of Science (Ph.D.), The University of Tokyo (2008–2010), advisors Dr. Hiroshi Nishihara
- Bachelor of Science (BA), The University of Tokyo (2006–2018), advisors Dr. Hiroshi Nishihara

Major Honors and Awards

- The Chemical Society of Japan Student Presentation Award 2013.
- 60th Conference of Japan Society of Coordination Chemistry Student Presentation Award.

M. Nishikawa, *Photofunctionalization of Molecular Switch Based on Pyrimidine Ring Rotation in Copper Complexes*, Springer Theses,
DOI: 10.1007/978-4-431-54625-2, © Springer Japan 2014